Comprehensive Theoretical Studies of Guided Modes in Multilayer Hybrid Plasmonic Waveguides

by

Sarah Aldawsari

A thesis
presented to the University of Waterloo
in fulfillment of the
thesis requirement for the degree of
Doctor of Philosophy
in
Physics

Waterloo, Ontario, Canada, 2018

Examining Committee Membership

The following served on the Examining Committee for this thesis. The decision of the Examining Committee is by majority vote.

External Examiner	NAME: Xun Li Title: Professor
Supervisor (1)	NAME: Li Wei Title: Professor
Supervisor (2)	NAME: Donna Strickland Title: Associate Professor
Internal Member	NAME: David Yevick Title: Professor
Internal-external Member	NAME: Zoran Miskovic Title: Professor
Other Member	NAME: Jeff Chen Title: Professor

AUTHOR'S DECLARATION

I hereby declare that I am the sole author of this thesis. This is a true copy of the thesis,
Including any required final revisions, as accepted by my examiners.
I understand that my thesis may be made electronically available to the public.

Abstract

Plasmonic waveguides (PWs) have integrated the strength of the miniscule size of electrical-wire interconnects and the large operational bandwidth of photonic waveguides. Beyond the diffraction limit, PWs have the ability to manipulate light at nanoscale structures through surface plasmon polaritons (SPPs) at metal-dielectric interface. Much interest has been paid to PWs because they are promising candidates for developing the next generation highly-dense integrated photonic circuits. However, the tradeoff between mode confinement and propagation loss is an issue encountering PWs. Fortunately, hybrid plasmonic waveguides (HPWs) are recent novel type of PWs, which have shown a favorable balance between mode confinement and propagation loss. Despite the excessive schemes of HPWs that have been proposed and studied theoretically for further enhancement such as symmetrical hybrid plasmonic waveguides, most of these studies are based on using simulation softwares. There is a lack of theoretical study for HPWs based on analytical derived equations, which are important to understand the hybrid guided mode deeply, and study all the key factors that might enhance the optical performance, and help the waveguide designers for the fabrication of plasmonic waveguides.

In this dissertation, comprehensive theoretical studies are presented based on analytical derived expressions for different types of multilayer hybrid plasmonic waveguides. They are hybrid-dielectic-metal-dielectric (DMD) and hybrid-metal-dielectric-metal (MDM) plasmonic waveguides. The guided modes equations have been derived, and their modal properties have been investigated numerically based on the derived analytical equations for different materials, including the modal index and the propagation length. The profile of the fields of the guided modes such as the electric field and energy flux density have been visualized. The hybrid guided modes characteristics has been analyzed thoroughly by proposing two effective criteria. The optical performance of the multilayer hybrid plasmonic waveguides has been also examined by measuring the normalized mode size, figures of merit, and confinement factor of the hybrid guided modes. Moreover, different factors have been taken into accounts in the study, such as the geometrical parameters and the optical properties of the materials. Consequently, these multilayer hybrid plasmonic waveguides have shown a better compromise between mode and propagation loss compared to the PWs. Such waveguides structures can be utilized for ultra-compact active/passive nanophotonic devices.

Acknowledgements

In The Name of Allah, The All-Merciful, The Most-Merciful.

First and foremost, I would like to thank Allah, almighty, for giving me the strength, knowledge, and all-the blessings that help me to accomplish this research work.

I would like to express my deep and sincere gratitude to my supervisor Professor Li Wei. I would like to thank her for her continues support, guidance, motivation, and excellent supervision during my PhD research journey. I would like also to thank my co-supervisors Professor Wing-Ki Liu and Professor Donna Strickland, and my committee members Professor Zoran Miskovic, Professor David Yevick, Professor Jeff Chen, and Professor Xun Li for spending their time to read my thesis, and for their valuable feedback and comments.

I would like to express my deepest gratitude and appreciation to my beloved mother ”Majeda” for her love, support, and prayers for me. My special thanks to my brothers and sisters for their support and encouragement.

I am extremely grateful to my beloved husband and best friend “Mohammed” for his endless love, support, and care to complete this work. Thanks to Allah for blessing me with my lovely two children “Abdullah” and “Abdulaziz”, who make my life more enjoyable.

This research work was supported by King Abdulaziz University, Saudi Arabia. I acknowledge them for their financial support.

Dedication

For my beloved:

My Mother: Majeda

My Father's soul

My husband: Mohammed

My lovely kids: Abdullah & Abdulaziz

Table of Contents

List of Abbreviations

SPPs	Surface Plasmon Polaritons
DMD	Dielectric Metal Dielectric
MDM	Metal Dielectric Metal
HPW	Hybrid Plasmonic Waveguide
SOI	Silicon-On-Insulator
CMOS	Complementary-Metal-Oxide-Semiconductor
SPs	Surface Plasmons
TM	Transverse Magentic
TE	Transverse Electric
FEM	Finite Element Method
DWs	Dielectric Waveguides
PWs	Plasmonic Waveguides
HP	Hybrid Plsmonic
LRS-DMD	Long Rang Symmetrical Dielectric-Metal-Dielectric
SRA-DMD	Short Rang Anti-symmetrical Dielectric-Metal-Dielectric
LRSPP	Long Range Surface Plasmon Polariton
SRSPP	Short Range Surface Plasmon Polariton
LRS-MDM	Long Range Symmetrical Metal-Dielectric-Metal

SRA-MDM	Short Range Antisymmetrical Metal-Dielectric-Metal
CGD	Conductor-Gap-Dielectric
SCGD	Symmetric Conductor-Gap-Dielectric
LML	Low index-Metal-Low index
LHL	Low index-High index-Low index
MLM	Metal-Low index-Metal
MHM	Metal-High index-Metal
LRSH-MDM	Long Rang Symmetrical Metal-Dielectric-Metal
FOM	Figures of Merit
SPP-DW	Surface Plasmon Polariton Dielectric Waveguide

List of Figures

Chapter 1

Introduction

“There is Plenty of Room at the bottom” is the title of the famous lecture given by the physicist Feynman in 1959 [1]. He predicted the potentials of the sub-atomic nanotechnology world in advance before the emergence of this field. One of the lecture outline is minimizing computers. He pointed out that computers are very big; they fill rooms. They can be very small by making the wires in the circuits 10 or 100 atoms in a diameter; thus, the cross of circuits can be a few hundred nanometers. However, on that time, this has not been realized yet because of the conventional micro-scale technology. In the present, Feynman’s vision comes true after the revolutionary advancements in the nano-fabrication techniques. Computers became very small by minimizing the elements of the electronic integrated circuits such as transistors, resistors, capacitors as well as the metal-wire interconnects, which play an important role to transmit electrical signals between the electronic circuit parts.

However, miniaturization of the metal interconnects comes at the cost of the operating speed of electronic devices, which has been limited to a few tens of gigahertz range due to the physical constraints of nanoscale nanowires such as time delay [2]. On the other hand, photonic waveguides (optical interconnects), which transmit electromagnetic waves (optical signals) through dielectric guiding structures, have shown superior high operating speed in the terahertz range. Even though photonic devices have overcome electronics one on the data bandwidth, electronic devices can be scaled down to nano-sizes whereas the photonic devices has failed. This is simply due to the fundamental limit of light known as the diffraction limit [3]; that means, light waves can not be localized down in a aperture with a dimension smaller than their half wavelength in that material. This limit has been an obstacle encountering photonic devices and limit their dimension to micro-scale.

Nano-plasmonic is a novel promising field of science and technology that permits to combine the great features of electronic and photonic technologies [3-6]. Light waves can be confined down to a nano-scale size beyond the diffraction limit through surface plasmon polaritons (SPPs) at metal/dielectric interface [5]. Therefore, extensive research has been conducted in order to exploit the unique properties of SPPs. Many plasmonic waveguide architectures have been proposed such as metal/dielectric/metal (MDM) [7-8] and dielecric/metal/dielectric (DMD) waveguides [9-10]. The former have shown strong confinement whereas the later high propagation length. However, there is one essential issue facing plasmonic waveguides, which is the trade-off between mode confinement and the propagation loss. The loss is due to the nature feature, Ohmic loss of metals at optical frequencies. This major problem has driven researchers to propose different schemes and geometries to enhance the propagation length. One novel type of plasmonic waveguides proposed recently is called hybrid plasmonic waveguide (HPW) [11-12]; it has shown a good balance between confinement and loss. An HPW consists of a subwavelength low-index dielectric layer sandwiched between metal and high-index dielectric layers, where the mode extremely confined in the sub-wavelength layer and decayed exponentially away into metal layer. There is an immense theoretical research studies done on HPWs to achieve higher propagation length based on commercial simulation tools softwares, for example, symmetrical hybrid-MDM and symmetrical hybrid-DMD waveguides based on planar and cylindrical geometries.

However, there is a lack of the theoretical studies based on derived analytical equations, which help to understand deeply the underlying physics of the mode characteristics and study how the geometrical parameters influences on waveguide performance. In this dissertation, comprehensive theoretical studies based on derived analytical expressions are presented based on different models of HPWS such as symmetrical multilayers hybrid-DMD and hybrid-MDM waveguides. For each waveguide, the mode characteristics has been thoroughly investigated based on proposed criteria. Commercial software (Finite element method) also has been used and the results based on it match accurately with the results based on the derived analytical equations.

In this thesis, chapter 2 reviews the fundamentals of nanoplasmonics technology whereas chapter 3 presents the theoretical principles and applications of different types of plasmonic waveguides starting such as simple single metal/dielectric interface, DMD, MDM, and hybrid plasmonic waveguides. In chapter 4, a thorough theoretical analytical study of multilayer symmetrical hybrid-DMD has been investigated by studying the guided mode optical properties, plotting the optical field profiles, analyzing the mode characteristics, and finding figure of merits and mode size. Chapter 5 presents a comprehensive theoretical study for a five layers symmetrical hybrid-MDM waveguide based on analytical results as well as the propagation characteristics of the guided mode.

Chapter 2

Nano-plasmonics

The first revolution in optical-science technology began with the invention of the laser in 1960, followed by the revolution of optical fiber communications in 1980s. The tremendous progress of nanotechnology techniques in the early of 1990s has driven to the third revolution in photonics history: “Nano-photonics”. There has been a considerable interest attracting researchers in nanophotonics field, which can be defined as studying the light-matter interaction at nanoscale size. Nanophotonics has the potential applications in different scientific and engineering fields such as sensors, lasers, energy, and photonics chips. As mentioned, confining and guiding light waves within subwavelength nanoscale conventional photonic devices could not be achieved because of the light diffraction-limit. Extensive research on nanoscale metallic materials has gained a lot of interest to exploit their distinguished optical properties which strongly depend on their size and shape. Localization of light waves at sub-wavelength scale metallic nanostructures becomes feasible by breaking the restriction-limit of light. The field of metallic nanostructures known as nanoplasmonics has received much attention in nanophotonics community. On the other hand, the topic of metallic nanostructures is not a recent scientific research; they have been used to stain glass centuries ago without realizing the physics behind that. The ancient famous example is Lycurgus cup in the British museum from the fourth century AD [6], shown in Fig. 1, where the glass color appears red when light is transmitted through it, and it shines green in a reflective light. This phenomena is due to the resonance of plasmonic metallic nanoparticles such as gold or silver embedded within the glass. However, there is current excitement about nanoplasmonics will be elaborated in this chapter as well as fundamental basic concepts.

2.1 The significance of nanoplasmonics

Nanoplasmonics, a branch of nanophotonics, is a new frontier field that integrates the strengths of both technologies electronics and photonics. It studies the interaction between light and metallic nanostructures. The recent excitement about this field is driven by different factors. Firstly, the high-progress of modern developments in nanofabrication techniques and the ever-increasing need to high-speed data technology have allowed numerous research devoted to metallic nanostructures such as nanoparticles or nano-thin films. When light is confined into minuscule metallic regions smaller than

Fig. 1 The ancient example of nanoplasmonics: the Lycurgus cup from the 4th century (British Museum, London)

the light wavelength, a high-enhancement in the electromagnetic field has been manifested because of the unique optical properties of metallic structures at nanoscale. This field enhancement induces new nano-optical phenomena different from the optical phenomena of the bulk-metal, which can be measured with the current advanced nano-tools, yielding to produce novel nano-photonic devices with superior-functionality beyond the diffraction limit. Secondly, the developments of modeling, simulation, computational techniques have stimulated scientists and engineers to perform theoretical-experiments, design nano-optical devices, and study new-optical phenomena, which can save time and open the possibility to conduct actual experiments. Finally, nanoplasmonics devices are compatible with the present planar fabrication techniques such as silicon-on-insulator (SOI) and complementary metal-oxide-semiconductor (CMOS) technologies. Hence, nanoplasmonics has the potential to provide a vast array of sub-wavelength optical components and integrated them on the same chip to produce the future era of computers “all-optical computers”.

2.2 The Principle of Plasmonics

Plasmonics is the field that concerned with the interactions between electromagnetic waves and metallic structures. Metals consist of collective oscillation of free electrons, called plasmons, moving freely with respect to the fixed positive ions. These plasmons play a crucial role in identifying the optical properties of metals. For instance, electromagnetic waves can not be transmitted through a metal when their frequencies smaller than the plasmons frequencies. The plasmons that confine to a metal-dielectric interface are called surface plasmons (SPs). When light is coupled to these SPs under certain conditions, it generates enhanced evanescent electromagnetic fields, called surface plasmon polaritons SPPs, propagating at the metal-dielectric interface and exponentially decaying away from the boundary into the surrounding materials. The electromagnetics of metals and characteristics of SPPs can be understood by utilizing Maxwell's equations to obtain the wave equation and all the optical properties of SPPs.

2.2.1 Maxwell's Equations

The electromagnetic fields can be represented in vacuum by the electric field $\vec{E}$ and magnetic induction $\vec{B}$ vectors. The interaction of these fields with matter can be prescribed by using the following well-known four equations of Maxwell [13]:

$$\vec{\nabla} \cdot \vec{D} = \rho, \tag{1}$$

$$\vec{\nabla} \cdot \vec{B} = 0, \tag{2}$$

$$\vec{\nabla} \times \vec{E} = -\frac{\partial \vec{B}}{\partial t}, \tag{3}$$

And

$$\vec{\nabla} \times \vec{H} = \frac{\partial \vec{D}}{\partial t} + \vec{J}, \tag{4}$$

which relate the electric charge density ρ and the current density J to the four macroscopic fields: the electric field $\vec{E}$, magnetic field $\vec{H}$, dielectric displacement $\vec{D}$, and magnetic induction $\vec{B}$. In addition, for linear, isotropic media, there are three constitutive material equations, which describe the response of the material to the electromagnetic fields. They can be written as:

$$\vec{D} = \epsilon_0 \epsilon_r \vec{E}, \tag{5}$$

$$\vec{B} = \mu_0 \mu_r \vec{H}, \tag{6}$$

And

$$\vec{J} = \sigma \overrightarrow{E}. \tag{7}$$

ϵ_0 and μ_0 are the electric permittivity and magnetic permeability in free space; ϵ_r, μ_r, and σ are the relative electric permittivity, relative magnetic permeability, and specific conductivity, respectively, where for non-magnetic media, $\mu_r = 1$. Moreover, the permittivities and permeabilities can be written as $\epsilon = \epsilon_0 \epsilon_r$ and $\mu = \mu_0 \mu_r$, where ϵ is called the dielectric constant or dielectric function; it describes the optical response of the materials.

2.2.2 Wave Equation

The propagation of the electromagnetic wave in terms of its electric and magnetic field can be described by obtaining the wave equation [14]. Using Maxwell's equations and some vector calculus will lead to the wave equation. Taking the curl of both sides of Faraday's law Eq. 3 results in:

$$\vec{\nabla} \times \left(\vec{\nabla} \times \vec{E}\right) = -\frac{\partial\left(\vec{\nabla} \times \vec{B}\right)}{\partial t}. \tag{8}$$

The left side and the right side of this relation can be rewritten by applying a vector identity and Ampere-Maxwell law Eq. 4, respectively, as:

$$\vec{\nabla}\left(\vec{\nabla} \cdot \vec{E}\right) - \nabla^2 \vec{E} = -\frac{\partial\left[\mu_0 \mu_r\left(\epsilon_0 \epsilon_r\left(\partial \vec{E}/\partial t\right) + \vec{J}\right)\right]}{\partial t}. \tag{9}$$

For non-magnetic, free-charge, free-current, and homogenous medium, the wave equation for electric field in a medium with dielectric constant ϵ can be written as:

$$\nabla^2 \vec{E} = \mu_0 \epsilon \frac{\partial^2 \vec{E}}{\partial t^2}. \tag{10}$$

This equation represents the electric field of the propagating wave travelling in the medium; the same wave equation for the magnetic field can, also, be obtained by using Ampere-Maxwell's law Eq. 4. In addition, for time harmonic fields, the wave equation Eq. 10 can be simply re-written as:

$$\nabla^2 \vec{E} + k_0^2 \epsilon \vec{E} = 0, \tag{11}$$

where k_0 is the wave number in vacuum ($k_0 = \omega/c = 2\pi/\lambda$). The optical characteristics of any electromagnetic wave within any medium can be fully described by solving the wave mode equation. Thus, the optical properties and the dispersion of SPPs mode relation will be discussed after the next section.

2.2.3 Drude Model

The Drude model or plasma model is used to explain the electromagnetics of metals and their optical properties at different frequencies by assuming sea of free electrons with density *n* moving against fixed positive ions [15]. In this model, the electron-electron interactions and the lattice potential are not considered whereas the effective mass of electron m includes information about the band structure. In the presence of applied an external electromagnetic field $\vec{E}$, the electrons oscillations are damping due to the collisions which can be explained by the characteristics collision frequency $\gamma = 1/\tau$, where τ is the relaxation time of the free electron. Hence, the motion equation of a free electron in the plasma sea of electrons can be written as:

$$m\ddot{\vec{x}} + m\gamma\dot{\vec{x}} = -e\vec{E}, \tag{12}$$

where $x(t) = x_0 e^{-i\omega t}$is the time-harmonic dependent solution of this equation, which represents the electron oscillations with a complex amplitude x_0 relating to the applied electric field by

$$\overrightarrow{x_0}(t) = \frac{e}{m(\omega^2+i\gamma\omega)}\vec{E}(t). \tag{13}$$

The macroscopic polarization relates to the electron displacement $\vec{P} = -ne\vec{x},$ so it can be re-written as:

$$\vec{P} = -\frac{ne^2}{m(\omega^2+i\gamma\omega)}\vec{E}. \tag{14}$$

By using this relation $\vec{D} = \epsilon_0\vec{E} + \vec{P}$, the electric displacement field will be

$$\vec{D} = \epsilon_0\left(1 - \frac{\omega_p^2}{\omega^2+i\gamma\omega}\right)\vec{E}, \tag{15}$$

here, $\omega_p = e\sqrt{\frac{n}{m\epsilon_0}}$ is the plasma frequency of the free electron gas, so the dielectric function of the free electron plasma is

$$\epsilon(\omega) = 1 - \frac{\omega_p^2}{\omega^2+i\gamma\omega}. \tag{16}$$

It is a complex function depends on the frequencies of the plasma and the applied electromagnetic field; it is known as the Drude model which helps to explain the optical behavior of metals.

2.2.4 The Dispersion of Surface Plasmon Polaritons at a Metal-Dielectric Interface

As aforementioned, surface plasmon polaritons SPPs are evanescent electromagnetic waves propagating along a metal/dielectric interface and decaying exponentially in a perpendicular direction to the interface as shown in Fig. 2. The dielectric material is assumed lossless, isotropic, and non-magnetic with dielectric permittivity ϵ_d, and the metal permittivity, $\epsilon_m = \epsilon_m' + \epsilon_m'' i$, is a complex function due to the Ohmic loss of metals. The dispersion in the dielectric constants is neglected. The structure geometry in Fig. 2 is proposed to be infinite in y-direction; so there is no field dependence in that direction.

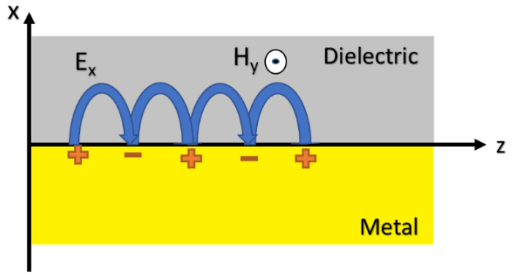

Fig. 2 A schematic diagram of SPPs at the interface of metal-dielectric geometry

To derive the dispersion relation of the SPPs propagating modes [15-16], the wave equation Eq. 11 will be solved in each region with applying the boundary conditions for different mode polarizations: transverse- electric TE and transverse-magnetic TM modes. The general solution of SPPs modes should be in the form $\vec{E}(x,y,z) = \vec{E}(x)e^{i\beta z}$, where β is the propagation constant of the SPPs propagating modes in *z*-direction. Thus, the wave equation can be recast as:

$$\frac{\partial^2 \vec{E}}{\partial x^2} - (\beta^2 - k_0^2 \epsilon_i)\vec{E} = 0, \tag{17}$$

For TE polarization, the non-vanishing field components are (E_y, H_z, H_x), and the general solution of the wave equation in the dielectric and metal regions can be expressed as:

$$\vec{E}(x,y,z) = E_y(x)e^{i\beta z}\hat{y}, \tag{18}$$

where

$$E_y(x) = \begin{cases} Ae^{-k_d x}, & x > 0 \\ Be^{k_m x}, & x < 0 \end{cases}, \tag{19}$$

and k_d and k_m are the wave numbers of the decaying field in the dielectric and metal regions and can be expressed as:

$$k_i = \sqrt{(\beta^2 - k_0^2 \epsilon_i)}, \;\; i = (d, m). \tag{20}$$

The magnetic field can be written as:

$$\vec{H}(x,y,z) = [H_x(x)\hat{x} + H_z(x)\hat{z}]e^{i\beta z}, \tag{21}$$

and by using Faraday-Maxwell equation for time-harmonic:

$$\vec{\nabla} \times \vec{E} = -i\omega\mu\vec{H}, \tag{22}$$

the magnetic field components can be obtained:

$$H(x,y,z)\hat{x} = H_x(x)e^{i\beta z}\hat{x} = \begin{cases} \frac{A\beta}{\omega\mu} e^{-k_d x} e^{i\beta z}\ (\hat{x}), x > 0 \\ \frac{B\beta}{\omega\mu} e^{k_m x} e^{i\beta z}\ (\hat{x}), x < 0 \end{cases} \tag{23}$$

And

$$H(x,y,z)\hat{z} = H_z(x)e^{i\beta z}\hat{z} = \begin{cases} -i\frac{Ak_d}{\omega\mu} e^{-k_d x} e^{i\beta z}\ (\hat{z}), x > 0 \\ i\frac{Bk_m}{\omega\mu} e^{k_m x} e^{i\beta z}\ (\hat{z}),\ x < 0 \end{cases}. \tag{24}$$

To obtain the dispersion relation of SPPs modes, the boundary conditions should be satisfied. Hence, the tangential components of the magnetic fields must be continuous at the interface between the dielectric and metal regions. Applying the boundary conditions at the interface plane x=0 shows that:

$$A = B \tag{25}$$

and

$$A(k_m + k_d) = 0. \tag{26}$$

SPPs propagating modes are confined to the interface of the metal-dielectric layers; so that, k_d and k_m should have positive values in order to maintain their confinement. That means, A should have a zero value, which leads to vanishing B value. Therefore, SPPs modes have no TE polarization.

Similarly, the TM polarization case can be discussed; the wave equation for the magnetic field can be expressed as:

$$\frac{\partial^2\vec{H}}{\partial x^2} - (\beta^2 - k_0^2\epsilon_i)\vec{H} = 0, \tag{27}$$

so the non-zero field components are H_y, E_z, and E_x, whereas the general solution for magnetic field is:

$$\vec{H}(x,y,z) = H_y(x)e^{i\beta z}\hat{y}, \tag{28}$$

Where

$$H_y(x) = \begin{cases} Ae^{-k_d x}, & x > 0 \\ Be^{k_m x}, & x < 0 \end{cases}, \tag{29}$$

and the electric field is

$$\vec{E}(x,y,z) = [E_x(x)\hat{x} + E_z(x)\hat{z}]e^{i\beta z}. \tag{30}$$

The electric field components can be obtained by using the following Ampere-Maxwell's equation for time-harmonic fields:

$$\vec{\nabla} \times \vec{H} = -i\omega\epsilon\vec{E}, \tag{31}$$

so they can be written as:

$$E(x,y,z)\hat{x} = E_x(x)e^{i\beta z}\hat{x} = \begin{cases} -\frac{A\beta}{\omega\epsilon_d}e^{-k_d x}e^{i\beta z}\ (\hat{x}), & x > 0 \\ -\frac{B\beta}{\omega\epsilon_m}e^{k_m x}e^{i\beta z}\ (\hat{x}), & x < 0 \end{cases} \tag{32}$$

and

$$E(x,y,z)\hat{z} = E_z(x)e^{i\beta z}\hat{z} = \begin{cases} i\frac{Ak_d}{\omega\epsilon_d}e^{-k_d x}e^{i\beta z}\ (\hat{z}), x > 0 \\ -i\frac{Bk_m}{\omega\epsilon_m}e^{k_m x}e^{i\beta z}\ (\hat{z}), x < 0 \end{cases}. \tag{33}$$

The continuity of the tangential components of the electric and magnetic fields at the interface *x*=0 requires that:

$$A = B \tag{34}$$

and

$$A\frac{k_d}{\epsilon_d} = -B\frac{k_m}{\epsilon_m}. \tag{35}$$

Since *A*=*B*, this relation can be written as:

$$\frac{k_m}{k_d} + \frac{\epsilon_m}{\epsilon_d} = 0. \tag{36}$$

The wave numbers of the decaying fields into the metal and dielectric materials k_{m} and k_{d} should have positive values, as mentioned before, to keep the confinement of the SPPs modes to the interface; as a result, the permittivity of metal and dielectric materials should have opposite sign of their real part values. Dielectric materials have positive dielectric constants because of their approximate lossless nature, whereas some noble metals at optical frequencies have negative real permittivities $(\epsilon_m') < 0$, which can be evaluated by using Drude model [17]. Therefore, SPPs modes support only TM polarization.

Now, the dispersion equation can be easily derived by dividing the square of the wavevectors of the decaying field in each material Eq. 20:

$$\frac{k_m^2}{k_d^2} = \frac{\beta^2 - k_0^2\epsilon_m}{\beta^2 - k_0^2\epsilon_d}, \tag{37}$$

And by using Eq. 36, the dispersion formula of SPPs can be determined:

$$\beta = k_{spp} = k_0\sqrt{\frac{\epsilon_m\epsilon_d}{\epsilon_m + \epsilon_d}}. \tag{38}$$

Here, k_{spp} the propagation constant of the propagating SPPs modes is a complex function $(k_{spp} = k_{spp}' + ik_{spp}'')$ since the dielectric constant of metal has a complex value. Substituting the metal permittivity complex function $(\epsilon_m = \epsilon_m' + i\epsilon_m'')$ back into Eq. 38 and assuming that $|\epsilon_m''| < |\epsilon_m'|$, the real and the imaginary part of the SPPs mode wavenumber can be obtained:

$$k_{spp}' = k_0\sqrt{\frac{\epsilon_m'\epsilon_d}{\epsilon_m' + \epsilon_d}} = k_0\big[Re(n_{eff})\big] \tag{39}$$

and

$$k_{spp}'' = k_0\frac{\epsilon_m''}{2\sqrt{\epsilon_m'}}\left(\frac{\epsilon_d}{\epsilon_d + \epsilon_m'}\right)^{\frac{3}{2}} = k_0\big[Im\big(n_{eff}\big)\big]. \tag{40}$$

The real part of the SPPs mode dispersion relation provides information about the optical properties of the SPPs modes such as the effective mode index n_{eff} and the SPPs mode's wavelength λ_{spp}, which defined as:

$$\lambda_{spp} = \frac{2\pi}{k_{spp}'} = \frac{2\pi}{k_0}\sqrt{\frac{\epsilon_d + \epsilon_m'}{\epsilon_d\epsilon_m'}} = \lambda\sqrt{\frac{\epsilon_d + \epsilon_m'}{\epsilon_d\epsilon_m'}}. \tag{41}$$

As noticed, the wavelength of the SPPs modes λ_{spp} is always smaller than the free space wavelength λ at the same frequency by a factor $\sqrt{(\epsilon_d + \epsilon_m')/(\epsilon_d \epsilon_m')}$, which depends on the optical properties of the metal and dielectric materials, so controlling the materials permittivities can reduce the SPPs mode's wavelength to sub-wavelength scale. Thus, this feature of SPPs waves' wavelength as well as their confinement to the metal-dielectric interface makes them overcoming the diffraction limit of light in conventional dielectric waveguides.

On the other hand, the imaginary part of the dispersion relation Eq. 40 measures the propagation length of the SPPs mode which defined as the distance where the SPPs propagating modes power decayed by $1/e$ of its initial value and can be expressed mathematically as:

$$L_p = \frac{1}{2k''_{spp}} = \frac{\lambda}{4\pi Im(n_{eff})}, \tag{42}$$

the imaginary part of the effective mode index reflects the loss of the SPPs modes, as the $Im(n_{eff})$ decreases, the propagation length would increase.

The momentum of the SPPs modes is greater than the momentum of a free space waves at the same frequency as shown in Eq. 38 and illustrated in Fig. 3 This momentum mismatch disables the direct excitation of the SPPs waves when the free space radiation is incident on the metal-dielectric interface; hence, there are some proposed techniques in order to solve the momentum-mismatch issue such as using prisms or gratings [18-19].

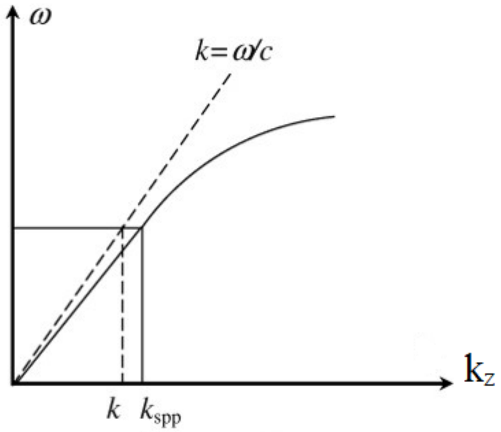

Fig. 3 The momentum mismatch between the SPP wave and the free-space wave at the same frequency

Figure 4 illustrates the electric field profile of the SPPs mode at the metal (Ag)/Dielectric (Si) interface at the telecom wavelength 1550 nm by using the Finite Element Method (FEM) mode solver in COMSOL software (see the Appendix for detailed information about the mode solver) [20]. The refractive index of silicon is n_{Si}=3.455 whereas the permittivity of silver is $\varepsilon_{Ag} = -129 + 3.3j$ [25-26].In this thesis, the dimensional coordinate axes have been chosen according to our assumption of Fig. 2, where the SPP mode's electric field is decaying exponentially at the materials interface in (x-direction), and the SPPs mode propagation direction is (z-direction) whereas the y-direction assumed to be infinite. The 1D plot for the absolute value of the electric field x-component $E_x(x, 0)$ of the SPPs mode at the Ag/Si interface is shown in Fig. 4(b), where the field is maximized at the interface and decayed into the two regions. The electric field decays exponentially in the metal layer more than dielectric layer due to the Ohmic loss of metals. Figure 4(a) demonstrates the 2D cross sectional surface plot for the electric field distribution of the SPPs single (Ag/Si) interface. As seen, the field is highly concentrated at the interface, where the dark-red corresponds to the maximum field, and the dark-blue indicates to the minimum field. In our study, we assume that the structure is 1D and it is infinite in the y-axis, so the field has to be stretched in the y-axis. However, due to the limitation of the COMSOL to perform study in 1D, the boundary conditions (Perfectly Matched Layer) are used in the simulation around the whole 2D geometry domain. As a result, one can see that the lateral mode confinement at the y-axis boundary (i.e., left and right direction). Note that this approach has been used in this thesis for all 2D plots.

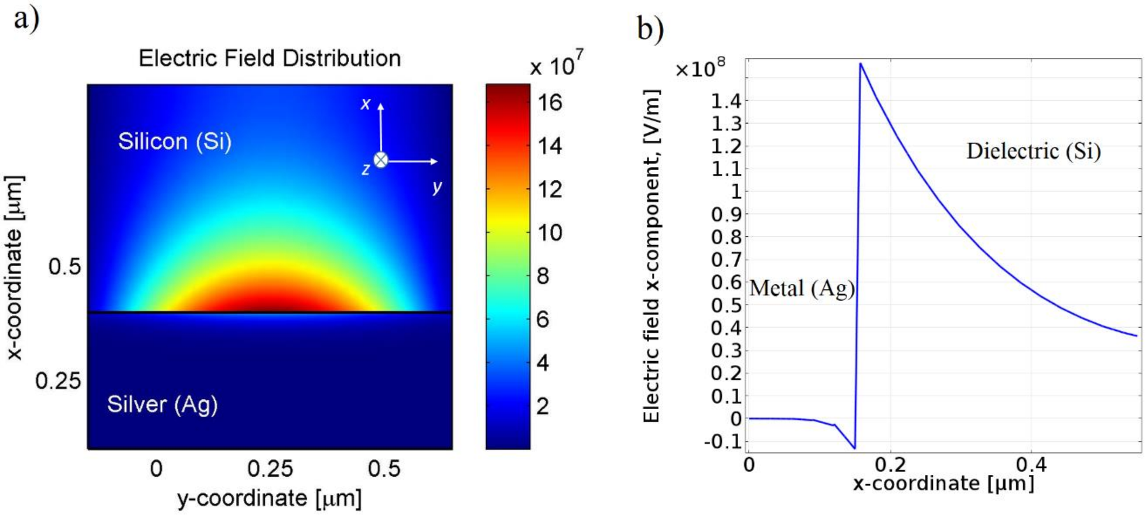

Fig. 4 a) The surface plot for the electric field distribution of the SPPs mode at Ag/Si interface, at 1550 nm wavelength, b) the 1D plot for the $E_x(x, 0)$.

Chapter 3

Plasmonic Waveguides

Optical fiber communications have revolutionized information transportation due their superior functionality to transmit enormous data over long distances with low cost. However, the capacity of data transmission on the short-distance level, on the chip-scale electronic integrated circuits, has been limited in terms of their speed because of the time-delay of metallic interconnects at nano-scale. Using light waves as information carriers on chips nanoscale circuits can tackle this issue of limiting data transmission rate of electronic circuits. Conventional dielectric waveguides (DWs) which guide light within a region with high- refractive index surrounding with low-index cladding is governed by the total internal reflection principle through Snell’s law. However, the diffraction limit of light in optical photonic waveguides has been a barrier in front of miniaturization photonic waveguides; that means, light waves can not be compressed within a domain with a dimension smaller than half their wavelength in that medium. Fortunately, nano-plasmincs has enabled to overcome the diffraction restrict of light by using surface plasmon polaritons SPPs waves, which discussed previously. One of the SPPs based-applications which received significant research attention over the past decade is plasmonic waveguides (PWs) that enable the conversion of light into surface plasmon polaritons (SPPs) on the sub-wavelength scale at the metal-dielectric interface beyond the diffraction limit. They are promising candidates for developing the next generation of ultra-compact integrated devices that have the advantages of both the large operational bandwidth of photonics and true nanometer-scale modal confinement, which paves the way to a future integration of high-capacity photonic and electronic devices at a scale comparable to electronics. Various SPPs waveguides structures and geometries have been proposed in order to harness the unique features of SPPs waveguides at nanoscale such as V-grooves [21-22], dielectric-metal-dielectric (DMD) waveguide, metal-dielectric-metal (MDM) waveguides, and metallic nanowires [23]. In spite of the interest features of PWs, there is one major problem facing them, which is the tradeoff between loss and confinement. A recent novel type of PWs has been investigated to provide a balance between mode confinements and propagation loss, called a hybrid plasmonic waveguide (HPW). In this chapter, three types of plasmnic waveguides: DMD, MDM, and hybrid plasmonic waveguides will be analyzed by deriving their modes’ equations analytically, studying their optical performance, plotting their optical field profiles, discussing their advantages and disadvantages, and exploring their potential applications.

3.1 Dielectric-Metal-Dielectric Plasmonic Waveguide

3.1.1 Basic principle

A DMD waveguide consists of a thin metal film with width d and permittivity ϵ_m surrounding with two dielectric layers with dielectric constants $\epsilon_{d1}$and ϵ_{d2} as illustrated in Fig. 5. Assuming the two dielectric layers are semi-infinite, and the geometry is infinite in the *y*-direction, so there is no field *y*-component. Such a structure supports two coupled SPPs modes propagating along *z*-direction, resulting from each SPPs mode at the two interfaces of the metal-dielectric layer. In order to study the DMD guided mode characteristics, the wave equation should be solved in each region, where the origin point O assumed to be in the mid of the thin metal film.

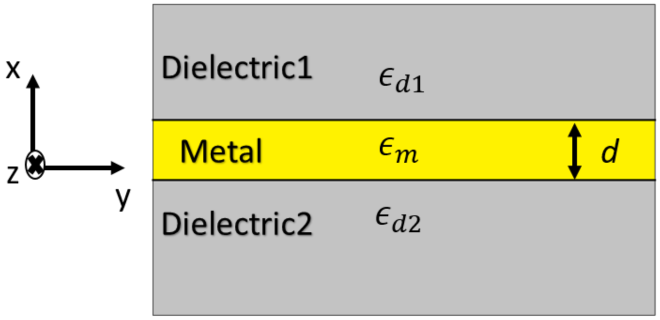

Fig. 5 The geometry of the DMD plasmonic waveguide

Since the SPPs mode has only a TM polarization, the nonzero-components H_y, E_x, and E_z and the wave equation for magnetic field will be used in each region

$$\nabla^2\vec{H} - (\beta^2 - k_0^2\epsilon_i)\vec{H} = 0, \tag{43}$$

where $i = (d_1, m, d_2)$ refers to the three regions; The general solution of the wave equation has the form $\vec{H}(x,y,z) = H_y(x)e^{i\beta z}\hat{y}$. Hence, the solution of Eq. 43 which gives the amplitude part of the DMD guide mode in each layer can be written as:

$$H_y(x) = \begin{cases} Ae^{-k_{d1}x},\ x > \frac{d}{2} \\ Be^{-k_m x} + Ce^{k_m x}, -\frac{d}{2} < x < \frac{d}{2}, \\ De^{k_{d2}x},\ x < -\frac{d}{2} \end{cases} \tag{44}$$

Here, the wave number of the decaying fields in each medium can be expressed as:

$$k_i = \sqrt{\beta^2 - k_0^2 \epsilon_i}, \text{ where } i = d1, m, and\ d2. \qquad (45)$$

Utilizing Ampere-Maxwell Eq. 31, the electric field components can be obtained:

$$E(x,y,z)\hat{x} = E_x(x)e^{i\beta z}\hat{x} = \begin{cases} -\frac{\beta A}{\omega \epsilon_{d1}} e^{(i\beta z - k_{d1}x)}\ (\hat{x}),\ x > \frac{d}{2} \\ -\frac{\beta}{\omega \epsilon_m} e^{i\beta z}\left(Be^{-k_m x} + Ce^{k_m x}\right)(\hat{x}), -\frac{d}{2} < x < \frac{d}{2} \\ -\frac{\beta D}{\omega \epsilon_{d2}} e^{(i\beta z + k_{d2}x)}\ (\hat{x}),\ x < -\frac{d}{2} \end{cases} \qquad (46)$$

And

$$E(x,y,z)\hat{z} = E_z(x)e^{i\beta z}\hat{z} = \begin{cases} \frac{iAk_{d1}}{\omega \epsilon_0 \epsilon_{d1}} e^{(i\beta z - k_{d1}x)}\ (\hat{z}), x > \frac{d}{2} \\ \frac{ik_m}{\omega \epsilon_0 \epsilon_m} e^{i\beta z}\left(Be^{-k_m x} - Ce^{k_m x}\right)(\hat{z}), -\frac{d}{2} < x < \frac{d}{2}. \\ -\frac{iDk_{d2}}{\omega \epsilon_0 \epsilon_{d2}} e^{(i\beta z + k_{d2}x)}\ (\hat{z}),\ x < -\frac{d}{2} \end{cases} \qquad (47)$$

To derive the characteristics DMD mode equation, the tangential components of the electric and magnetic fields must be continuous at the boundaries at $x = \pm d/2$. Thus, the dispersion relation for DMD plasmonic waveguide can be written as:

$$e^{2k_m d} = \frac{\left(\frac{k_m}{\epsilon_m} - \frac{k_{d1}}{\epsilon_{d1}}\right)\left(\frac{k_m}{\epsilon_m} - \frac{k_{d2}}{\epsilon_{d2}}\right)}{\left(\frac{k_m}{\epsilon_m} + \frac{k_{d2}}{\epsilon_{d2}}\right)\left(\frac{k_m}{\epsilon_m} + \frac{k_{d1}}{\epsilon_{d1}}\right)}. \qquad (48)$$

When the structure is symmetrical $\epsilon_{d1} = \epsilon_{d2} = \epsilon_d$, the dispersion relation will be:

$$e^{k_m d} = \pm \frac{\left(\frac{k_m}{\epsilon_m} - \frac{k_d}{\epsilon_d}\right)}{\left(\frac{k_m}{\epsilon_m} + \frac{k_d}{\epsilon_d}\right)}. \qquad (49)$$

Since the plasmonic mode has only TM polarization, the DMD plasmonic waveguide supports TM modes. The positive sign in the dispersion relation corresponds to the Long Range Symmetrical DMD (LRS-DMD) fundamental TM mode supported by the waveguide structure whereas the negative sign refers to the Short Range Anti-symmetrical DMD (SRA-DMD) TM mode [9, 24]. The transverse electric field of the SR SPP mode is anti-symmetric with respect to the center metal film layer and that of LRSPP is symmetric. For a thick metal film, the two modes are degenerated. For a thin metal film, with decrease of the metal thickness, the propagation loss of the SRSPP increases, rapidly leading to the cutoff of the mode while that of the LRSPP decreases, giving rise to a long-range propagation distance. The characteristics mode equation Eq. 49 can be also expressed in a transcendental form; hence, for the positive sign:

$$\tanh\left(\frac{k_m d}{2}\right) = -\frac{k_d \epsilon_m}{\epsilon_d k_m}, \tag{50}$$

and for the negative sign:

$$\tanh\left(\frac{k_m d}{2}\right) = -\frac{k_m \epsilon_d}{\epsilon_m k_d}, \tag{51}$$

3.1.2 Numerical Analysis

We solved numerically Eq. 50 and Eq. 51 to study the mode optical characteristics of the fundamental TM DMD guided mode. The performance of any waveguide can be simply studied by finding the mode effective index n_{eff} and the propagation length L_{p}, where the former corresponds to the confinement and the later to the loss. Fig. 6 shows the modal index and the propagation length of the two types of DMD mode (i.e., SR-DMD and LR-DMD mode) supported by the DMD waveguide structure at the optical communication wavelength 1550 nm over a range of metal thickness $d\ (0-150) nm$, where the dielectric chosen to be silica with a refractive index $n_{SiO_2} = 1.445$, and the metal film chosen to be silver with a permittivity $\varepsilon_{Ag} = -129 + 3.3j$ [25-26]. For the LR-DMD mode, as the metal film thickness increases the DMD modal index increases until it reaches a maximum thickness $d_{max} \approx 125\ nm$, there is no DMD mode supported any more, at this maximum thickness, the DMD modal index approaching to the modal index of a single metal/dielectric interface. Thus, the condition to have a strong DMD mode is the metal film thickness should be less than the maximum cutoff thickness where the DMD modal index reaches to $\sqrt{\epsilon'_m \epsilon_d / (\epsilon_d + \epsilon'_m)}$. Here, the cutoff thickness is about 125 nm, so the formation of the SPP DMD mode needs a minimized subwavelength metal thickness much less than 125 nm. The physical interpretation of having small metal gap thickness to form a DMD plasmonic mode is simply because the propagating SPP plasmonic modes are confined to the metal-dielectric interface and decaying exponentially in a perpendicular direction to the interfaces, and due to the lossy nature of metals, the part of the SPP modes decaying in the metal film requires only a very small distance until vanishes, whereas the decaying field in the dielectric parts are longer due to the lossless nature of dielectric. For the SR-DMD mode, the behavior of the modal index is different from the LR-DMD mode; at large metal thicknesses the two types of mode converge to the same modal index which mean the single metal-dielectric interface mode is evolved as shown in Fig. 6 (Left). However, at small metal thickness, the SR-DMD reaches to the cutoff metal thickness where there is no SR-DMD mode. We can see clearly from the propagation length in Fig. 6 how the propagation length behavior of the two types of DMD-mode is different, where the LRS-DMD waveguide mode has higher propagation length compared to the SRA-DMD mode. For this reason in our study, we will focus on the long-range symmetrical mode. At almost a few nanometer metal thicknesses, the propagation length of the LRS-DMD mode reaches a couple of thousands microns. When the metal thickness starts increasing, the propagation length reduces to a couple of hundreds microns as shown in the figure; this can be attributed to the Ohmic loss of metals.

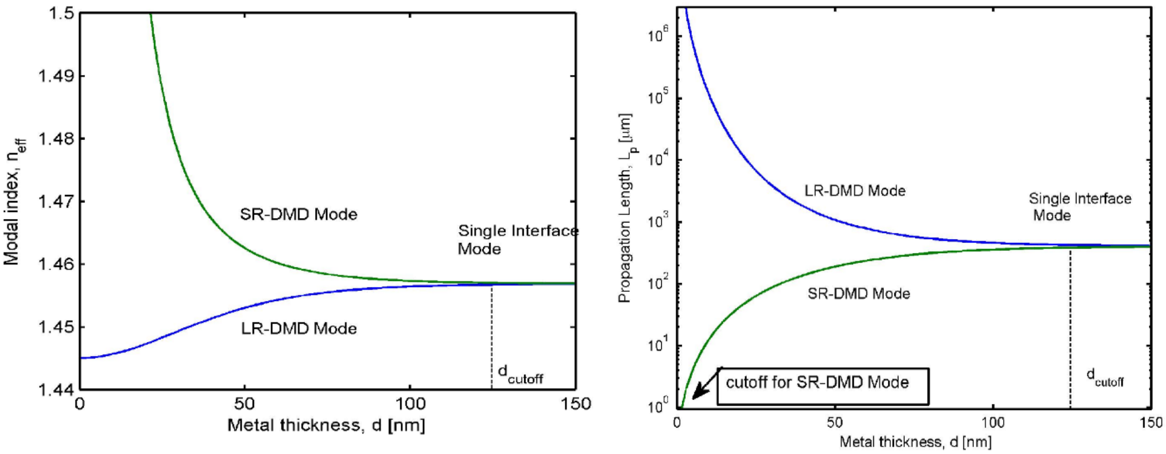

Fig. 6 The modal index and the propagation length of the DMD waveguide mode

The effect of the metal film thickness on the DMD mode's formation and confinement can be realized by plotting numerically the transverse magnetic field component (in Eq. 44) of the DMD mode at different metal thicknesses. One way to measure the mode confinement is by finding the confinement factor Γ, the ratio of the propagating power within the metal film to the whole mode's energy in all three layers, which can be expressed as [27]:

$$\Gamma = \frac{\frac{1}{2}\int_{m} Re\left(\vec{E}\times\vec{H}^{*}\right)\cdot\hat{z}\,dx}{\frac{1}{2}\int_{whole} Re\left(\vec{E}\times\vec{H}^{*}\right)\cdot\hat{z}\,dx}. \tag{52}$$

Figure 7 illustrates the $H_y(x)$ field profile of the DMD mode at different metal thicknesses d=20, 50, and 100 nm, for the same materials used in Fig. 6. As seen in Fig. 7, DMD mode is weakly confined within the metal layer which simply due to the Ohmic loss of metals. At very small metal thickness *d*=20 nm, the propagation length according to Fig. 6 is a few thousands of microns, whereas the mode confinement is very weak about 0.02%. As the metal thickness increases to 50 nm, the confinement gradually increased to 0.035%, which is still very low. When the metal thickness approaches to the cutoff condition where the DMD mode starts to be single metal-dielectric interface mode, the coupling strength decreases as well as the mode confinement, where the field strongly confined to the interfaces; this yields to a reduction in the mode confinement to 0.034%. Even though DMD mode has lower attenuation loss; however, the mode confinement is very weak.

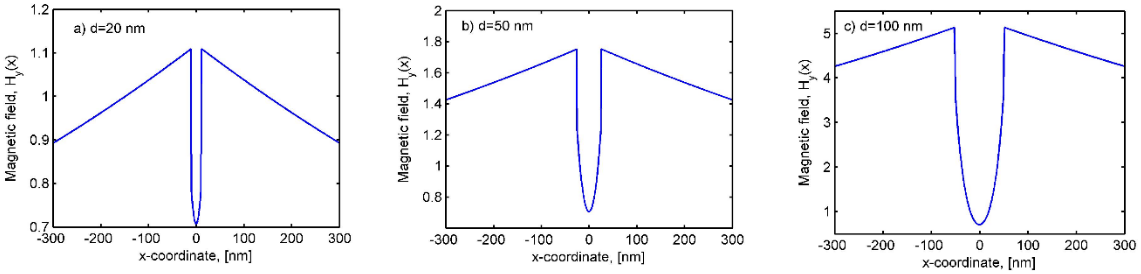

Fig. 7 The magnetic field profile of the DMD waveguide mode at different metal thicknesses *d*=20, 50, and 100 nm

In addition, the electric field of the DMD (SiO_2/Ag/SiO_2) plasmonic waveguide mode at dielectric thickness *d*=30 nm and at wavelength 1550 nm is shown in Fig. 8 by using COMSOL software. The surface plot, Fig. 8(a) shows the electric field of the DMD mode where the field is highly concentrated at the Ag/SiO2 interface and decaying into the two materials. The highest field distributes in the dielectric layer whereas the lowest field is confined within the metal region which can be seen clearly in the 1D plot of the $E_x(x,0)$ for the DMD mode (in Fig. 8(a). This non-enhancement field within metal layer attributes to the loss associated with metals.

SPP DMD modes supported by DMD waveguides have higher propagation lengths in the order of couple thousands microns better than metal/dielectric single interface modes, which have a few hundred microns as noticed in the example in Fig. 6. This essential feature makes DMD waveguides have the potential for nano-optical devices that require higher propagation length. Different structures of DMD plasmonic waveguides have been studied in order to investigate the possibility to guide light waves at nano-scale level. These research studies have agreed to call the DMD SPP modes “Long-Range SPP waves” due to their lower attenuation loss [28-33]. Even though DMD waveguides have shown higher propagation lengths, the confinement of their modes are weak compared to MDM plasmonic waveguides, will be discussed in the following section, which might restrict their use in the integrated photonics applications that require very strong field confinement such as all-optical switching and signal processing data.

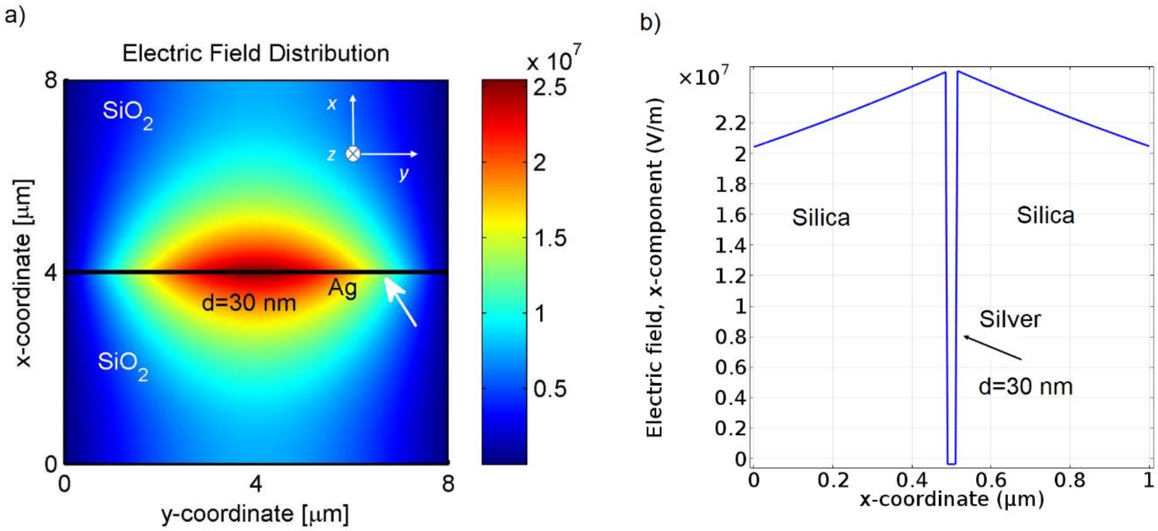

Fig. 8 a) The surface plot for the electric field of the DMD (SiO_2/Ag/SiO_2) plasmonic mode at d=30 nm, and b) 1D plot for the $E_x(x, 0)$

3.2 Metal-Dielectric-Metal Plasmonic Waveguide

3.2.1 Basic Principle

As opposite to the DMD waveguide, an MDM plasmonic waveguide consists of a dielectric film with thickness d and dielectric constant ϵ_d surrounding by a cladding and a substrate of metal with complex-valued permittivity ϵ_c and ϵ_s, respectively, where the MDM waveguide geometry is depicted in Fig. 9.

In order to comprehend the plasmonic mode guided by the MDM waveguide structure, the characteristic mode equation should be solved. Similar to the derivation of the DMD waveguide mode, the MDM waveguide mode equation can be obtained:

$$e^{2k_d d} = \frac{\left(\frac{k_d}{\epsilon_d} - \frac{k_c}{\epsilon_c}\right)\left(\frac{k_d}{\epsilon_d} - \frac{k_s}{\epsilon_s}\right)}{\left(\frac{k_d}{\epsilon_d} + \frac{k_s}{\epsilon_s}\right)\left(\frac{k_d}{\epsilon_d} + \frac{k_c}{\epsilon_c}\right)}. \tag{53}$$

For simplicity, the cladding and substrate metals are assumed to be symmetrical $\epsilon_c = \epsilon_s = \epsilon_m$.

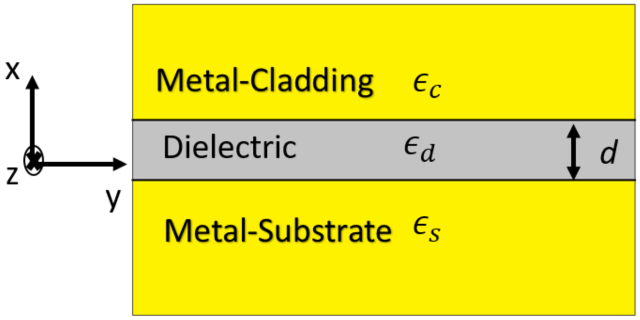

Fig. 9 The MDM plasmonic waveguide structure

Hence, the dispersion relation can be expressed as:

$$e^{k_d d} = \pm \frac{\left(\frac{k_d}{\epsilon_d} - \frac{k_m}{\epsilon_m}\right)}{\left(\frac{k_d}{\epsilon_d} + \frac{k_m}{\epsilon_m}\right)}. \tag{54}$$

In transcendental forms, the positive sign can be written as:

$$\tanh\left(\frac{k_d d}{2}\right) = -\frac{k_m \epsilon_d}{\epsilon_m k_d}, \tag{55}$$

and the negative sign one

$$\tanh\left(\frac{k_d d}{2}\right) = -\frac{k_d \epsilon_m}{\epsilon_d k_m}. \tag{56}$$

As discussed in the previous section, the positive sign characteristic mode equation represents the fundamental transverse magnetic TM Long Range Symmetrical MDM (LRS-MDM) mode, whereas the negative sign one corresponds to the transverse magnetic TM Short Range Anti-symmetrical MDM (SRA-MDM) mode. The discussion will be limited to the LRS-MDM modes due to their lower propagation loss.

3.2.2 Numerical Analysis

By solving the mode equation Eq. 55 numerically, the optical properties of the MDM plasmonic guided mode can be investigated such as the modal index, propagation length, optical fields, and the mode confinement. Figure 10 illustrates the modal index and the propagation length of the MDM guided mode over a range of dielectric film thickness *d*=0-200 nm at the optical communication wavelength 1550 nm, where the dielectric and metal layers chosen to silica and silver; the same materials are used in the example of the previous section for DMD waveguide mode, for a comparison purpose. At a few nanometers of dielectric thickness *d*, the modal index of the MDM guided mode has a large value, and it decreases as the dielectric thickness increases until it reaches the cutoff dielectric thickness, where the modal index of the MDM mode approaches to the single interface SPP modal index $n_{eff,\infty} = \sqrt{\epsilon_m \epsilon_d/(\epsilon_m + \epsilon_d)}$. The cutoff dielectric thickness d_{cutoff} of MDM waveguide can be obtained from the mode equation Eq. 55 by assuming $\left|\frac{k_d d}{2}\right| \ll 1$ and using the estimation $\tanh(x) \approx x$:

$$d_{cutoff} \approx Re\left(-2\frac{\epsilon_d}{\epsilon_m}\frac{\sqrt{n_{eff,\infty}^2 - \epsilon_m}}{k_0\left(n_{eff,\infty}^2 - \epsilon_d\right)}\right). \tag{57}$$

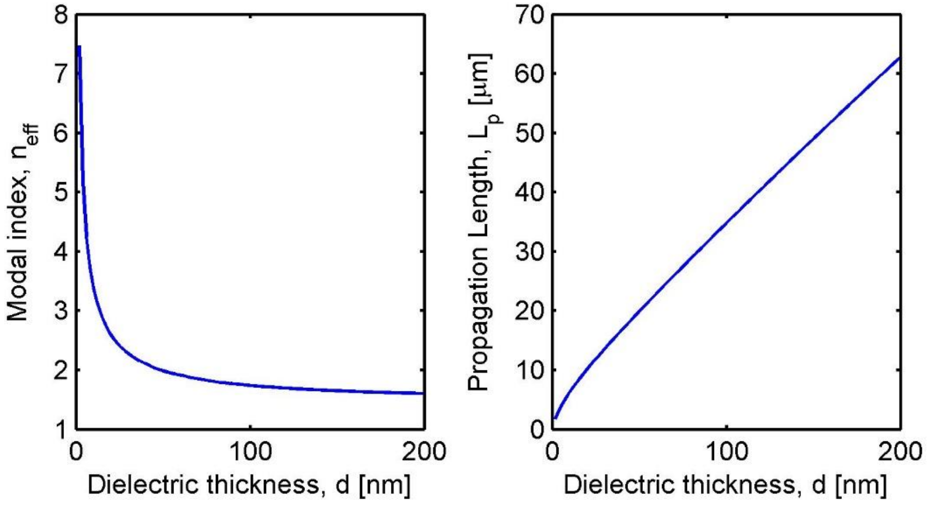

Fig. 10 The modal index and the propagation length of the MDM waveguide mode versus the dielectric thickness *d*

Here, the cutoff dielectric thickness will be about 2600 nm, so it is a large value compared to the cutoff metal thickness of the DMD waveguide d_{cutoff} =100 nm in the previous section. This intuitively refers to that the MDM guided mode which results from the coupling between the two the single interface surface plasmons modes in the dielectric layer, so the majority of the decayed field is localized in the dielectric gap and minority of the fields decayed into the metal claddings. Hence, this enhancement of the MDM fields within the dielectric gap increases the cutoff dielectric thickness of the MDM waveguide mode. Contrary to the modal index of MDM guided mode, the propagation length increases tens microns as the dielectric thickness increases. However, this propagation lengths is very small compared to the propagation lengths of the DMD guided mode, which in the range of a couple of hundreds microns. This high propagation loss attributes to the resistive heating loss of two metal claddings.

The transvers magnetic field of the MDM guided mode can be plotted numerically by solving the derived mode equation Eq. 55 at different dielectric thicknesses *d*=20, 50, and 100 nm as shown in Fig. 11, at the same metal thicknesses of the DMD guided mode in Fig. 7. It can be seen that how the MDM strongly confined within the dielectric film with almost a 99% confinement factor, which totally different from the confinement of the DMD guided mode that shows weaker confinement as the metal thickness increases. In the small limit of the dielectric thickness *d*=20 nm, the decaying length of the fields in the dielectric layers is larger than the dielectric film thickness d, so this reduces the exponential decayed fields into the metals leading to increase the spatial extent of the mode. As the dielectric thickness increases, the exponential decaying of the fields increases in the metal clads, limiting the spatial extent of the MDM mode.

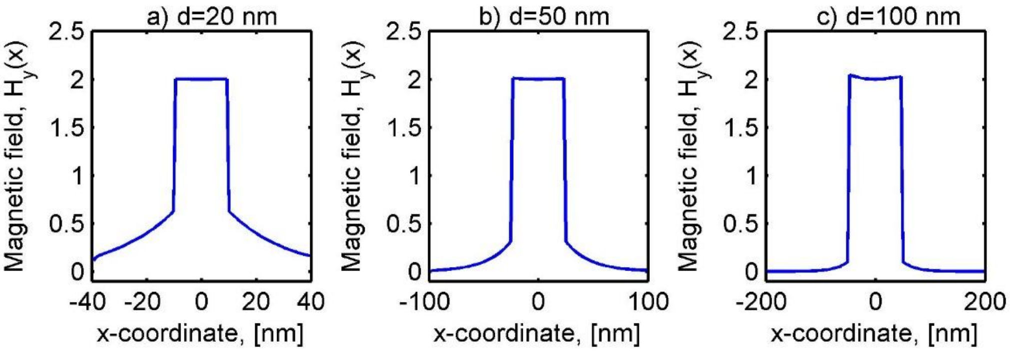

Fig. 11 The transvers magnetic field of the MDM guided mode at dielectric thicknesses *d*=20, 50, and 100 nm

Figure 12 shows the 2D plot for electric field magnitude of the MDM (Ag/SiO$_2$/Ag) plasmonic waveguide mode at 1550 nm and the 1D plot for electric field x-component $E_x(x,0)$, at dielectric thickness d=30 nm, by using the FEM mode solver. The surface plot as well as the 1D plot demonstrate how the field is highly localized within the dielectric region and rapidly decayed in the metal regions. Comparing this example with Fig. 8 for the DMD plasmonic waveguide, where the materials and the core thickness are the same, we can see how the MDM plasmonic waveguide provides strong confinement within the core region better than DMD plasmonic mode.

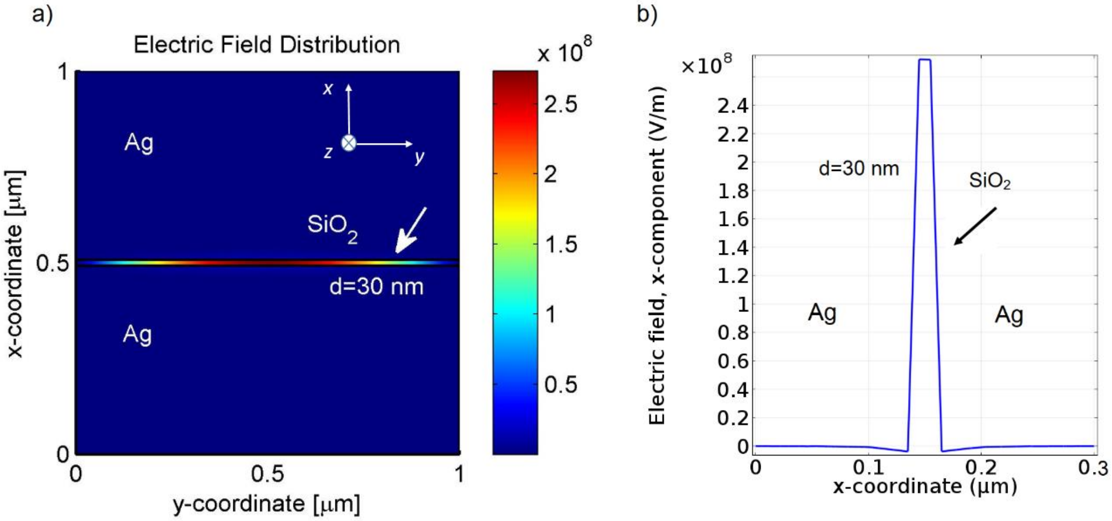

Fig. 12 a) The 2D plot for the electric field, and the b) 1D plot for the electric field x-component of the MDM (Ag/SiO2/Ag) plasmonic mode at dielectric thickness *d*=30 nm

Due to the strong confinement provided by the MDM waveguides, much research have been conducted to exploit their features for sub-wavelength on-chip optical devices, such as sensing [34-35], all optical switching [36-37] and filtering [38-40]. DMD waveguides have shown higher propagation length with lower mode confinement while the MDM waveguides have shown strong mode confinement with lower propagation length. Thus, there is a remarkable tradeoff between propagation loss and mode confinement.

3.3 Hybrid Plasmonic Waveguide

3.3.1 Background

Even though plasmonic waveguides (PWs) have received much interests due to their unique features to confine light in deep sub-wavelength structures, the propagation loss accompanied to the PWs has limited their applications. Intensive research have been done to enhance the optical performance of PWs. A hybrid plasmonic waveguide (HPW) is a recently proposed novel type of plasmonic waveguides that could obtain high confinement and low propagation loss simultaneously. A basic HPW consists of a sub-wavelength low-index dielectric layer sandwiched between a metal layer and a high-index dielectric layer. The first pioneer work was proposed in 2007 by Alam *et al.* based on a rectangular geometry shown in Fig. 13(a) [11, 41]. Their proposed structure consists of a low-index dielectric spacer (silica) embedded between a high-index dielectric (silicon) and a metal substrate (silver) at the wavelength 800 nm. They found that the absence of the metal layer yields to have a conventional dielectric mode localized in the silicon nano-wire and the absence of the silicon layer leads to have a single interface metal/dielectric surface mode. However, the presence of the silicon layer close to the metal separated by a thin-spacer silica results in forming a Super-mode, which highly concentrated in the sub-wavelength low-index layer as displayed in the Fig. 13(b).

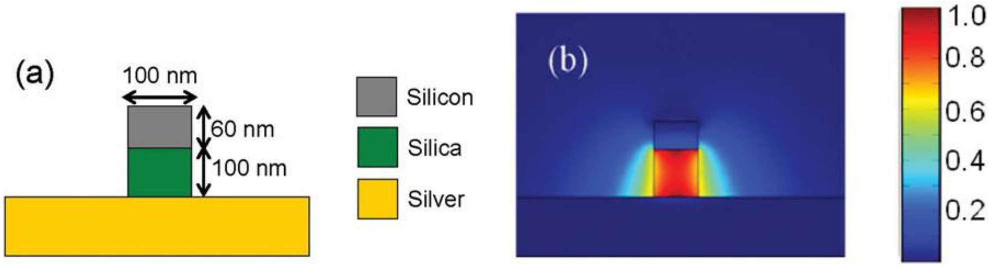

Fig. 13 a) The first proposed HPW based on a planar geometry, b) the power profile of the hybrid mode [41]

A year after, this Super-mode was called a hybrid plasmonic (HP) mode in the second pioneer work conducted by Oulton *et al*. [12]. This HP mode results from the strong coupling between the conventional dielectric mode and the SP mode. The hybrid mode has shown a favorable balance between mode confinement and propagation loss. Their work is based on a non-planar geometry. It consists of a cylindrical high-index dielectric nanowire (GaAs) adjacent to a metallic surface (silver) through a low index gap (silica) at the telecommunications wavelength 1550 nm as shown in Fig. 14(a). In their work, Oulton *et al*. explained the hybrid mode formation by using the coupled-mode theory, and divided the hybrid mode into two types: a SPP-like mode and a dielectric waveguide (DW)-like mode by controlling the geometrical dimensional parameters. Figure 14(b) shows the propagation length of the hybrid mode versus the diameter *d* of the high-index nanowire for different low-index gap width *h*. Their proposed HPW geometry has shown large propagation lengths (40-150 μm) with a strong mode confinement from $\boldsymbol{\lambda}^2/400$ to $\boldsymbol{\lambda}^2/40$ compared to the PWs.

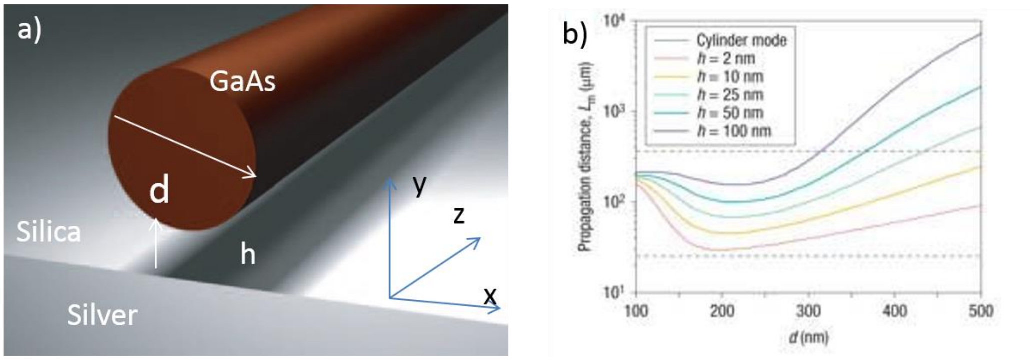

Fig. 14 a) The second proposed HPW based on a non-planar geometry, b) the propagation length of the hybrid mode versus the diameter *d* of the nanowire for different gap thicknesses *h* [12]

Even though both of the proposed structures have shown strong mode confinement and substantial improvements in the propagation length, the rectangular-based HPW is compatible with current nano-fabrication techniques and easier to integrate on-chips more than the cylindrical-based HPW.

The excellent features of the HP modes have driven researchers to propose different geometries and schemes of HPWs, based on theoretical [42-48] and experimental studies [49-50]. For example, a metal cap on a silicon on isolator SOI ridge HPW has been proposed by Dai *et al*. in 2009 shown in Fig. 15(a) [42]. They found that having a nano-scale 5 nm low-index spacer thickness with 50 nm ridge width can provide a better confinement with longer propagation length on the order of 100$\boldsymbol{\lambda}$, as well as their ease fabrication techniques which is compatible with SOI wafers. Another guiding scheme of the proposed HPWs is metallic V-grooves filled with a low-index gap dielectric and a high-index dielectric mediums shown in Fig. 15(b) [48]. Such a structure reveals a strong localized HP mode within the gap with long propagation length ranging from tens microns to hundred microns, and its compatibility with planar fabrication techniques.

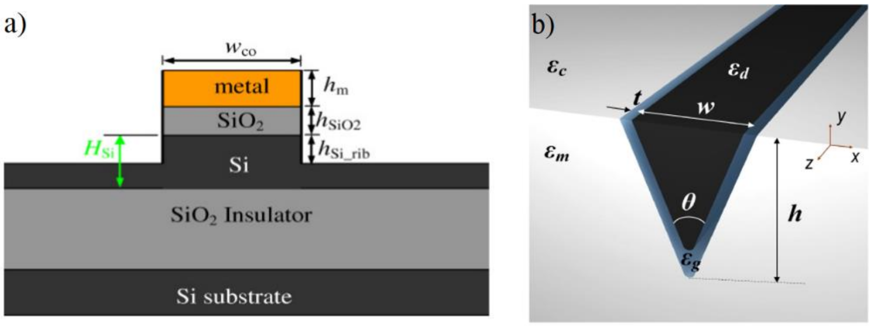

Fig. 15 Different proposed guiding schemes of HPWs, a) a metal cap on a SOI ridge [42], and b) metallic V-groove [48]

3.3.2 Dispersion equation of the Hybrid Plasmonic Mode

As previously mentioned, different geometries and structures have been considered in order to investigate hybrid plasmonic waveguides; however, all these theoretical studies were based on commercial mode solver software's based-results. The first theoretical study of a HPW based on a derived analytical equation was performed by Avrutsky *et al.* in 2010 [51]. They theoretically analyzed the guided modes in a conductor-gap-dielectric (CGD) system that consists of a low-index gap sandwiched by a conductor and a high-index dielectric layer. The authors explained why the low-index gap has to be nanoscale and that the role of the exact geometry of the high-index part in [12] is for lateral confinement, rather than hybridization and coupling of a SPP to a mode of cylinder.

The mode equation of the hybrid plasmonic waveguide can be derived by using the wave equation and applying the suitable boundary conditions, as done in the previous sections. A simple schematic of a simple 1D HPW is shown in Fig. 16; it consists of a low-index gap dielectric layer with a permittivity ϵ_g and gap thickness t inserted between a metal and high-index dielectric semi-infinite claddings with permittivities ϵ_m and ϵ_d, respectively, where the origin O point in the mid of the gap thickness. Assuming the hybrid mode is propagating in z-direction and the geometry is infinite in y-direction, so there is no y-field dependent for the hybrid guided mode. Since the hybrid mode is a plasmonic mode, so it has a TM polarization. Hence, there are three non-zero fields H_y, E_x, and E_z. By solving the wave equation Eq. 43 in each layer and using Maxwell's equations, the hybrid mode solutions can be expressed as:

$$H_y(x) = \begin{cases} Ae^{-k_d x}, \; x > \frac{t}{2} \\ Be^{-k_g x} + Ce^{k_g x}, -\frac{t}{2} < x < \frac{t}{2}, \\ De^{k_m x}, \; x < -\frac{t}{2} \end{cases} \tag{58}$$

$$E(x,y,z)\hat{x} = E_x(x)e^{i\beta z}\hat{x} = \begin{cases} -\frac{\beta A}{\omega \epsilon_d} e^{(i\beta z - k_d x)} \, (\hat{x}), \; x > \frac{t}{2} \\ -\frac{\beta}{\omega \epsilon_g} e^{i\beta z}\left(Be^{-k_g x} + Ce^{k_g x}\right) (\hat{x}), -\frac{t}{2} < x < \frac{t}{2}, \\ -\frac{\beta D}{\omega \epsilon_m} e^{(i\beta z + k_m x)} \, (\hat{x}), \; x < -\frac{t}{2} \end{cases} \tag{59}$$

and

$$E(x,y,z)\hat{z} = E_z(x)e^{i\beta z}\hat{z} = \begin{cases} \frac{iAk_d}{\omega \epsilon_0 \epsilon_d} e^{(i\beta z - k_d x)} \, (\hat{z}), x > \frac{t}{2} \\ \frac{ik_g}{\omega \epsilon_0 \epsilon_g} e^{i\beta z}\left(Be^{-k_g x} - Ce^{k_g x}\right) (\hat{z}), -\frac{t}{2} < x < \frac{t}{2}, \\ -\frac{iDk_m}{\omega \epsilon_0 \epsilon_m} e^{(i\beta z + k_m x)} \, (\hat{z}), \; x < -\frac{t}{2} \end{cases} \tag{60}$$

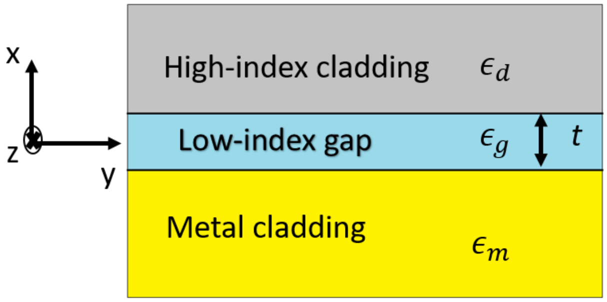

Fig. 16 A schematic diagram of the hybrid plasmonic waveguide structure

where wave number of the hybrid mode decaying fields into each region can written as:

$$k_i = \sqrt{\beta^2 - k_0^2 \epsilon_i}, \tag{61}$$

where $i = d, g,$ and $m,$ stands for dielectric, gap, and metal region. It can be noticed that the hybrid plasmonic waveguide has the same solutions as the DMD waveguide or MDM waveguide with different refractive indices. Hence, the dispersion relation of the hybrid plasmonic waveguide would have the same general formula of the DMD waveguide Eq. 44 or MDM waveguide Eq 52, with utilizing the suitable material optical properties. Therefore, the dispersion relation of the hybrid plasmonic mode can take the form

$$e^{2k_g t} = \frac{\left(\frac{k_g}{\epsilon_g} - \frac{k_m}{\epsilon_m}\right)\left(\frac{k_g}{\epsilon_g} - \frac{k_d}{\epsilon_d}\right)}{\left(\frac{k_g}{\epsilon_g} + \frac{k_m}{\epsilon_m}\right)\left(\frac{k_g}{\epsilon_g} + \frac{k_d}{\epsilon_d}\right)}. \tag{62}$$

It can be also simplified to

$$e^{k_g t} = \pm \sqrt{\frac{\left(\frac{k_g}{\epsilon_g} - \frac{k_m}{\epsilon_m}\right)\left(\frac{k_g}{\epsilon_g} - \frac{k_d}{\epsilon_d}\right)}{\left(\frac{k_g}{\epsilon_g} + \frac{k_m}{\epsilon_m}\right)\left(\frac{k_g}{\epsilon_g} + \frac{k_d}{\epsilon_d}\right)}}. \tag{63}$$

The dispersion equation of the hybrid mode, as seen, depends on the optical properties of each layer as well as the low-index gap thickness *t*. When the gap thickness shrinks to zero, the dispersion relation will approach to the single interface metal/high-index dielectric dispersion relation

$$n_{eff,\infty} = \sqrt{\frac{\epsilon_m \epsilon_d}{(\epsilon_m + \epsilon_d)}}. \tag{64}$$

3.3.3 Numerical Analysis and Discussion

3.3.3.1 The Modal Properties

The optical performance of the hybrid plasmonic waveguide can be studied by solving the dispersion equation of the LR hybrid plasmonic mode Eq. 63 numerically, and obtaining the basic optical descriptors of the hybrid mode: the modal index and the propagation length. Figure 17 illustrates the optical properties of the hybrid mode for two examples. The modal index and the propagation length of the hybrid mode for Silicon/Silica/Silver HPW at the telecommunications wavelength 1550 nm are shown in Fig. 17(a), where the refractive indices of the materials are $n_{\mathrm{Si}} = 3.455, n_{\mathrm{SiO_2}} = 1.445,$ and $n_{\mathrm{Ag}} = 0.1453 + 11.3587i.$ At zero gap thickness *t* of the silica layer, the modal index approaches to the modal index of a single interface Silver/Silicon surface plasmon mode $n_{\mathrm{eff},\infty}$. As the gap thickness increases, the modal index reduces dramatically until the curve converge to the refractive index of the high-index cladding (silicon) n_{Si}, where the cutoff gap thickness t_{cutoff} approached. Hence, the propagation length will be a maximum at the cutoff thickness and the loss minimum because the mode starts being a conventional dielectric mode localized in the high-index layer (silicon). The cutoff thickness of the hybrid mode can be obtained from LR-HP mode dispersion formula of Eq. 63 by assuming that the modal index of the hybrid mode n_{eff} approaching the refractive index of the high-index dielectric (silicon) layer $n_d = n_{\mathrm{Si}}$, so it can be expressed as:

$$t_{cutoff} = Re\left(\frac{\lambda}{4\pi\sqrt{n_d^2-n_g^2}}\, ln\left(\frac{n_m^2\sqrt{n_d^2-n_g^2}-n_g^2\sqrt{n_d^2-n_m^2}}{n_m^2\sqrt{n_d^2-n_g^2}+n_g^2\sqrt{n_d^2-n_m^2}}\right)\right). \tag{65}$$

Hence, the modal index range of the hybrid plasmonic mode is between the modal index of the single interface Si/Ag surface plasmon mode $n_{eff,\infty}(\mathrm{Si/Ag})$ and the refractive index of the high-index dielectric mode n_{Si} where the cutoff gap thickness reached, as shown in Fig. 17(a). Thus, the hybrid mode needs only a few nanometers gap thicknesses in order to reduce the modal index of $n_{eff,\infty}(\mathrm{Si/Ag})$ to the refractive index of n_{Si}, so the cutoff gap thickness here is very small a few nanometers 4.7 nm, where the index contrast is large between the high-index dielectric (silicon) and the-index gap dielectric (silica) layer $(n_{\mathrm{Si}}/n_{\mathrm{SiO2}})=2.39$. This explains how the hybrid mode is compressed in a sub-wavelength size in the low-index gap region. As the index contrast decreases, the cutoff thickness increases to a few tens nanometers around 46 nm as illustrated in Fig. 17(b) where the hybrid plasmonic waveguide materials are Germanium (high-index, $n_{\mathrm{Ge}}=4.275$), silicon (low-index gap), and silver (metal) at the wavelength 1550 nm. In addition, the propagation length of the hybrid mode increases as the gap thickness increases until it maximizes infinitely at the cutoff thickness as shown in Fig. 17 (Right), so the hybrid mode has lower loss compared to the single interface metal/dielectric loss. For example, the propagation length of the SPPs mode at Si/Ag interface is 26 µm, and the propagation length for Ge/Ag interface's SPPs mode is ~13 µm. These short propagation lengths of the SPPs mode at the metal/dielectric interface reflects the high loss that PWs suffering from, whereas the propagation length range of the hybrid mode is between tens microns to a hundred microns which is much better than pure SPPs modes. These propagation lengths of the hybrid mode are reasonably acceptable for on chips nano-plasmonic devices, which is considered to be a few hundred nanometers a cross.

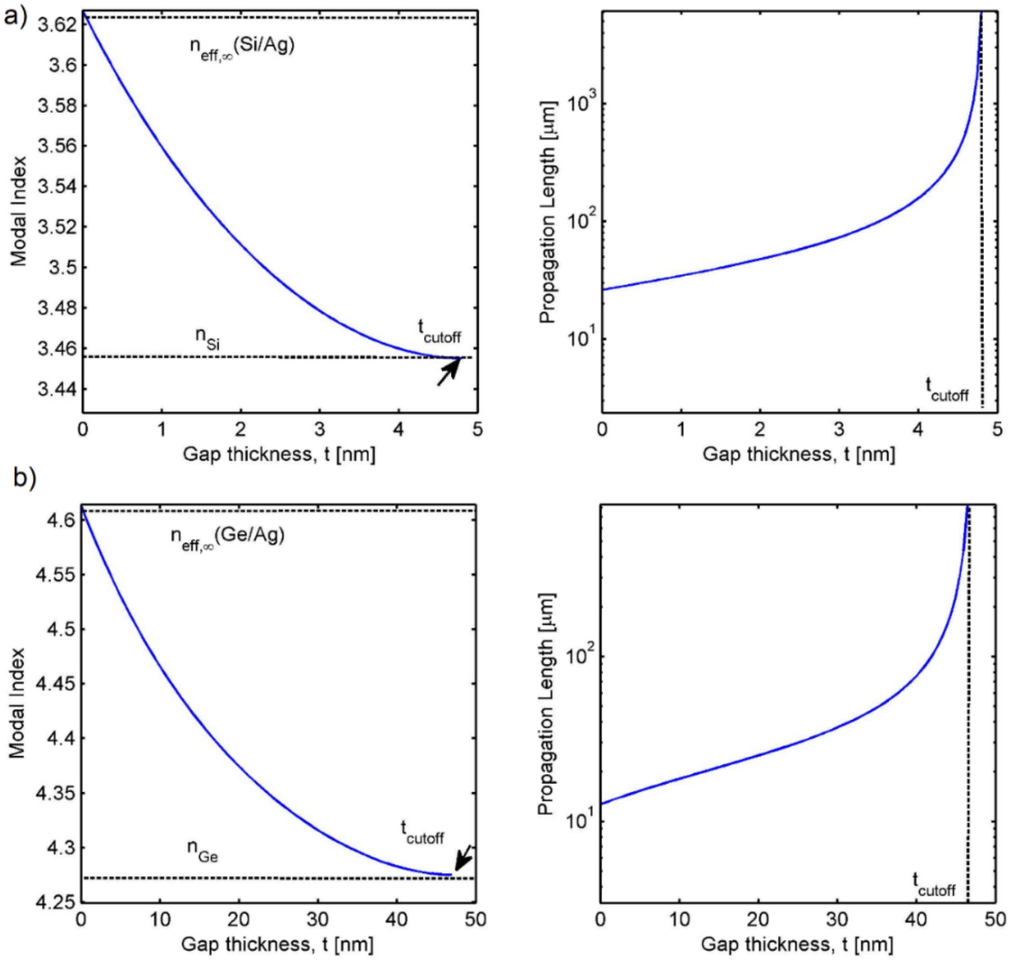

Fig. 17 The modal index and the propagation length versus the gap thickness *t* of the a) Silicon/Silica/Silver, and b) Germanium/Silicon/Silver hybrid plasmonic waveguides at 1550 nm

3.3.3.2 The Energy Flux Density Profile of the Hybrid Mode

The power density of the hybrid mode flowing in the *z*-direction can be plotted by using the transverse field components Eq. 57 and Eq. 58, and the energy flux density (the time average of the z-component of the pointing vector):

$$S_z = \frac{1}{2} Re\left(\vec{E} \times \vec{H}^*\right) \cdot \hat{z}. \tag{66}$$

Figure 18(a) shows the propagating power of the hybrid mode at different gap thicknesses t for the (Ge/Si/Ag) hybrid plasmonic waveguide. At very small gap thickness t=5 nm, the power density is highly maximized within the gap region (Silicon) layer and decays into the cladding regions. This noticeable field enhancement within the gap can be explained simply from the continuity of the normal electric displacement fields at the interfaces of the gap (Si) and the high-index dielectric (Ge) materials; $\epsilon_g E_{x,g} = \epsilon_d E_{x,d}$. Thus, the electric field localized in the gap is 1.54 times the electric field confined within the high-index layer.

Therefore, having large index contrast between the gap and the dielectric layers will improve the field enhancement greatly within the gap. Figure 18(b) shows the power profile of the hybrid mode at large index contrast Si/SiO$_2$ at different gap thicknesses t=1, 3, and 4 nm, so it can be seen how the field is highly localized within the gap (SiO$_2$); it is almost 6 times the field residing within the high-index dielectric layer (Si) . At the metal/gap interfaces, the continuity of the normal component of the electric fields requires that $\epsilon_m E_{x,m} = \epsilon_g E_g$. Since the metal permittivity has a negative real part, the power field direction is flipping at the metal/low-index gap interface as shown clearly in Fig. 18 (a), and rapidly decaying in the metal clad because the high propagation loss of metals at optical frequencies. As the gap thickness increases in the two cases of Fig. 18, the power field confined within the gap region decreases. As a result, subwavelength nano-gap thicknesses can provide strong field confinement with a moderate propagation length.

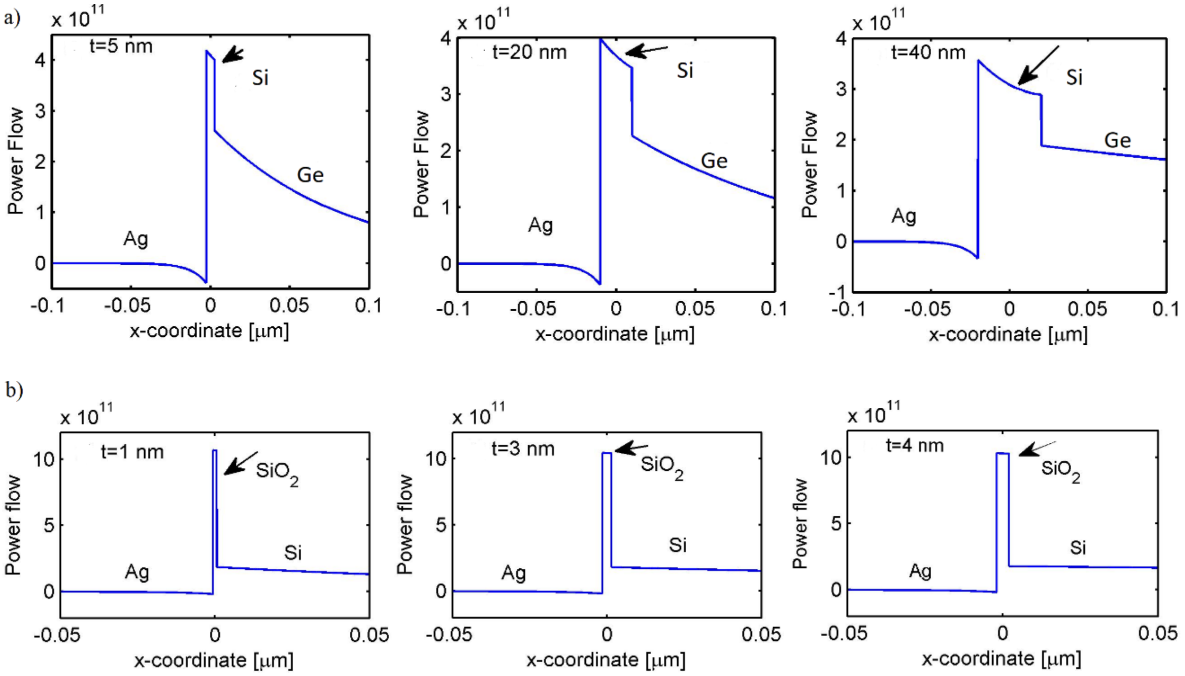

Fig. 18 The energy flux density of the hybrid mode in a) the (Ge/Si/Ag) HPW at different gap thicknesses *t*=5, 20, and 40 nm, b) at high index contrast Si/SiO_2/Ag HPW at gap thicknesses *t*=1, 3, and 4 nm

Moreover, the FEM mode solver has been used to examine the hybrid plasmonic mode's electric field in one and two dimensions, and to realize how the gap cutoff thickness t influences the hybrid mode's formation. Figure 19 and Fig. 20 show one and two dimensional plot for electric field of the (Ge/Si/Ag) hybrid plasmonic mode at different gap thicknesses *t*=10, 30, 50, and 70 nm. At small gap thicknesses such as *t*=10 and 30 nm, we can see the hybrid mode's field is highly compressed within the low-index gap layer and decaying away into the cladding regions (Ge and Ag layers), and the field confinement within the gap decreases as the gap thickness increases. Referring back to Fig. 17(b) where the optical performance of the (Ge/Si/Ag) hybrid plasmonic waveguide has been investigated, we found that the hybrid mode supported by such a structure has a gap thickness $t_{cutoff} \approx 46$ nm. Thus, when the gap thickness is smaller than the cutoff thickness, the field highly concentrated within the gap as in the cases *t*=10 and 30 nm. However, as the gap thickness increases to 50 and 70 nm exceeding the cutoff gap thickness as illustrated in Fig. 19 and Fig. 20, we observe how the E-field of the hybrid mode noticeably leaks to the high-index region, and the leakage increases as the gap thickness increases.

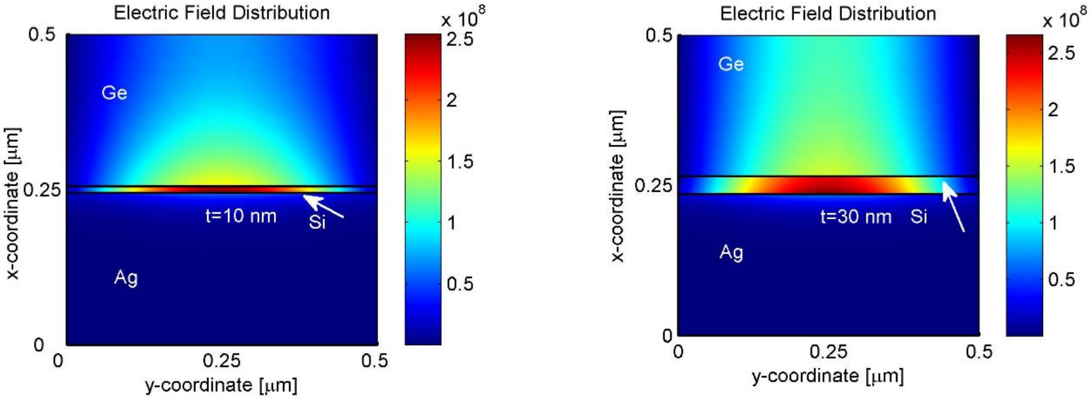

a) t=10 nm

b) t=30 nm

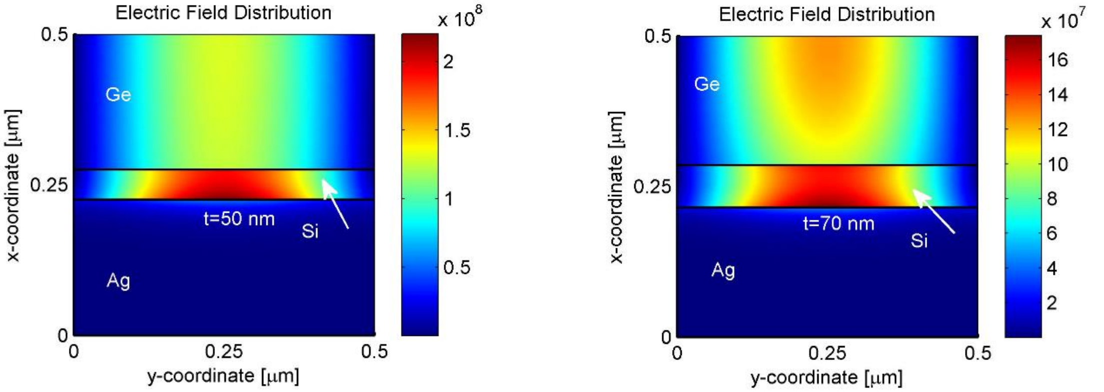

c) t=50 nm

d) t=70 nm

Fig. 19 The 2D electric field for the hybrid plasmonic mode at different gap thicknesses *t*=10, 30, 50, and 70 nm

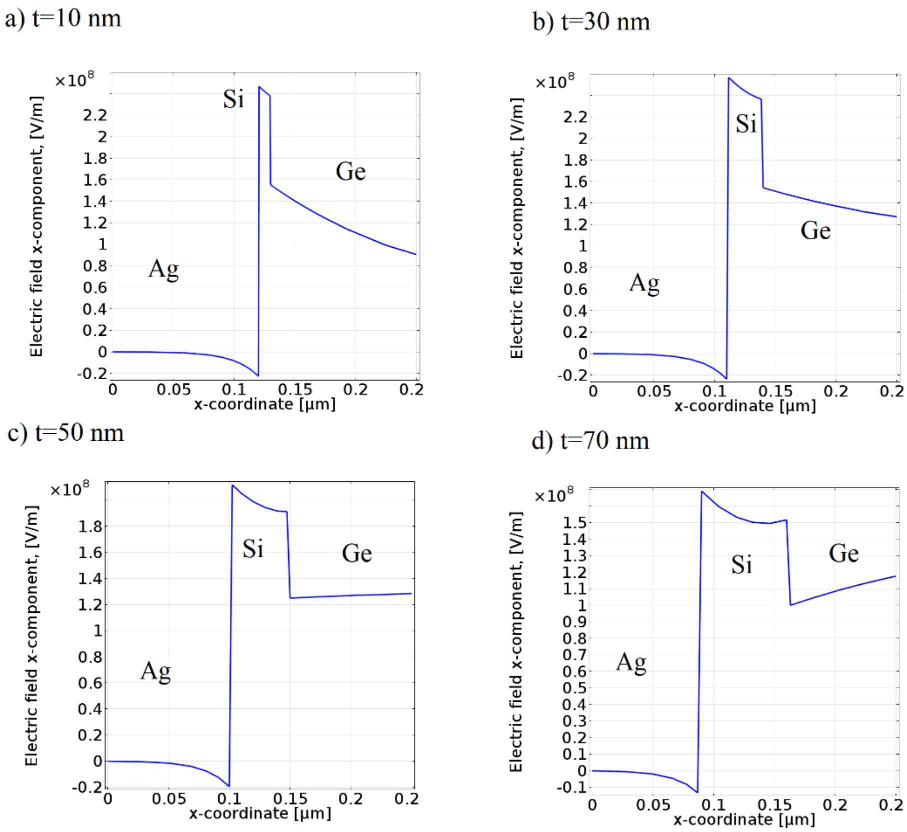

a) t=10 nm

b) t=30 nm

c) t=50 nm

d) t=70 nm

Fig. 20 The electric field of the hybrid guided mode as a function of *x* at different gap thicknesses a) t=10, b) t=30, c) t=50, and d) t=70 nm

3.3.4 Applications of Hybrid Plasmonic Waveguides

There is a great attention has been paid to the hybrid plasmonic waveguides HPWs in recent years because of their crucial features to confine light strongly within sub-wavelength nano-scale structures beyond the diffraction limit with lower propagation loss compared to other purely plasmonic waveguides, and their compatibility with the SOI and CMOS fabrication techniques. Many research studies have been conducted to exploit the strengths of HPWs in different applications. One of the HPWs promising applications is constructing highly-dense plasmonic integrated circuits, which can have superior data transmission rate, low power consumption, and minuscule size [52]. Different components of plasmonic integrated circuits based on HPWs have been proposed and investigated such as power splitters [53], ring resonators [54], and directional couplers [55]. Since data processing within electronic integrated circuits is performed nonlinearly in order to route, modulate, and switch data, there has been much interest to perform nonlinear all optical data-processing devices. The great field enhancement achieved within the low-index gap of hybrid plasmonic waveguides makes them excellent candidates to perform nonlinear optical devices which require high field intensity, low power, and very small switching time. For this purpose, various hybrid plasmonic waveguides have been proposed and studied for nonlinear devices [56-63]. Another important application of HPWs which has been investigated experimentally and theoretically is building active nanoscale devices such as nanolasers [64-68]. Utilizing HPWs for biosensing applications has gained much interest recently [69-71].

Chapter 4

Hybrid Multilayered Dielectric-Metal-Dielectric Waveguides

Although the SPPs modes supported by the fundamental metal-dielectric interface structure have shown superior merits to confine light beyond diffraction limit, it suffers from high propagation loss due to the intrinsic Ohmic loss in metal [72]. To reduce the propagation loss, symmetrical structures such as Dielectric-Metal-Dielectric (DMD) [73-74] and Metal-Dielectric-Metal (MDM) waveguide structures have been proposed; unfortunately, the improvement in propagation loss in the DMD structure comes at the price of the modal field confinement and vice versa in the MDM structure, as discussed previously.

Hybrid plasmonic waveguides (HPWs) have been proposed as a solution to the propagation loss issue of plasmonic waveguides. They have gained consideration as one of the most promising plasmonic structures as they can support hybrid plasmonic modes that have extremely strong field confinement within a nanometer scale gap while maintaining a relatively long propagation distance compared to purely plasmonic waveguides. Symmetrical hybrid SPP waveguide structures have been proposed to further improve the propagation distance and the field confinement of the guided SPP modes. For example, symmetrical hybrid plasmonic waveguides with two high-index nanowires [75] and rectangular slabs [76] have been proposed. Both of them have shown simultaneous improvement in propagation loss and modal confinement.

Most of the theoretical studies are based on using simulation software in order to study the hybrid guided mode and its optical properties. Understanding the hybrid mode deeply requires analytical theoretical studies in order to study all the factors that may enhance the waveguide performance accurately, which can help the waveguide designers for the fabrication of the plasmonic devices. For example, the mode equation for a planar 3-layer conductor-gap-dielectric waveguide (CGD), which consists of a low-index dielectric gap inserted between an infinite conductor layer and an infinite high-index dielectric layer, has been derived by Avrutsky *et al*. [51]. They analyzed the hybrid mode and explained the physical reason for the requirement of nanoscale gap for the existence of the hybrid plasmonic mode. Although the mode equation for the hybrid mode of a three-layer planar PW has been derived and studied, there is a lack of theoretical studies based on analytical equations for the characterization of the hybrid mode of multilayer HPWs. In this dissertation, we present comprehensive theoretical studies for the hybrid modes guided by multilayered hybrid plasmonic waveguides based on derived-analytical equations. In this chapter, we present two thorough analytical-theoretical studies for five and seven layers hybrid-DMD plasmonic waveguides by deriving their dispersion equations, studying their optical performance, plotting their optical fields' profile, analyzing the mode characteristics, including the confinement factor, utilizing figures of merit, as well as using a commercial software for more investigations [77-78].

4.1 Theoretical Study of Plasmonic Modes in a Symmetric Conductor-Gap-Dielectric waveguide

We present a theoretical analysis of the guided SPP modes of a symmetric conductor-gap-dielectric system (SCGD) that is constructed with a conductor metal strip sandwiched symmetrically with a low-index gap and high-index cladding layer on both sides. The dispersion relation of the guided mode by such a structure is derived to investigate the optical performance in the SCGD system. As well as, we explain the existence of the cutoff gap thickness and present an approximate analytical expression for its estimation. Contrary to the CGD system, where the cutoff gap thickness is fixed [51], we investigate the effect of the metal thickness and the index contrast ratio of the cladding high-index layer to the low-index gap layer on the cutoff thickness of the low-index gap region. The optical fields guided by such a structure are plotted based on our analytical equations. Moreover, we present the simulation results for the characterization of the guided mode, including the modal index, propagation distance, gap cutoff thickness, optical fields' power, and electrical field confinement within the gap. The lateral confinement of the SCGD mode is also discussed. The guided modes supported by the SCGD waveguide structure have been characterized for relatively low index contrast ratio by another approach based on the reflection pole method [79]. However, our study is based on analytical derived equations, focused on the high-index-contrast ratio structure, which enables an extremely strong field confinement within a nano-scale low-index gap, making the SCGD structure an excellent plasmonic waveguide for fabricating active and passive plasmonic devices, such as surface-plasmon nano-lasers [80], and all-optical switchers using nonlinear effects [81].

4.1.1 Theoretical Model

4.1.1.1 Dispersion equation

A schematic diagram of the SCGD plasmonic waveguide structure is shown in Fig. 21, which consists of a center conductor layer sandwiched between two low-index dielectric gaps that cladded with semi-infinite high-index dielectric layers on both sides. The conductor thin film has a thickness of d and permittivity of ε_m. Each low-index gap has a thickness of t and refractive index of n_g, and the refractive index of the high-index cladding is denoted as n_d. Both the low-index and high-index dielectric layers are assumed to be lossless, and all the materials are considered homogeneous, nonmagnetic and isotropic. The SCGD waveguide architecture is simply a modified DMD structure with the insertion of two low-index dielectric gap layers inside. Without the gap layers, i.e., $t = 0$, it becomes a traditional DMD waveguide, which supports two SPPs modes: the LRS-DMD mode and SRA-DMD mode.

With the insertion of the gap layers, due to the large index contrast ratio of the cladding layer to gap layer, the guided mode in the SCGD system, referred to as the SCGD mode, is strongly confined in the gap layers with reduced propagation loss if the gap thickness is sufficiently narrow. The largest gap thickness for which SCGD mode can propagate is called cutoff gap thickness, i.e. the SCGD mode occurs only if the gap thickness is smaller than the cutoff gap thickness, which will be discussed in details theoretically.

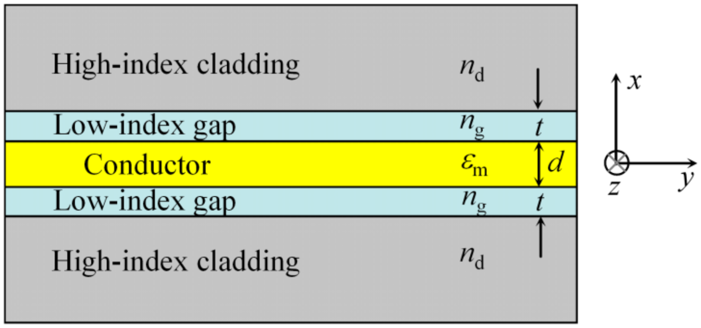

Fig. 21. Schematic diagram of the 1D symmetric conduct-gap-dielectric (SCGD) structure

We assume the 1D model is infinite in y-direction, so there is no dependence on the lateral dimension y, and the guided mode propagates in the z-direction. The SCGD waveguide only supports transverse magnetic (TM) modes, where the non-zero field components are H_y, E_x, and E_z. All the fields assumed to have time-harmonic form, for the SPP propagation in the *z* direction, the wave equations for magnetic field can be simplified to Helmholtz's equation, given by

$$\frac{\partial^2 H_y}{\partial x^2} - (\beta^2 - k_0^2 \varepsilon_r) H_y = 0, \tag{67}$$

where β is the propagation constant of the guided mode, ε_r stands for the relative permittivity of the media (i.e, the gap, cladding, or metal film), $k_o = 2\pi/\lambda$ is the wave vector of the propagating wave, and λ is the wavelength in vacuum. Equation (67) is a partial differential equation, from which a corresponding function of the solution H_y is constructed for different media. By using Maxwell's equations, the tangential and normal electric fields components can be obtained from H_y by using the following relations:

$$E_x = \frac{\beta}{\omega \varepsilon_0 \varepsilon_r} H_y \tag{68}$$

and

$$E_z = -\frac{j}{\omega \varepsilon_0 \varepsilon_r} \frac{\partial H_y}{\partial x}. \tag{69}$$

The boundary conditions must be satisfied at the materials interfaces. That means, the tangential components of the electric and magnetic fields E_z and H_y, and the normal component of the electric displacement field D_x are continuous. By applying the appropriate the boundary conditions, the dispersion relation of the SCGD waveguide can be obtained

$$e^{k_m d} = \pm \frac{\frac{k_m \varepsilon_g}{k_g \varepsilon_m} \cdot \frac{1+r}{1-r} + 1}{\frac{k_m \varepsilon_g}{k_g \varepsilon_m} \cdot \frac{1+r}{1-r} - 1}, \tag{70}$$

with

$$r = e^{2k_g t} \frac{\frac{k_g}{\varepsilon_g} + \frac{k_d}{\varepsilon_d}}{\frac{k_g}{\varepsilon_g} - \frac{k_d}{\varepsilon_d}} \tag{71}$$

and

$$k_i^2 = \beta^2 - k_0^2 \varepsilon_i, \tag{72}$$

where $i = m, g,$ and $d,$ standing for metal, gap, and dielectric layers, respectively. The relative permittivites are related to refractive indices by $\varepsilon_i = n_i^2$. The positive sign of the dispersion relation Eq. 70 corresponds to the fundamental transverse magnetic TM symmetrical LRSPP hybrid-DMD mode, whereas the negative sign one refers to anti-symmetrical SRSPP hybrid-DMD mode. Here, we study only the LRSPP hybrid-DMD mode due to its low propagation loss. The dispersion equations of the hybrid-DMD modes can be re-expressed in transcendental forms as:

$$\tanh\left(\frac{k_m d}{2}\right) = \frac{k_g \varepsilon_m (1-r)}{k_m \varepsilon_g (1+r)}, \tag{73}$$

for the positive sign, and

$$\tanh\left(\frac{k_m d}{2}\right) = \frac{k_m \varepsilon_g (1+r)}{k_g \varepsilon_m (1-r)}, \tag{74}$$

for the negative sign.

When there is no low-index gap layers, the dispersion equations 70, 73, and 74 can be simplified as:

$$e^{k_m d} = \pm \frac{\frac{k_m}{\varepsilon_m} - \frac{k_d}{\varepsilon_d}}{\frac{k_m}{\varepsilon_m} + \frac{k_d}{\varepsilon_d}}, \tag{75}$$

$$\tanh\left(\frac{k_m d}{2}\right) = -\frac{k_d \epsilon_m}{\epsilon_d k_m}, \tag{76}$$

$$\tanh\left(\frac{k_m d}{2}\right) = -\frac{k_m \epsilon_d}{\epsilon_m k_d}. \tag{77}$$

As noticed, these equations are equivalent perfectly to the characteristic mode equations Eq. 40 - Eq. 51 of the DMD plasmonic waveguides discussed in the previous chapter. The positive sign of the mode equation represents the LRSPP DMD mode, and the negative sign corresponds to the SRSPP DMD mode.

4.1.1.2 Cutoff condition for the guided SCGD mode

In order to understand how to form the guided mode in the SCGD structure – $\mathrm{D_{high}}$/$\mathrm{D_{low}}$/Metal/ $\mathrm{D_{low}}$/$\mathrm{D_{high}}$, the special case when the gap thickness $t = 0$ will be considered. Thus, this waveguide structure becomes the traditional DMD structure that is formed by a thin metal film surrounding with high-index cladding layers – $\mathrm{D_{high}}$/Metal/$\mathrm{D_{high}}$. The modal index of the $\mathrm{D_{high}}$/Metal/$\mathrm{D_{high}}$ system determined by Eq. 76 is larger than the index of the cladding layer. As the metal film thickness increases, the modal index will be greater and propagation length smaller. By introducing symmetric thin dielectric low-index gap layers, the modal index and the propagation loss of the SCGD system start to decrease. When increasing the thickness of the gap, the modal index and propagation loss continue to decrease until the gap reaches a maximum thickness where the real part of the modal index is equal to the index of the cladding layer and the propagation loss reaches its minimum. Beyond the maximum gap thickness, the mode shows substantial leakage into the high-index cladding layer. This represents the cutoff condition for the guided SCGD mode, and this maximum gap thickness is referred as the cutoff gap thickness.

The cutoff gap thickness t_{max} can be numerically solved from the transcendental dispersion equation Eq. 73. On the other hand, it would be convenient and meaningful for waveguide designers to be able to find a reliable estimate of t_{max} without resort to complicated numerical calculations. By setting the modal index equal to the index of the cladding layer and assuming zero propagation loss for the guided mode (which is very reasonable due to the minimum propagation loss at cutoff condition), an approximate analytical expression for the cutoff gap thickness can be written as:

$$t_{max} = \frac{1}{k_g} tanh^{-1}\left(-\frac{k_m \varepsilon_g}{k_g \varepsilon_m} tanh\left(\frac{k_m d}{2}\right)\right) \qquad (78)$$

with $k_g = k_0\sqrt{\varepsilon_d - \varepsilon_g}$ and $k_m = \sqrt{\varepsilon_d - \varepsilon_m}$. $k_m = k_o\sqrt{\varepsilon_d - \varepsilon_m}$.

It can be seen from Eq. 78, the cutoff gap thickness of the SCGD mode depends on the metal film thickness d, and the materials optical properties of the gap and cladding layer, the permittivity of the metal film, as well as the wavelength of the propagation wave. When the metal film thickness is thin, the cutoff gap thickness will be smaller. In addition, having large index contrast (the ratio of n_d to n_g)

will decrease the cutoff thickness. When the thickness of the metal film *d* is considered to be very small, the cutoff gap thickness equation Eq. 78 can be simplified to:

$$t_{max} \approx \frac{d}{2\left(n_d^2/n_g^2-1\right)}. \tag{79}$$

For instance, if the metal thickness is 30 nm, and the index contrast ratio n_d/n_g, is 1.5, then from the estimate of the cutoff gap thickness $t_{\max}$ will be 12 nm. As the contrast index ratio increased to 2.39 (by using n_{Si}/n_{SiO2} at the wavelength 1550 nm), then the allowable cutoff gap thickness $t_{\max}$ is reduced to 3.2 nm. From Eq. 79, we can clearly see that $t_{\max}$ is proportional to the metal thickness. Therefore, the cutoff gap thickness can be controlled by the index contrast ratio and the metal thickness.

The case we considered, thus far, is for high index contrast ratio, where the cutoff gap thickness $t_{\max}$ to have guided SCGD mode is in the nanoscale range. However, when the index contrast ratio reduced by fixing n_g while decreasing n_d, then the cutoff thickness will increase. For the extreme case where $t_{\max} \to \infty$, the dispersion equation of the SCGD guided mode Eq. 73 can be written as:

$$\tanh\left(\frac{k_m d}{2}\right) = -\frac{k_g \epsilon_m}{\epsilon_g k_m}, \tag{80}$$

As seen, Eq. 80 is simply the dispersion equation for a low-index-metal-low-index (LML) plasmonic waveguide structure. Thus, at $t_{\max} \to \infty$, the modal index of the SCGD structure is actually the modal index for a gap/conductor/gap structure, determined by Eq. 80. Recall that to derive the approximate analytical expression for the cut off condition of the SCGD mode, the modal index is set equal to the cladding index n_d. Therefore, to have guided SCGD mode, the cladding index n_d has to be larger than the modal index of the gap/conductor/gap structure based on Eq. 80, which depends on the metal thickness. This conclusion is in agreement with Eq. (1) in ref. [79]. As well as, by fixing the high-index n_d, the metal film has to be (very thin) smaller than the thickness determined by Eq. 80 to ensure the existence of the SCGD mode within the low index gap.

4.1.2 Numerical Analysis and Discussion

4.1.2.1 The Modal Properties

In order to study the optical behavior of the SCGD guided mode, we need to solve the mode equation numerically to obtain the optical properties of the guided mode such as the modal index and the propagation length. The effect of the index contrast ratio n_d/n_g on the cutoff gap thickness will be investigated by using three different combinations of the cladding/gap materials – Ge/Si, CdS/MgF_2 and Si/SiO_2. The refractive indices of Ge, Si, CdS, MgF_2 and SiO_2 at the telecom wavelength 1550 nm are 4.275, 3.455, 2.3, 1.37, and 1.445, respectively. Hence, the index contrast ratios are 1.237, 1.678 and 2.391 for the combinations Ge/Si, CdS/MgF_2 and Si/SiO_2, respectively. In the SCGD structure, the conductor has been chosen to be silver (Ag) and gold (Au) for the sake of comparison, where their permittivities are $\varepsilon_{Ag} = -129 + 3.3j$ and $\varepsilon_{Au} = -115.11 + 11.103j$ [26]. By solving Eq. 73, we can obtain the modal properties of the SCGD guided mode: the modal index and the propagation length.

The modal index and propagation distance versus the thickness of the low-index gap layer, at different metal film thicknesses and various cladding/gap materials, are shown in Fig. 22, where the solid and dotted lines correspond to the silver and gold, respectively. Three different index contrast cladding/gap materials are analyzed: Ge/Si, CdS/MgF_2, and Si/SiO_2, respectively, at various metal thicknesses d=10, 20, 30, 40, and 50 nm.

It is worth noting that utilizing silver film results in lowering the propagation loss because the Ohmic loss of the silver is smaller than that of gold. As the gap thickness increases, we can see the modal index decreasing and the propagation length increasing. Increasing the gap thickness further leads to all curves for the modal index approaching to the index of the cladding layer, where the cutoff gap thickness is reached. At the cutoff gap thickness, the propagation length is maximized leading to a remarkable reduction in the propagation loss.

Moreover, the cutoff gap thickness changes with the metal film thickness. Reducing the metal thickness results in having a smaller cutoff thickness and a longer propagation length. The physical reason behind that is with a thinner metal film, at zero gap the modal index is only slightly above the cladding index, which suggests that only a thin low-index gap is required to bring the modal index down to the cladding index. Because of the intrinsic Ohmic loss of the conductor material, a thinner metal film will have a smaller overlap with the SCGD mode, yielding to longer propagation distance.

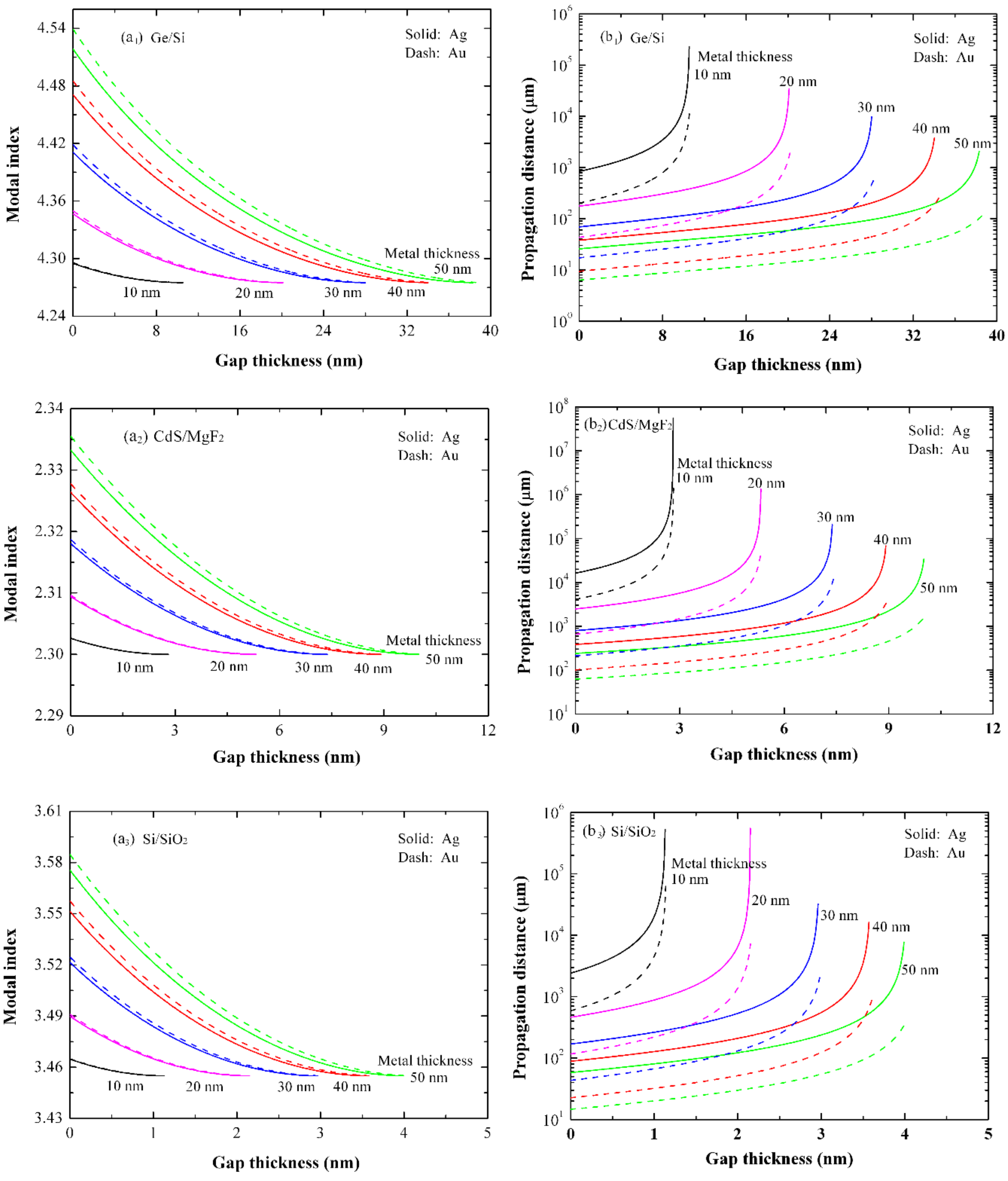

Fig. 22 (a$_1$) – (a$_3$) SCGD modal index and (b$_1$) – (b$_3$) propagation distance as a function of gap thickness for different metal thickness. Solid and dotted lines represent silver and gold respectively. Cladding/gap materials are Ge/Si for [(a$_1$), (b$_1$)], CdS/MgF$_2$ for [(a$_2$), (b$_2$)], and Si/SiO$_2$ for [(a$_3$), (b$_3$)], respectively.

Our simulation results based on our analytical expression are in agreement with those in ref. [79] which is based on a different approach, as well as verified by using the commercial finite element-based software COMSOL Multiphysics 4.3b. By using COMSOL's mode solver, the modal index and the propagation length at different metal thicknesses *d*=20, 30, and 40 nm for SCGD guided mode by the Ge/Si/Ag/Si/Ge waveguide structure at 1550 nm are shown in Fig. 23. They are similar results to that (in Fig.22) based on analytical equations. For the same waveguide structure, at metal thickness *d*=30 nm, the electric field for the SCGD guided mode has been investigated in 1D and 2D, for different gap thicknesses *t*=15, 20, 25, and 35 nm, as illustrated in Fig. 24 and Fig. 25. It can be seen that how the field highly concentrating within the low-index gap (Si) at *t*=15 nm as shown in the surface plot (Fig. 24(a)) and clearly the correspondence 1D plot Fig. 25(a), respectively. Then, the electric field starts decreasing as the gap thickness increasing *t*=20 and 25 nm (Fig. 24 and Fig. 25 (b and c)). We can see how the SCGD guided mode shows leakage into the cladding layers when the gap-thickness *t*=35 nm is larger than the cutoff gap thickness, which is $t_{max} \sim 30\ nm$, as illustrated in Fig. 24(d) and Fig. 25 (d).

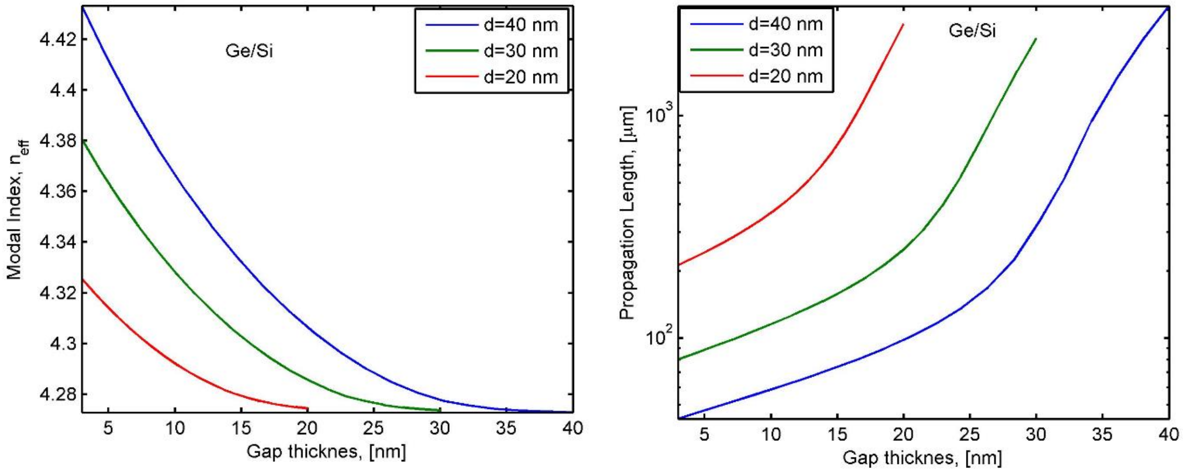

Fig. 23 The modal index (left) and the propagation length (left) for the guided mode by Ge/Si/Ag/Si/Ge structure at 1550 nm, by using commercial mode solver

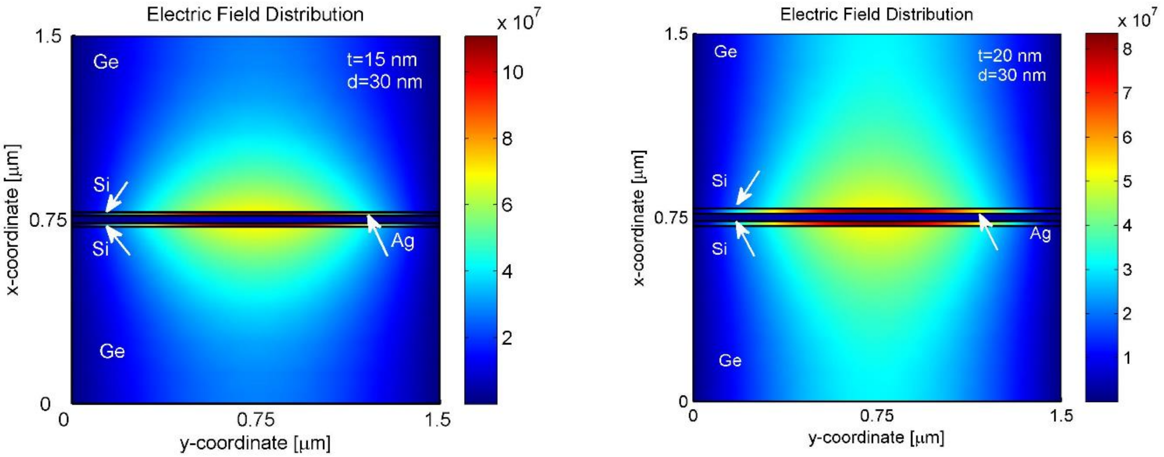
a) t=15 nm

b) t=20 nm

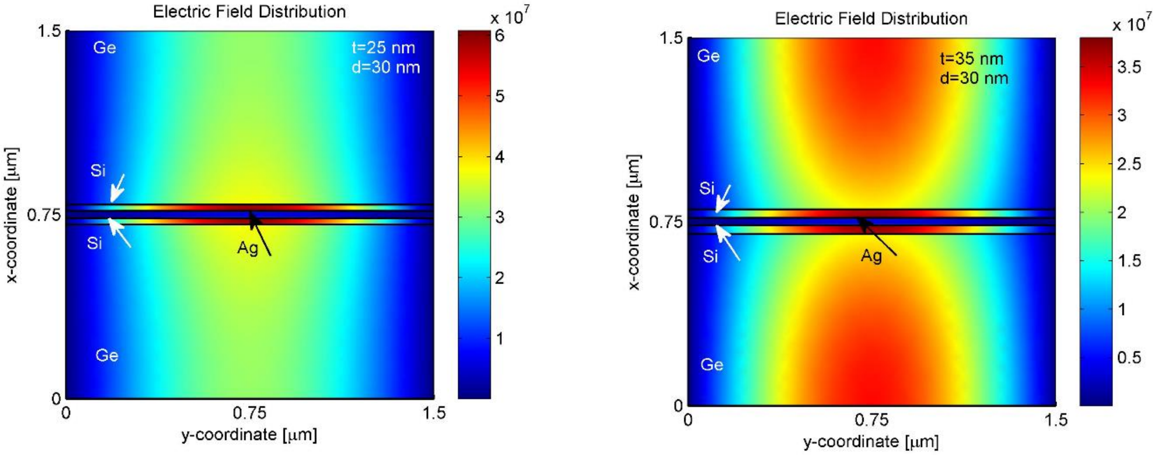
c) t=25 nm

d) t=35 nm

Fig. 24 The surface plot of the Electric field of the SCGD guided mode for Ge/Si/Ag/Si/Ge structure at *d* =30 nm for different gap thicknesses *t*=15, 20, 25, and 35 nm

a) t=15 nm

b) t=20 nm

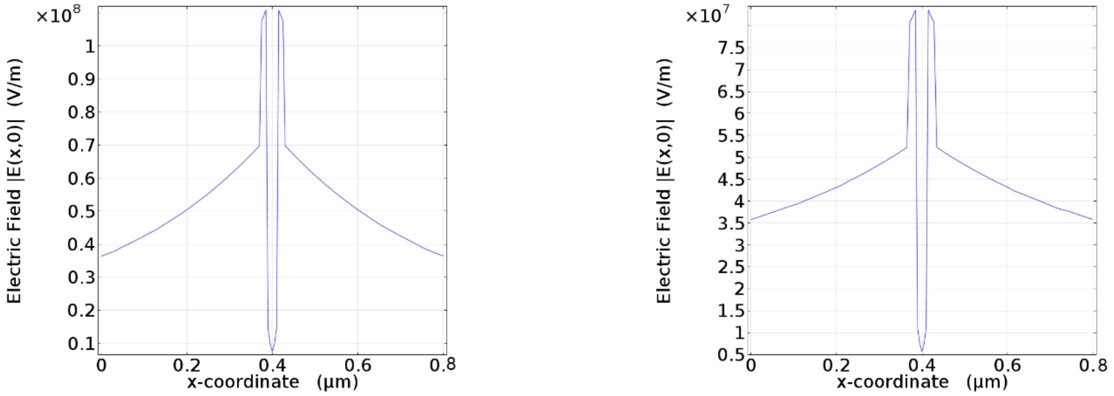

c) t=25 nm

c) t=35 nm

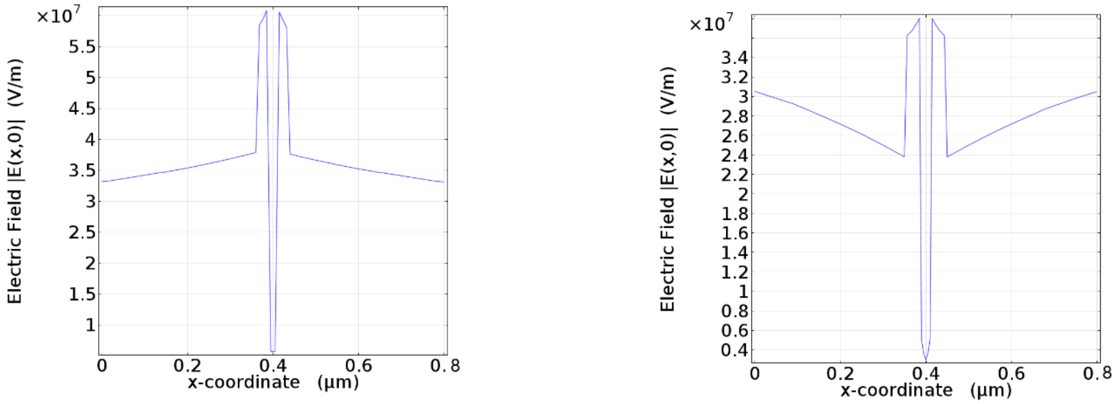

Fig. 25 The 1D plot of the Electric field of the SCGD guided mode $|\vec{E}(x,0)|$ for Ge/Si/Ag/Si/Ge structure at *d* =30 nm for different gap thicknesses *t*=15, 20, 25, and 35 nm

4.1.2.2 The effect of the index contrast on the cutoff gap thickness

Figure 26 shows the cutoff gap thickness versus metal thickness for three different cladding/gap materials in order to see how the cutoff gap thickness is controlled by the index contrast ratio of the cladding/gap layers. The solid line illustrates the numerical solution of the dispersion equation Eq. 73, and the dash line corresponds to the results based on the approximate analytical expression Eq. 78 of the cutoff gap thickness The study are performed for two metal films, silver and gold in Fig. 26(a) and Fig. 26(b) respectively. We can clearly see that the results Fig. 26(a) and 26(b) are very similar because the mode overlap with the metal is very small at the cutoff condition. In addition, it can be noticed having large index contrast ratio results in decreasing the cutoff gap thickness. However, as the metal thickness increases, the cutoff gap thickness increases. Furthermore, almost there is no difference between the exact and the approximate results for silver film compared with that for gold film. This attributes to the analytical expression of the cutoff gap thickness is based on the assumption of zero propagation loss for the guided mode. Without doubt, the analytical expression of the cutoff gap thickness is more accurate for the silver film than that for gold film because the Ohmic loss of silver is less than that of gold.

Typically, the approximate analytical expression’s results agree reasonably well with the one from the numerical calculation of the dispersion equation. When the index contrast ratio is high, such as 1.68 and 2.39 for CdS/MgF_2 and Si/SiO_2, respectively, the curves based on two different approaches are almost overlap. However, for a relatively low index contrast ratio such as 1.22 for Ge/Si, the approximate expression works well only when the metal thickness is less than 30 nm for silver and 15 nm for gold. As a result, the analytical expression for cutoff gap thickness in Eq. 78 can be used as a practical estimate for the design of the SCGD waveguide for utilizing cladding/gap materials with a large index contrast ratio.

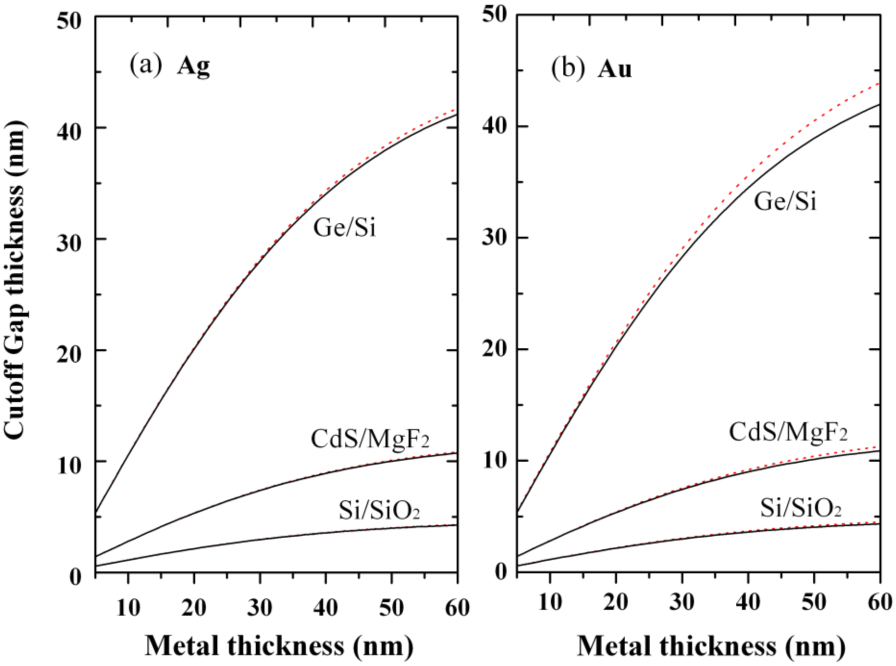

Fig. 26 Cutoff thickness versus metal thickness for different index contrast ratio. Solid and dashed lines represent the numerical result obtained from dispersion equation Eq. 78 and cutoff gap thickness Eq. 79. (a) and (b) are respectively for Ag and Au.

Moreover, the simplified expression for the cutoff gap thickness in Eq. 79 is investigated. Figure 27 shows the cutoff gap thickness by using the dispersion equation Eq. 73 in solid black, the analytical expression Eq. 78 in dotted blue and the simplified expression Eq. 79 in solid red color, respectively. The results from the very simple formula Eq. 79 match reasonably well for small metal film thickness with relatively large index contrast ratio. Thus, Eq. 79 could serve as a rough estimate at the beginning of the SCGD waveguide design.

It is worth noting that Fig. 22(b) that at a special case with zero gap thickness (i.e., typical D_{high}/Metal/D_{high} structure) the modal index is largest while the propagation distance is shortest. The propagation distance can be significantly enhanced in a SCGD structure by symmetrically inserting the low-index gap layers. Thus, an ultra-long range SPP mode can be supported in the SCGD structure. However, the rate of exponential decay within the cladding layer decreases.

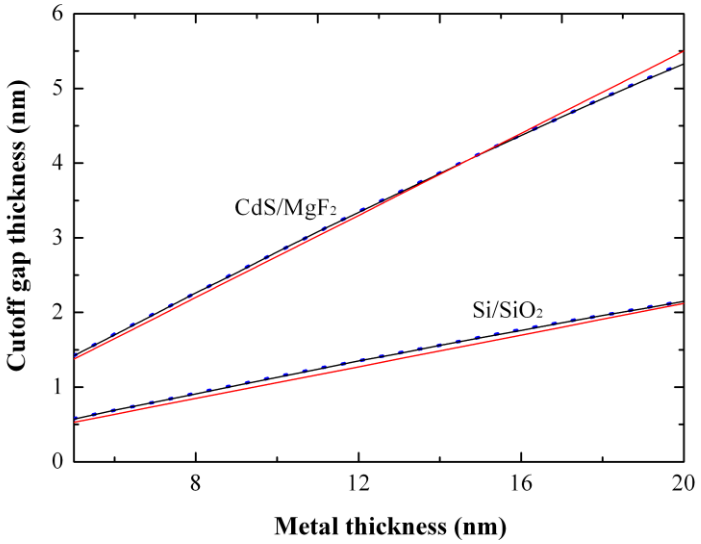

Fig. 27 Cutoff gap thickness versus metal thickness using three different approaches – dispersion equation Eq. 73 in solid black, analytical expression Eq. 78 in dotted blue and simplified expression Eq. 79 in solid red

4.1.2.3 The Energy Flux Density of SCGD Guided Mode

The propagating power of the SCGD guided mode can be plotted numerically by using the energy flux density

$$S_z = \frac{1}{2} Re\left(\vec{E} \times \vec{H}^*\right) \cdot \hat{z}, \tag{81}$$

where the fields are the transvers components E_x from Eq. 68 and H_y. Figure 28 shows the power flow of the propagating mode in the SCGD structure at different index contrast materials (Ge/Si) Fig. 28(a), (CdS/MgF$_2$) Fig. 28(b), and (Si/SiO$_2$) Fig. 28 (c)at fixed metal thickness d=20 nm, and different gap thicknesses. We can see how the energy flux density highly concentrated within the low index gap and decaying into cladding layers. It is worthy of note that strong modal confinement can be achieved within the nanometer- scale gap layers. This is because at the interfaces of the cladding/gap layer and the gap/metal layer, the normal component of displacement field D_x is continuous. As a result, a high index contrast ratio of the cladding layer to the gap layer leads to a great enhancement in the normal electric field E_x in the gap layer by a factor of $(n_\mathrm{d}/n_\mathrm{g})^2$ times. For example, using Si/SiO$_2$ for cladding/gap materials as shown in Fig. 28(c), the normal component of the electric field E_x has its largest amplitude within a few nanometres' SiO_2 gap while the electric field E_x in the cladding Si layer at the Si/SiO_2 boundary dramatically drops to $(n_g/n_d)^2 = 17.5\%$ of that in the SiO_2 gap. As the index contrast decreases, the concentrated field within the low-index gap decreases comparing to the rise in the field within the high-index claddings as seen in Fig. 28(a) and (b).

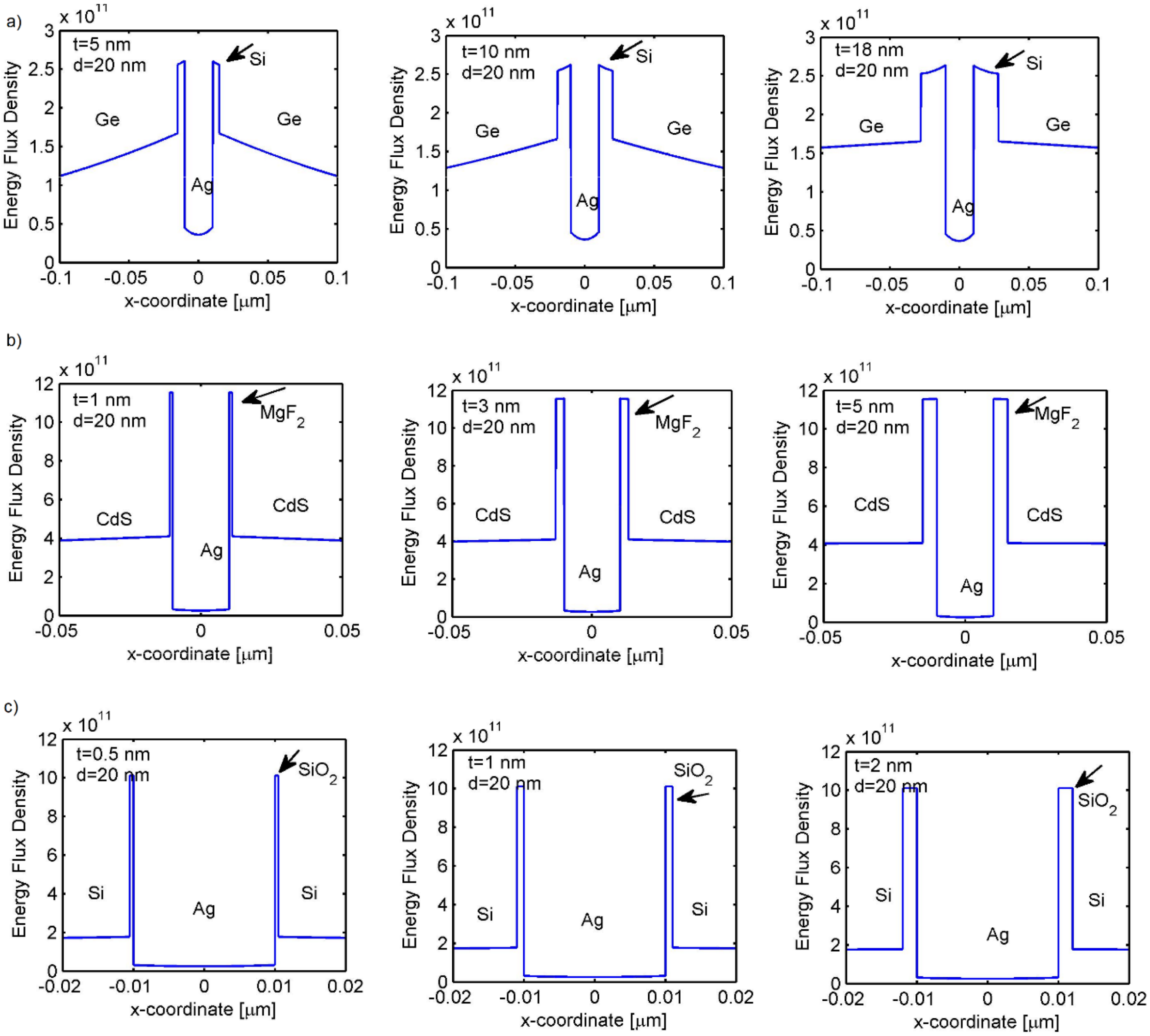

Fig. 28 The energy flux density of the SCGD guided mode for different index contrast materials at different gap thicknesses t at fixed metal thickness *d*=20 nm, a) Ge/Si (*t*=5, 10, 18 nm), b) CdS/MgF_2 (t=1, 3, 5 nm), and c) Si/SiO_2 (t=0.5, 1, 2 nm)

At low index contrast Ge/Si in Fig.28 (a), when the gap thickness increases from t=5 to 18 nm, it is noticeable how the fields in the claddings enhance. However, when index contrast increases, as well as the gap thicknesses, the field power decayed in the cladding layers is almost constant as shown in Fig. 28(b) & 28(c). This is because the cutoff gap thickness is very small as index contrast increases as show in Fig. 22; it is almost a few nanometers t_{max}~2.2 and 5.2 nm for Si/SiO_2 and CdS/MgF_2, respectively. Thus, the change in the field within the cladding can not be observed while the field highly confined within the low index gap.

4.1.3 Lateral Confinement

Confining the SCGD mode laterally is an important factor that needs to be considered when designing SCGD waveguides. Although a one-dimensional SCGD waveguide structure is primarily investigated here, the characteristics of the SCGD mode can be implemented in a two-dimensional SPP waveguide with proper geometrical design. This could be achieved by using the strategies in integrated optics for reducing a mode size in the lateral cross section by having a core index significantly larger than its surrounding index.

Figure 28(a) illustrates the proposed two-dimensional plasmonic waveguide structure for lateral confinement and the electric field distribution for the structure, and Fig. 28(b) shows the absolute value of the electric field $E(x,0)$ of the guided SCGD mode, which is obtained by using the commercial software package COMSOL Multiphysics. The core structure of the proposed scheme is exactly the same as the SCGD structure, with the width of the high-index Ge cladding layers limited to 500 nm, while the surrounding area is a typical DMD structure formed by a metal strip sandwiched by low-index SiO_2 layers. The metal film is 40 nm thick, and the thickness of the low-index SiO_2 layer is 10 nm, which is less than the cutoff gap thickness. From Fig. 28, we can clearly see that lateral confinement is achieved. This is attributed to the fact that the effective index for the SCGD mode at the core is larger than that for the SPP mode at the surrounding region with $D_{low}/M/D_{low}$ structure. One can also see that the maximum electric field intensity is well concentrated within the sub-wavelength low index gap, with thickness about 0.0065λ, and decays exponentially away into the cladding regions. It is worthy of note that the lateral confinement can also be achieved by continuously varying the low-index gap thickness, for example, by changing the geometry of the high index layer to cylindrical shape [12, 51], in which the guided SCGD mode is only supported in the region where the thickness of the gap is smaller than the cutoff gap thickness. Nevertheless, planar geometry is always preferable in order to be compatible with planar fabrication techniques such as silicon-on-insulator (SOI) and CMOS.

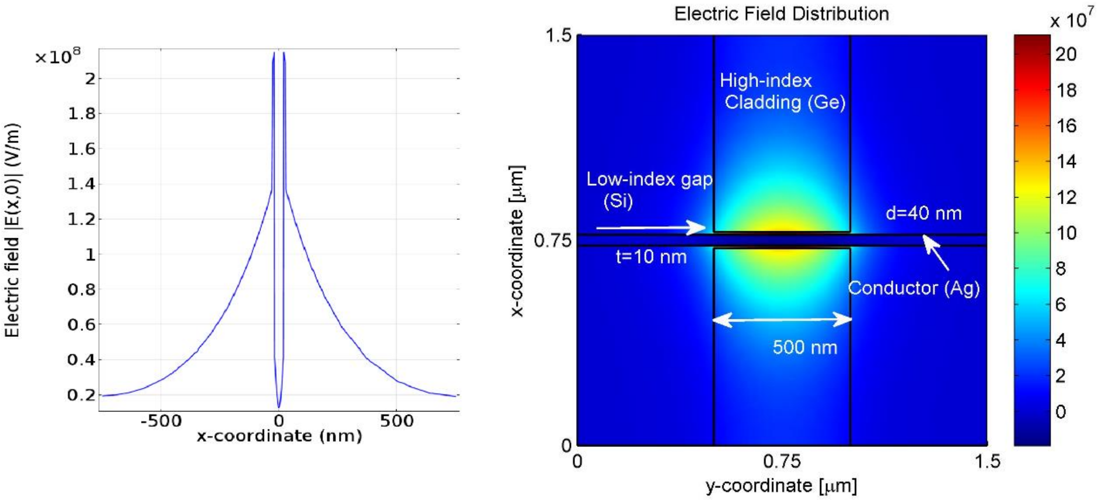

Fig. 29 Electric field distribution in the proposed two-dimensional SCGD waveguide for lateral confinement. (b) The electric field strength |E(*x*,0)| as a function of *x*.

4.1.4 Conclusion

We have theoretically analyzed the guided mode in a symmetric conductor gap dielectric (SCGD) plasmonic waveguide. The condition for the existence of the SCGD mode is that the low-index gap thickness must be smaller than a cutoff gap thickness. The dispersion equation and analytical expressions of the cutoff gap thickness are derived, from which the SCGD mode can be characterized numerically. The presence of the low-index gap layers between the metal strip and high-index cladding layers has fundamentally changed the modal behavior. The energy flux density of the SCGD guided modes are plotted numerically based on our analytical equation at various gap thicknesses for different index contrast materials. The propagation distance of the guided SCGD mode is considerably increased in comparison with that of the typical DMD mode. In the case of a large index-contrast ratio of the cladding/gap layers, the transverse electric field of the SCGD mode is tightly confined within the nanoscale gap layer while dropping sharply at the interface of the gap and high-index cladding layer. The lateral confinement of the SCGD mode is also discussed. The commercial mode solver is also used and gives similar results to the analytical one. The SCGD plasmonic waveguide has potential applications in surface-plasmon nano-lasers and plasmonic sensors. The theoretical analysis presented shall be useful for designing ultra-long range SCGD waveguides or symmetric hybrid plasmonic waveguides with superior field confinement.

4.2 Theoretical Study of Hybrid modes in a 7-layer Symmetrical Plasmonic Waveguide

In the previous section, we presented a theoretical analysis [77] for a planar 5-layer symmetrical conductor-gap-dielectric waveguide (SCGD), which consists of a thin metal layer centered between two low-index gaps of finite thicknesses *t*, symmetrically clad with infinite high-index cladding layers. To support hybrid plasmonic modes the low-index gap thickness has to be smaller than the cutoff gap thickness, which is only a few nanometers for a high contrast ratio of high to low index. Although the propagation length can be substantially increased near the cutoff gap thickness, it may not be practical to fabricate them. Fortunately, this problem associated with the 5-layer structure can be alleviated by a 7-layer plasmonic structure by replacing the infinite high-index cladding layers with a finite thickness and introducing infinite low-index layers to the bottom substrate and the top cover.

In this section, we presented an analytical model and an extensive analysis of the hybrid plasmonic modes in the 7-layer planar plasmonic structure. Such a waveguide structure has been discussed by Chen *et al*. [82], who employed the commercial software COMSOL to analyze the hybrid guided modes. Here we derived the dispersion relation of the hybrid guided modes. The results based on our analytical formulae agree well with those obtained by COMSOL in [82]. We show that the thicknesses of the low-index gap and the high-index layer play important roles in determining the types of the hybrid guided modes: strong SPP-like mode, SPP-Dielectric Waveguide (SPP-DW)-like mode and strong DW-like mode according to our defined criteria on the ratio of the peak energy flux density. To further characterize the performance of the plasmonic waveguide, the normalized mode size, the figure of merit and the confinement factor are investigated in detail. Our results reveal that with a small low-index gap, the strong-SPP-like mode is always present no matter how thick the high-index dielectric layer is. With a large low-index gap, the SPP-like mode occurs when the thickness of the high-index layer is smaller than a critical thickness h_c, and to achieve the best light confinement there is an optimum thickness of the high-index dielectric layer. To the best of our knowledge, this is the first comprehensive theoretical analysis for a planar 7-layer symmetrical plasmonic waveguide based on analytical expressions.

4.2.1 Theoretical Model

Figure 30 illustrates a one-dimensional 7-layer hybrid plasmonic waveguide schematically. It consists of a thin metal layer with thickness *d* and permittivity ε_m sandwiched between two low-index sub-wavelength gap with thickness *t* and permittivity ε_g, which are clad on both sides with high-index dielectric layer with permittivity ε_d and thickness h. The structure is clad with an infinite cover layer and an infinite substrate layer with dielectric permittivities ε_c and ε_s respectively. We assume that the dielectric materials are lossless. In addition, the geometry is assumed to be infinite in the *y*-direction so that the fields of the hybrid mode have no *y* dependence. The propagation direction of the hybrid mode is in the *z*-direction. The only polarization supported by such a structure is a transverse-magnetic (TM) mode so that the wave equation for the magnetic field intensity in each layer is

$$\frac{\partial^2 \vec{H}}{\partial x^2} + (k_0^2 \varepsilon_r - \beta^2)\vec{H} = 0, \tag{82}$$

where k_0 is the wave vector in the vacuum is, β is the propagation constant of the guided hybrid mode, and ε_r is the relative permittivity of each medium in the structure. The general solution of the wave equation is

$$\vec{H} = H_y(x) e^{i\beta z} \hat{y} \tag{83}$$

where the non-vanishing components of the fields are H_y, E_x, and E_z. The electric field components can be obtained using Maxwell's equations for time-harmonic fields:

$$\vec{E} = -\frac{1}{\omega \varepsilon_r}\left(\beta H_y \hat{x} + i\frac{\partial H_y}{\partial x}\hat{z}\right). \tag{84}$$

At the interior interfaces, the boundary conditions must be satisfied, i.e., the tangential components of the magnetic and electric fields as well as the normal component of the electric displacement field must be continuous. Applying the boundary conditions at the interior six interfaces, we derive the mode characteristic equation. The dispersion relation of the hybrid guided mode can be written as

$$e^{2k_m d} = \frac{\left[\frac{k_m}{\varepsilon_m} + \frac{(1-Q)k_g}{(1+Q)\varepsilon_g}\right]\left[\frac{k_m}{\varepsilon_m} + \frac{(1-R)k_g}{(1+R)\varepsilon_g}\right]}{\left[\frac{k_m}{\varepsilon_m} - \frac{(1-Q)k_g}{(1+Q)\varepsilon_g}\right]\left[\frac{k_m}{\varepsilon_m} - \frac{(1-R)k_g}{(1+R)\varepsilon_g}\right]} \tag{85}$$

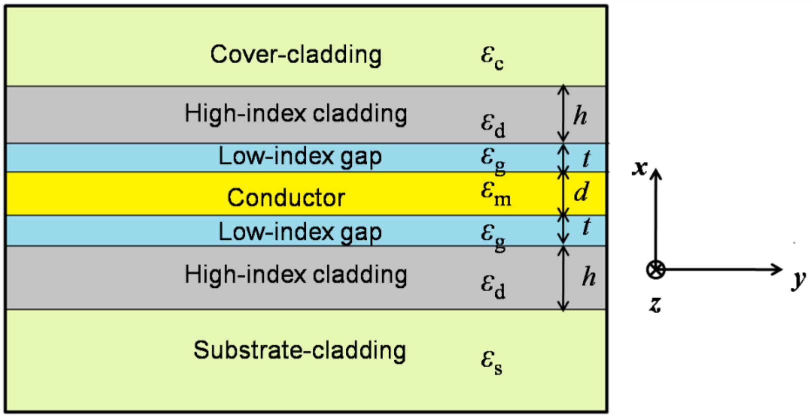

Fig. 30 Schematic configuration of the one-dimensional 7-layer hybrid plasmonic waveguide

where

$$Q = e^{2k_g t}\frac{\left[\frac{k_g}{\varepsilon_g} - \frac{(1-r)k_d}{(1+r)\varepsilon_d}\right]}{\left[\frac{k_g}{\varepsilon_g} + \frac{(1-r)k_d}{(1+r)\varepsilon_d}\right]}, \tag{86}$$

with

$$r = e^{2k_d h}\frac{\left(\frac{k_d}{\varepsilon_d} + \frac{k_s}{\varepsilon_s}\right)}{\left(\frac{k_d}{\varepsilon_d} - \frac{k_s}{\varepsilon_s}\right)} \tag{87}$$

and

$$R = e^{2k_g t}\frac{\left[\frac{k_g}{\varepsilon_g} - \frac{(1-q)k_d}{(1+q)\varepsilon_d}\right]}{\left[\frac{k_g}{\varepsilon_g} + \frac{(1-q)k_d}{(1+q)\varepsilon_d}\right]}, \tag{88}$$

with

$$q = e^{2k_d h}\frac{\left(\frac{k_d}{\varepsilon_d}+\frac{k_c}{\varepsilon_c}\right)}{\left(\frac{k_d}{\varepsilon_d}-\frac{k_c}{\varepsilon_c}\right)}. \tag{89}$$

k_c, k_d, k_g, k_m, and k_s are the wave vectors in the cover, high-index dielectric cladding, low-index gap, metal, and substrate materials, respectively, and can be written as:

$$k_i = \sqrt{\beta^2 - k_0^2\varepsilon_i}, \text{ where i=c, d, g, m, s.} \tag{90}$$

For the sake of symmetry, we assume that both the cover and the substrate are made up of the same low-index dielectric material with permittivity ε_c=ε_s. Hence, the dispersion relation Eq. 85 can be simplified:

$$e^{k_m d} = \pm\frac{\left[\frac{k_m}{\varepsilon_m}+\frac{(1-Q)k_g}{(1+Q)\varepsilon_g}\right]}{\left[\frac{k_m}{\varepsilon_m}-\frac{(1-Q)k_g}{(1+Q)\varepsilon_g}\right]}. \tag{91}$$

This symmetric waveguide structure can support two kinds of hybrid guided modes – symmetrical and anti-symmetrical SPP modes, which are respectively represented by Eq. 91 with the positive and negative signs. The symmetrical and anti-symmetrical modes are often referred as the long-range SPP (LRSPP) and short-range SPP (SRLPP) modes. The dispersion relation can be expressed in a transcendental form. For the positive sign of the dispersion relation, the symmetrical LRSPP hybrid mode equation can be written as:

$$\tanh\left(\frac{k_m d}{2}\right) = \frac{(1-Q)k_g\varepsilon_m}{(1+Q)k_m\varepsilon_g} \tag{92}$$

and for the negative sign, we obtain the anti-symmetrical SRSPP hybrid mode equation:

$$\tanh\left(\frac{k_m d}{2}\right) = \frac{(1+Q)k_m\varepsilon_g}{(1-Q)k_g\varepsilon_m}. \tag{93}$$

Here we only discuss the symmetrical LRSPP hybrid mode because of its low propagation loss. By solving the characteristic guided mode equation Eq.92, we can obtain the optical properties of the

LRSPP hybrid mode such as the mode effective index ($n_{\text{eff}} = \text{Re}(\beta/k_0)$) and the propagation length. The propagation length L_{prop} is defined as the distance where the power of the propagating hybrid mode decays to 1/*e* of its initial value, which can be expressed in terms of the imaginary part of the modal index:

$$L_{prop} = \frac{\lambda}{4\pi Im(n_{eff})}. \tag{94}$$

Specifically, as the high-index layer's thickness h approaches infinity, we obtain from Eq. 92 the same mode characteristic equation we recently proposed for the 5-layer SCGD plasmonic waveguide structure [77]:

$$\tanh\left(\frac{k_m d}{2}\right) = \frac{k_g \varepsilon_m (1-r)}{k_m \varepsilon_g (1+r)}. \tag{95}$$

As studied in [77], there exists a cutoff gap thickness condition to support plasmonic modes in the SCGD system. The modal index of the SCGD plasmoinc mode which is localized in the low-index nanoscale gap layer is larger than the index of the outmost dielectric cladding layers. As the gap thickness increases the modal index will decrease until it is equal to the index of the dielectric cladding at the gap cutoff thickness, resulting in a leakage mode into the high-index layer.

On the other hand, in the 7-layer plasmonic waveguide the presence of the low-index cover and substrate layers will substantially change the modal index behavior of the LRSPP hybrid guided mode. The 7-layer plasmonic structure can be regarded as a modified DMD structure where the dielectric layer is replaced with three conventional low/high/low (LHL) dielectric waveguide layers, i.e., low-index-gap/high-index-cladding/low-index-cover (or substrate). The hybrid mode originates from the mode coupling between the SPP mode and the conventional DW mode due to the dielectric LHL layers. When the thickness of the inner low-index gap is very small compared with that of the high-index cladding layer, the cover and substrate have little impact on the guided mode; thus the 7-layer waveguide behaviors like a 5-layer waveguide structure [77] supporting the plasmonic guided modes. With increasing the inner low-index gap layer thickness, the supporting guided mode gradually transits from a plasmonic-like to a hybrid plasmonic-dielectric-like mode attributable to the mode coupling of the dielectric mode from the LHL layers. When the gap layer thickness is further increased, the conventional dielectric mode becomes predominant. Therefore, as the gap thickness increases, the modal index will decrease without any cutoff. Consequently, we will always have the hybrid guided mode as the gap thickness increases; however, this will affect the mode confinement. In the next section, we will first investigate the characteristic parameters (i.e., modal index and propagation length) of the guided hybrid mode. Then we will characterize the hybrid guided mode and elaborate its evolution from the plasmonic-like mode to the dielectric-like mode along with the performance of the waveguide structure.

4.2.2 Numerical Analysis and Discussion

4.2.2.1 The Modal Properties

In this study, the high-index cladding material is chosen to be silicon with refractive index n_{Si}=3.455 whereas the low-index gap is silica with refractive index n_{SiO2}=1.445. The high index contrast ratio (defined as the ratio of high-index n_{Si} to low-index n_{SiO2}) enables significant enhancement of the field in the nano-scale low-index gap. Both the low-index cover and the substrate materials are also chosen to be silica because it is compatible with current fabrication techniques, such as the silicon-on-insulator fabrication method. The waveguide model is assumed to be operated at the telecom wavelength λ =1550 nm. Silver and gold are employed to be the conductor materials with a permittivity of ε_{Ag}=-129+3.3j and ε_{Au}=-115.11+11.103j, respectively. To analyze the optical properties of the LRSPP hybrid guided mode and how the geometrical dimensions affect the hybrid guided modal index and the propagation length L_{prop}, the characteristic mode equation Eq. 92 has been solved numerically.

Figure 31, 32, and 33 show the behavior of the modal index and the propagation length versus the gap thickness t from 0 to 100 nm at fixed dielectric cladding thicknesses h = 100, 200, 300, 400, and 500 nm, and fixed metal (silver) film thicknesses d = 20, 40, and 60 nm, respectively, for the 7-layer waveguide structure, which is compared with the 5-layer SCGD waveguide [77]. As expected, with increasing the gap thickness t, the modal index decreases while the propagation length increases; moreover, there is no cutoff gap thickness for the 7-layer waveguide structure. Although the presence of the low-index top and bottom layers has brought the modal index down slightly, the modal index of the guided mode is always larger than that of the outmost layers, which consequently eliminates the gap cutoff thickness condition of the hybrid mode. Thus, the hybrid mode will always present, which can greatly enhance the fabrication tolerance of the gap region thickness t. In contrast, for SCGD waveguide structure, the cutoff gap thickness *t* is only a few nanometers. As shown in Fig. 31, Fig. 32, and Fig. 33, the cutoff gap thicknesses are respectively about 2.2, 3.8, and 4.2 nm for the metal thickness of 20, 40, and 60 nm, respectively.

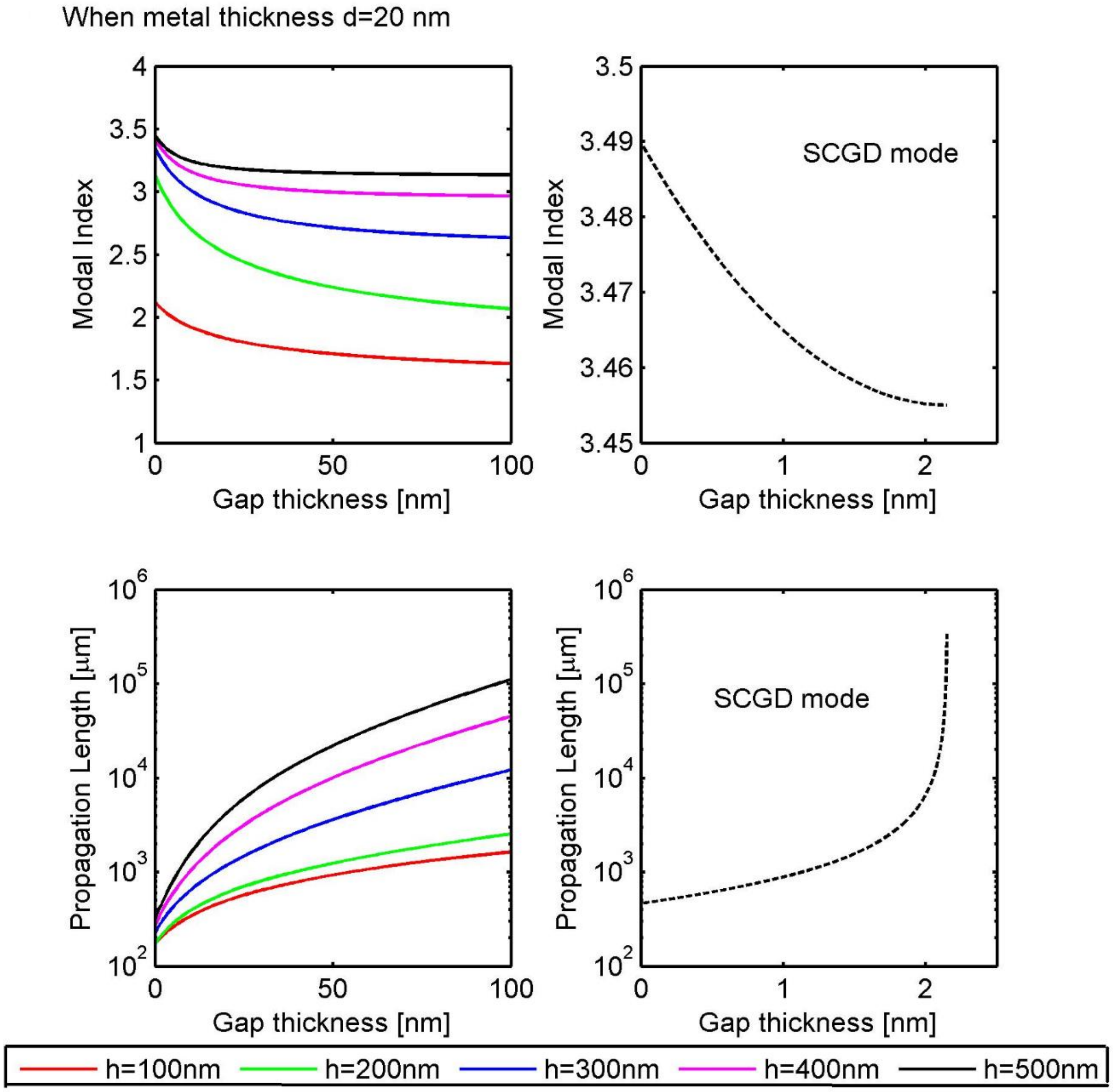

Fig. 31 Modal index and propagation length of the 7-layers HPW structure at different dielectric thicknesses *h* = 100, 200, 300, 400, and 500 nm and our recent SCGD waveguide (dashed black) versus the gap thickness *t*, at metal thickness *d* = 20 nm

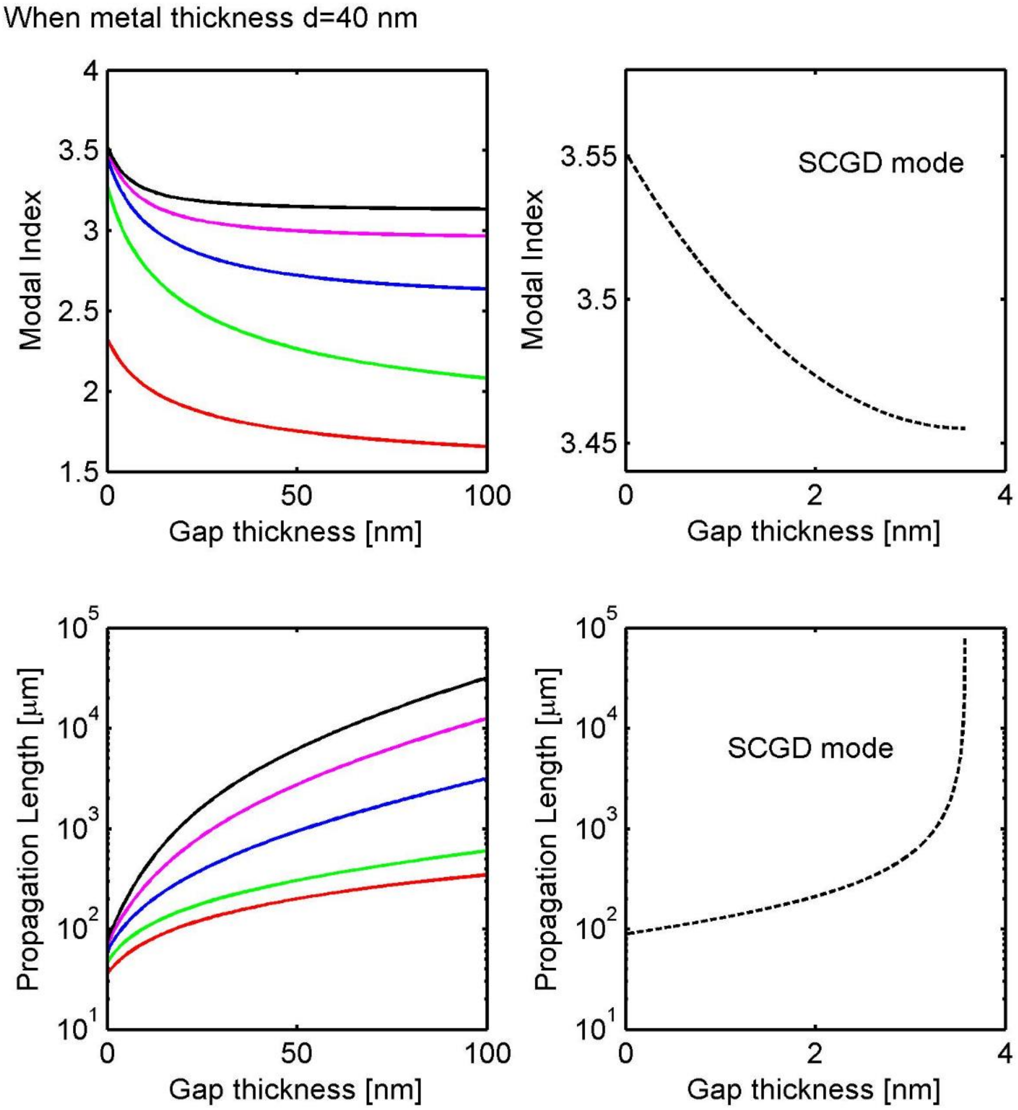

Fig. 32 Modal index and propagation length of the 7-layers HPW structure at different dielectric thicknesses *h* = 100, 200, 300, 400, and 500 nm and our recent SCGD waveguide (dashed black) versus the gap thickness *t*, at metal thickness *d*=40 nm

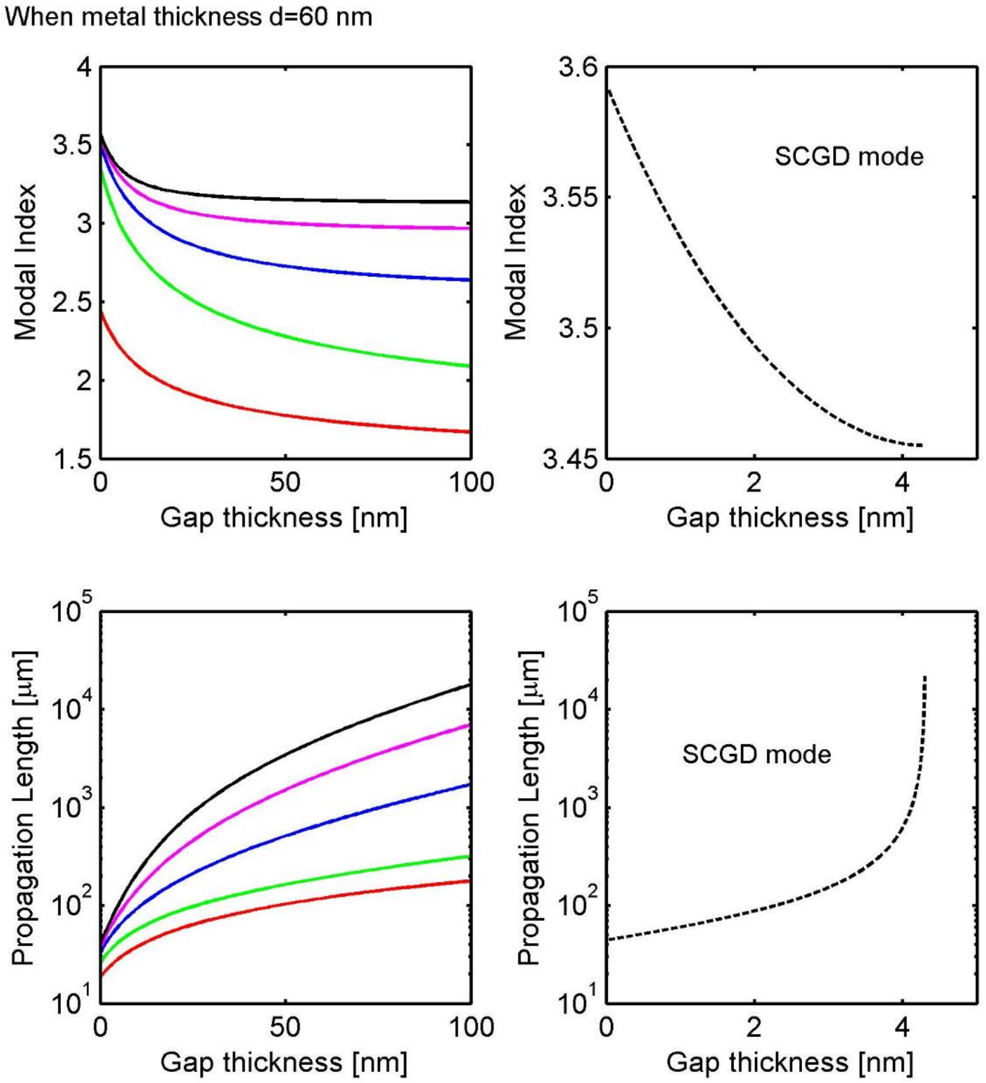

Fig. 33 Modal index and propagation length of the 7-layers HPW structure at different dielectric thicknesses *h* = 100, 200, 300, 400, and 500 nm and our recent SCGD waveguide (dashed black) versus the gap thickness *t*, both at the metal thickness *d*=60 nm

Note that from Fig. 31, at small gap thickness t of a few nanometers with a large high-index dielectric layer (such as h = 500 nm), the modal index of the hybrid guided mode for the 7-layer waveguide is very similar to that for the 5-layer SCGD waveguide. For example, at the metal thickness d = 20 nm, the modal index at zero gap thickness is about 3.49 for both the SCGD waveguide and the

7-layer waveguide with *h*=500 nm. This is because for very small *t* and large *h*, the effect of the cover and substrate is negligible, reducing to the case of the SCDG waveguide. Moreover, the propagation length increases as the dielectric thickness *h* as well as the gap thickness; this will certainly affect the degree of the mode confinement of the hybrid mode, as will be discussed later. Figure 32 and Fig. 33 also show that increasing the metal film thickness will results in a slight increase of modal index of the hybrid mode and a decrease of the propagation length due to the Ohmic loss in the metal.

In Fig. 34 we investigate the dependence of the modal index and the propagation length on the dielectric cladding thickness *h* at different values of the gap thickness *t* in order to compare our results based on the analytical dispersion equation Eq. 92 with those obtained by Chen *et al*. [82] using the commercial software COMSOL. Their results based on the COMSOL perfetctly agree well with our results based on the anayltical results of Fig. 34. Gold was used as the metal thin film in [82] while both gold (dashed line) and silver (solid line) are used in our work, with the metal thickness *d* fixed at 20 nm. Figure 34(a) shows that the modal indices for both metals are almost identical while the distinct improvement on the propagatuion length with silver is clearly demostrated in Fig. 34(b) due to its smaller ohmic loss. The modal index and propgation length of the conventional DMD plasmonic waveguide are calculated and shown as the horizontal dashed lines, where the dielectrics are assumed to be silicon and silica. For a fixed gap thickness, the modal index increases with the thickness of the high-index layer. The modal indices of the hybrid guided mode fall between those of the plasmonic modes for the conventional DMD (SiO_2/Ag/SiO_2) and that of the hybrid guided mode (Si/Ag/Si) waveguides. It is quite apparent how the propagation is greatly improved compared with the conventional Si/Ag/Si plasmonic waveguide. Although the propagation length of the SiO_2/Ag/SiO_2 plasmonic waveguide is large, the mode confinement of the structure is very weak, compared with that of the proposed 7-layer symmetrical waveguide.

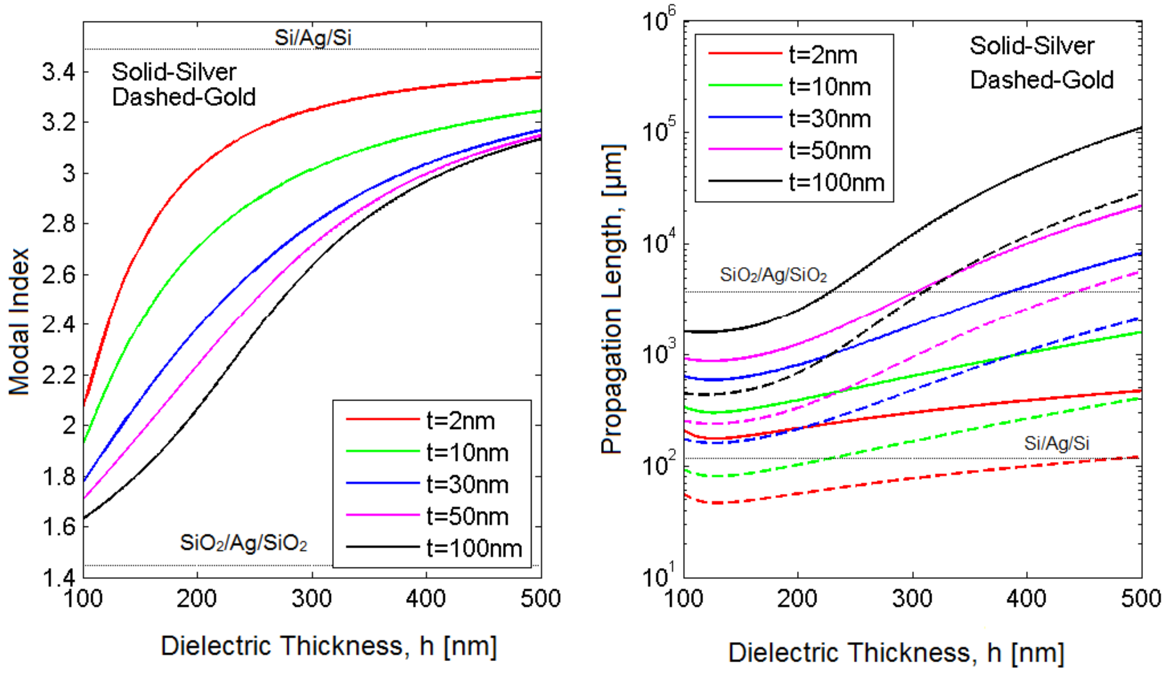

Fig. 34 Modal index and propagation length of the LRSPP hybrid mode versus the dielectric thickness *h* for silver (solid line) and gold (dashed line) at fixed gap thickness *t* = 2, 10, 30, 50, and 100 nm

4.2.2.2 The Energy Flux Density

The variation of the modal index and the propagation length with geometric dimensions in Fig. 34 suggests the evolution of the hybrid guided mode. Figure 35 illustrates the energy flux density of the hybrid mode along the *x*-direction at different gap and dielcrtic cladding thicknesses, using the time-averaged value of the *z*-component of the poynting vector:

$$S_z = \frac{1}{2} Re\left(\vec{E} \times \vec{H}^*\right) \cdot \hat{z}, \tag{96}$$

where E_x and H_y are the transverse components of the field solutions obtained from Eq. 83 and Eq. 84. Note that the metal (silver) thickness is set to be 20 nm for the rest of this study. Figure 35(a) shows the power of the hybrid mode is strongly confined within the 10 nm gap when the dielectric cladding thickness *h* is 100 nm based on the derived analytical equations. With the gap and dielectric cladding thickness increase, the power is gradually shifted from the low-index gap toward the high-index dielectric cladding, as shown as shown in Fig. 35(b). Further increases of the gap and cladding thickness lead to complete power transfer to the high-index dielectric regime (see Fig. 35(c)) to form a hybrid DW-like mode. Apparently, the geometrical parameters of the plasmonic waveguide have great influence on the formation of the hybrid guided mode.

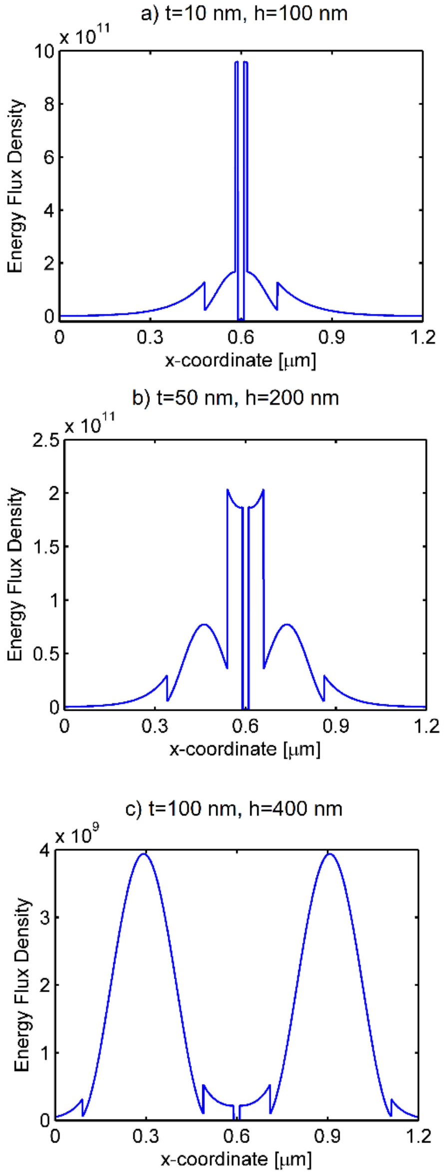

Fig. 35 Energy flux density of the hybrid mode along x-direction at different dielectric and gap thicknesses a) [*h*, *t*] = [100nm, 10nm], b) [200nm, 50nm], c) [400nm, 100 nm].

4.2.3 Hybrid Guided Mode Evolution

The hybrid mode characteristic has been investigated by Chen *et al*. [82] using the mode character $|a_{+}(h,t)|^2$ originally employed by Oulton *et al*. [12] to study the degree of the hybrid mode and determine whether it is SPP-like or cylindrical-like using a criterion $|a_{+}(h,t)|^2 = 0.5$. The mode character depends on the index difference ratio [12]:

$$|a_{+}(h,t)|^2 = \frac{n_{hyb}(h,t)-n_g}{[n_{hyb}(h,t)-n_d(h)]+[n_{hyb}(h,t)-n_g]}, \tag{97}$$

where n_{hyb} is the effective mode index of the hybrid mode, n_{d} is that of the conventional dielectric cylindrical waveguide and n_{g} is the refractive index of the gap material. Although Chen *et al*. obtained the mode character as a function of the dielectric cladding thickness for different gap thickness and pointed out at smaller/larger dielectric thickness the hybrid mode tends to be SPP/dielectric-like, there was a lack of quantitative information on the dielectric cladding thickness at which the hybrid mode is SPP-like or dielectric-like. This is because the criterion in Oulton's work [12] for non-symmetrical cylinder shape is not applicable for the symmetrical planar shape.

To analyze in detail whether the hybrid mode is a hybrid plasmonic mode or a hybrid dielectric mode, we calculate the maximum energy flux density (i.e., Poynting vector) in two regimes – $P_{\mathrm{max,g}}$ in the low-index gap and $P_{\mathrm{max,d}}$ in the high-index dielectric cladding, where the mode is mainly localized. The ratio of peak energy flux density $P_{\mathrm{max,g}}/P_{\mathrm{max,d}}$ is employed to characterize the hybrid mode. Two criteria are used. The first criterion is $P_{\mathrm{max,g}}/P_{\mathrm{max,d}} = 1$, i.e., equal maximum energy flux density at the two regimes and the second is when the maximum energy density in the high-index region decreases to 1/e of that in the low-index gap region, i.e., $P_{\mathrm{max,d}}/P_{\mathrm{max,g}} = 1/e$. Fig. 36(a) shows the ratio of the peak energy flux density as a function of the high-index cladding thickness h for different low-index gap thickness t. The horizontal blue and black lines represent the two criteria used to characterize the guided hybrid mode.

At the larger gap thickness t = 30, 50,100 nm, the peak ratio of the energy flux density in the gap region decreases with the increase of the dielectric thickness h. At the largest gap thickness t = 100nm, for example, the first criterion is satisfied at $h \approx$ 170nm while the second is at $h \approx$230nm. That means when the dielectric cladding thickness h is greater than 230 nm, the hybrid mode will behave as conventional DW-like mode since the peak energy flux density in the cladding area is higher than that in the gap; the energy flux density distribution at t = 100 and h = 400 nm shown in the lowest plot of Fig. 36(b) is an example of a strong DW-like mode. The hybrid mode shows strong SPP-like behavior at h < 170 nm as the peak energy flux density in the high-index cladding area is decreased by 1/e of that in the gap; the energy flux density distribution for a strong plasmonic mode is displayed in the top plot of Fig. 36(b) with t = 100 and h =100 nm. In the middle range of h = 170~230 nm, due to the strong coupling between the SPP and DW mode, the hybrid mode can be referred to as a SPP-DW-like mode. The energy flux density of this type of the hybrid mode is shown in the middle plot of Fig. 36(b) with fixed t = 100 and h = 200nm.

On the other hand, at small low-index gap thickness t =2 and 10 nm, Fig. 36(a) reveals that the peak energy flux density in the gap is always much larger than that in the high-index cladding region. For example, at t =2nm, the peak energy flux density in the gap is about 5.7 times of that in the high-index region over the whole range of h, indicating a strong SPP-like mode. This intuitively explains how the SPP plasmonic mode can be always formed with a nanoscale low-index gap(~10 nm) no matter how large the thickness of the high-index region is.

With gradually increasing the gap thickness, the thickness of the high-index layer h has to be controlled in order to have a strong plasmonic mode; the larger the low-index gap thickness, the smaller the allowed maximum thickness of the high-index layer. From Fig. 36 we can clearly see the significant impact of the thickness of the gap t and the cladding h on the degree of the hybrid guided mode.

In addition, the FEM mode solver is used to examine the hybrid guided modes types supported by the 7-layers hybrid plasmonic waveguide. Figure 37 shows the propagating power of the hybrid guided mode in z-direction for the waveguide in one and two dimensions at 1550 nm. The material for the low-index gap and the cover claddings is chosen to be silica, whereas for the high-index dielectric layer is silicon, at metal film thickness d=20 nm. Based on our mode characteristics criteria, such a waveguide structure supports three different types of hybrid mode. The first hybrid mode type is the strong SPP-like mode where the field is highly confined within the low-index subwavelength layer. This type of hybrid mode is shown in Fig. 37(a) at a miniscule low-index gap thickness t=10 nm and dielectric thickness h=100 nm. It can be clearly seen how the power confined and propagating in the low-index gap region is almost three times the power distributed within the cladding layers; this type of hybrid guided mode retains the character of plasmonic waveguides for subwavelength strong mode confinement. Figure 37(b) illustrates the propagating power profile for the second type of the guided modes in the 7-layer hybrid plasmonic waveguide: the SPP-DW-like mode. This kind of hybrid mode integrates the strength of the optical behavior of the SPP-like mode and DW-like mode. At *t*=50 nm ad *h*=200 nm, the SPP-DW-like mode is confined mostly within the low-index gap and the high-index dielectric layers as seen in Fig. 37(b). The third type of the hybrid guided mode is the DW-like mode, which gains the low loss character of the conventional DWs. Figure 37(c) shows this DW-like hybrid mode at the gap and dielectric thicknesses: *t*=100 nm and *h*=400 nm, respectively. We can observe how the power mostly localized within the high-index cladding layers. The propagating power in the dielectric layers is almost five times the power distributed within the other regions of the waveguide structure.

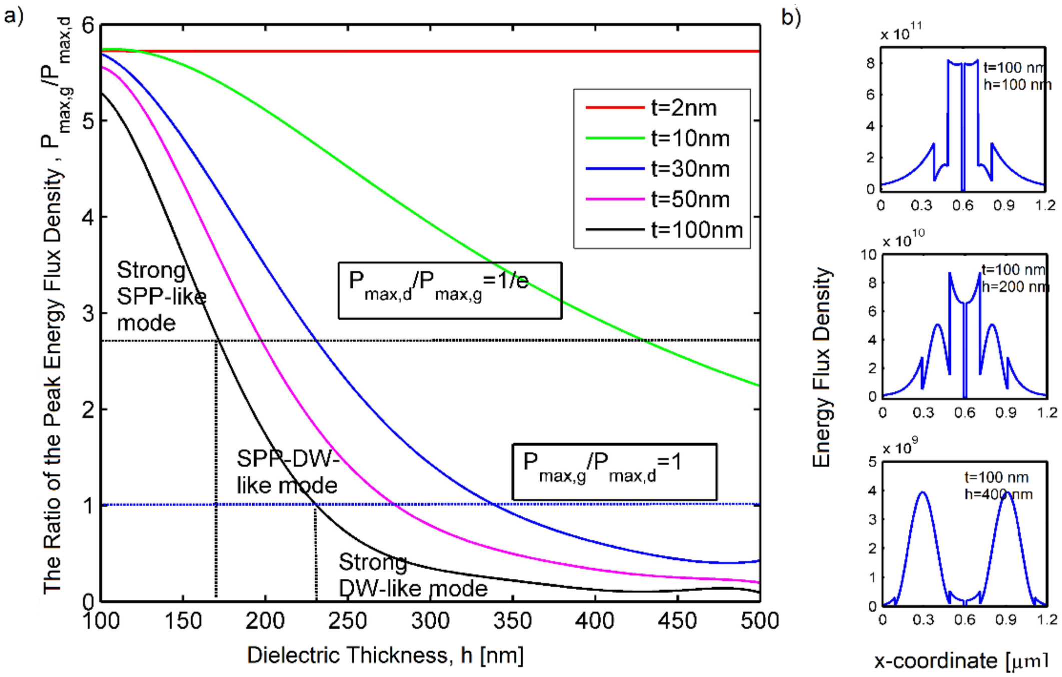

Fig.36(a) Dependence of the ratio of the peak energy flux density in the low-index gap to the high-index dielectric region on the dielectric thickness *h* at different gap thicknesses, (b) an example of the power profile at fixed *t* = 100 nm and different *h* = 100,200, and 400 nm

a) t=10 nm, h=100 nm

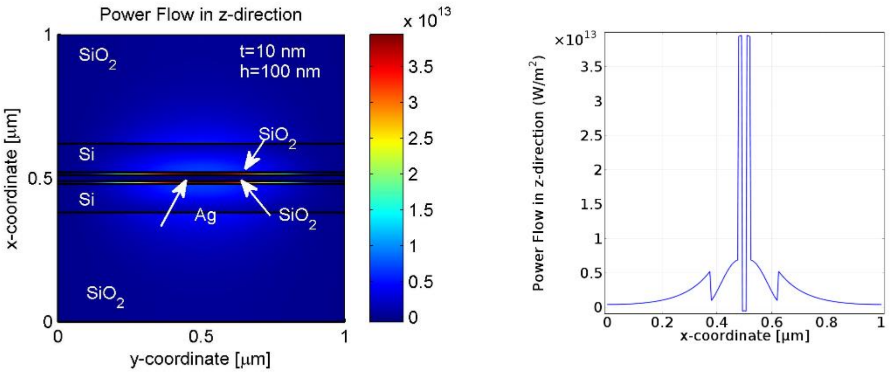

b) t=50 nm, h=200 nm

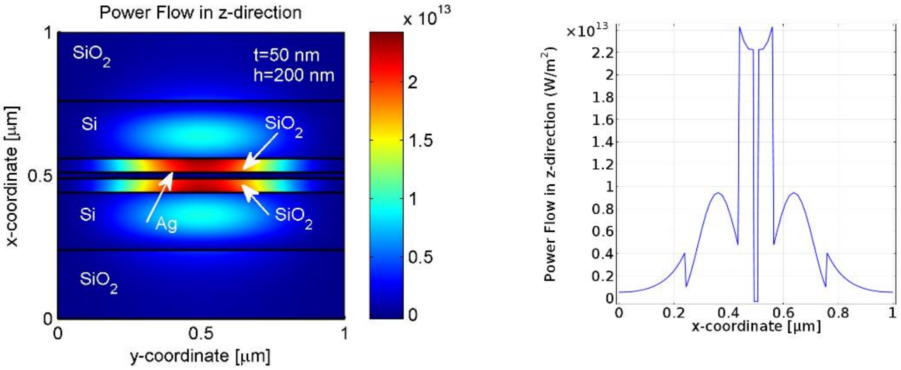

c) t=100 nm, h=400 nm

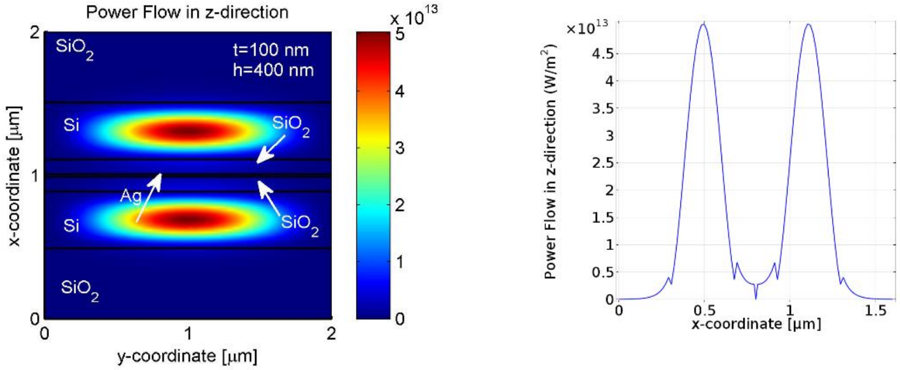

Fig. 37 The 1D and 2D plot of the power flow in z-direction for the three types of the hybrid guided mode at different dielectric and gap thicknesses, a) *t*=10 and *h*=100 nm, b) *t*=50 and *h*=200 nm, and c) *t*=100 and *h*=400 nm

4.2.4 Figures of Merit

For PWs, it is always desirable to have both tight mode confinement and long propagation length; however, in general, tight mode confinement comes at the price of the propagation length. FOM proposed by Berini [83] is a commonly adopted parameter to characterize the performance of PWs in terms of these two factors and defined as:

$$FOM = \frac{L_{prop}}{L_{ms}} \tag{98}$$

where L_{prop} is the propagation length and L_{ms} is the effective mode size. In a three-layer waveguide structure, the effective mode size L_{ms} is the 1/e field penetration depth, while for hybrid waveguide structure, it is defined as the ratio of the averaged value of the total mode energy flux to the peak energy flux density along the *x*-direction, which can be written as [82], [84]:

$$L_{ms} = \frac{\int_{-\infty}^{+\infty} S_z dx}{\max(S_z)}. \tag{99}$$

Fig. 38(a) and (b) show the normalized mode size L_{norm} (defined as L_{ms}/L_0 with $L_0 = \lambda/2$) and the FOM as a function of dielectric thickness h at different gap thickness, which are calculated from Eq. 98 &99 based on our analytical expressions.

It is interesting to observe in Fig. 38(a) that when the high index dielectric thickness h is around 130 nm there is a minimum normalized mode size for each gap thickness, which suggests that strong mode confinement can be achieved with suitably choosing h. When further increasing h, for a small gap thickness (such as t=2 and 10 nm), the normalized mode size increases monotonously as h increases. However, for a large gap thickness the normalized mode size increases until a critical dielectric thickness h_c, which are respectively about 230, 290, 340 nm for t = 100,50 and 30nm.Further increasing h, the mode size slowly increases with nearly the same value for different gap thickness. The physical reason can be explained easily based on the criteria we defined earlier for the characterization of the hybrid mode. Referring back to Fig. 36(a), we can see the critical dielectric thickness h_c is just the value where the maximum energy flux density in the gap and the dielectric regions is the same, i.e., $P_{max,g} = P_{max,d}$. That means when increasing the dielectric thickness from h_c, most of the energy of the hybrid mode starts to shift to the dielectric region forming DW-like hybrid mode. As a result, the PW supports dielectric-like mode when the dielectric thickness $h > h_c$, and SPP-like hybrid mode when $h<h_c$.

On the other hand, at small gap thickness t =2 and10 nm, the mode size smoothly increases as h increases in the absence of h_c indicating the existence of the SPP mode only for these cases. Therefore, the outcomes based on the normalized mode size are in good agreement with the results we obtained from Fig. 36(a) on the evolution of the guided hybrid mode.

Fig. 38(b) shows the FOM of the 7-layer waveguide structure. At large gap thicknesses t = 30 , 50, and100 nm, the FOM gradually increases with the increase of the dielectric thickness h at the beginning and then suddenly starts increasing rapidly beyond the critical dielectric thickness h_c. This is attributed to the fact that when h> h_c the guided hybrid mode starts to behave like a DW-like hybrid mode (as explained in Figs.36(a) and 38(a), which has much larger propagation lengths compared with a SPP mode, resulting in a noticeable enhancement in the FOM's value. At small gap thicknesses t =2and 10 nm, the FOM is almost the same over a wide range of the dielectric thickness without the presence of the critical dielectric thickness h_c, which suggests that the hybrid guided mode will be strong SPP-like mode at small gap thickness as discussed in Figs. 36(a) and 38(a), and there is a tradeoff between the mode confinement and the propagation length.

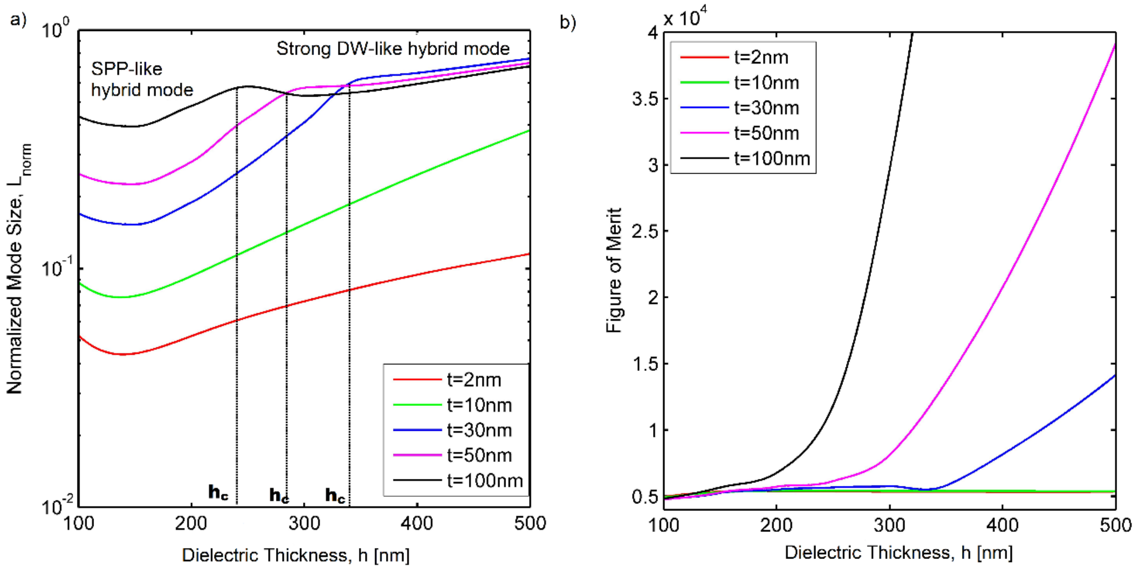

Fig. 38 (a) Dependence of the normalized mode size L_{norm}, and (b) the FOM on the high-index cladding thickness h at different gap thicknesses t = 2, 10, 30, 50, and 100nm.

4.2.5 Confinement Factor

Although the normalized mode size can be used to evaluate the performance of the mode confinement, it lacks information on how much energy is sustained within the nanoscale low-index gap. For practical applications in active plasmonic devices, strong interaction between the SPP and the active nano-gap layer is highly desirable. So, it is very important to know the portion of the mode power resided within the low- index gap to the total power of the whole waveguide, which is known as the confinement factor Γ [85].It is widely used to evaluate the light confinement in a specific regime of a waveguide, which is given by:

$$\Gamma = \frac{\frac{1}{2}\int_{gap} Re\left(\vec{E}\times\vec{H}^{*}\right)\cdot\hat{z}\,dx}{\frac{1}{2}\int_{total} Re\left(\vec{E}\times\vec{H}^{*}\right)\cdot\hat{z}\,dx}. \tag{100}$$

Figure 39 shows the influence of the gap thickness *t* and the dielectric thickness *h* on the confinement factor, which is calculated with our analytical expressions. It is very interesting to see that there is a maximum value of the confinement factor for each gap thickness *t* when the dielectric cladding thickness *h* is set to be about 130 nm, which coincides with the thickness for having a smallest normalized mode size, as seen in Fig. 38(a), and where strong localized SPP-like mode is assured to be supported according to the results in Fig. 36. At the optimum value of *h*, the portion of the mode energy sustained inside the low-index gap can be enhanced by increasing the gap thickness. For example, at *h* = 130 nm, about 35% of the mode energy will be confined within the sub-wavelength gap region at *t* = 10 nm while it can reach 50% when *t* is increased to 30 nm. Nevertheless, referring back to Fig. 38(a), there is a compromise between the confinement factor and the normalized mode size. On the other hand, when the high-index cladding thickness *h* is greater than 200 nm, the confinement factor is largely reduced and the larger the gap thickness *t*, the faster the rate of decline. This is because for a larger gap thickness, with increasing the high-index cladding thickness *h*, the hybrid mode is gradually evolved from strong a SPP-DW-like mode to a strong DW-like mode, while for a smaller gap thickness (such as *t* =2nm), strong SPP like mode is always present, resulting in a slight change in the confinement factor with the increases of the cladding thickness. Apparently, we can see that the confinement factor and the normalized mode size are complementary to each other to elaborate the mode confinement of the hybrid guided mode.

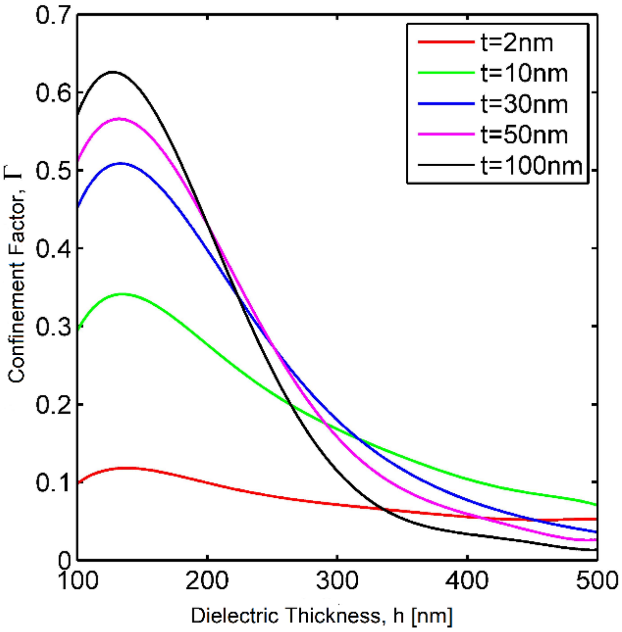

Fig. 39 Dependence of the confinement factor on the dielectric thickness h for different gap thickness t.

Hence, the7-layer PW structure can be optimized with strong mode confinement in the low-index gap by suitably choosing the thickness of the high-index cladding layer, which shall be very helpful to PW designers. Based on our results, we can conclude that the 7-layer symmetrical HPW can support strong SPP-like hybrid modes when the dielectric thickness *h* is less than approximately 200 nm at the large gap thicknesses *t* = 30, 50, and100 nm, whereas it can always support strong SPP mode at small gap thicknesses such as *t*=2 and 10 nm. In addition to the advantage of tight nanoscale mode confinement, when the dielectric thickness *h* is less than about 200 nm, the symmetrical 7-layer PW can provide a large propagation length (200–3000 μm), which is much larger than that (40–150 μm)in the hybrid cylindrical plasmonic structure [12]. Moreover, the planar waveguide geometry allows for easy fabrications.

4.2.6 Conclusion

A theoretical study of a 7-layer planar PW has been presented. The 7-layer waveguide consists of a thin metal layer symmetrically sandwiched with 3 low/high/low layers. We derived the dispersion equation for the hybrid mode which allows us to numerically calculate the mode index and the propagation length of the guided mode. Unlike the 5-layer symmetrical HPW we studied earlier [77] there is no cutoff condition for the low index gap thickness due to the two additional low-index outmost layers. Our results from the analytical expressions agree with those [82] obtained from the commercial software package. Based on our two proposed criteria, the evolution of the hybrid guided mode is investigated in detail, which can be strong SPP-like, SPP-DW-like, or strong DW-like, depending on the thickness of the inner gap and high-index cladding layers. The performance of the 7-layer PW is also examined, including the normalized mode size, the FOM and the confinement factor. The specific variations in the curves of the normalized mode size and the FOM with geometric dimensions of the waveguide indicate the transition of the hybrid mode. Our results from both the normalized mode size and the confinement factor show that strong mode confinement within the low-index gap can be obtained by properly choosing the high-index cladding thickness. The large propagation length along with tight mode confinement in nanoscale gap makes the 7-layer symmetrical planar PW suitable for applications in active and passive nanoplamonic devices.

Chapter 5

Hybrid Multilayerd Metal-Dielectric-Metal Plasmonic Waveguides

Gaining a comprehensive understanding of optical behavior of the guided mode in hybrid plasmonic waveguides (HPWs) requires theoretical-analytical equations to study and analyze all the contributors that may improve the optical performance of the waveguide, which can really help the waveguide designers to fabricate PWs. We thoroughly investigated the guided hybrid mode in planar five- and seven-layer hybrid DMD waveguide structures with thin metal layer at the center cladded symmetrically with low/high and low/high/low layer, respectively [77-78]; based on the derived mode questions, our numerical results explained the formation of the hybrid guided mode, the existence of the cutoff thickness [77], and the importance of the presence of the cover layers on the hybrid mode formation and characteristics [78].

In contrast to the hybrid DMD waveguides mentioned above with dielectrics as the outer layers, PW structures with metal layers as the outer layers, such as metal-dielectric-metal (MDM) structure have attracted considerable interest due to their extremely strong mode confinement, which is an important feature for all-optical data-processing devices. However, the three-layer MDM waveguide suffers from high loss. To overcome the drawbacks of the three-layer PWs, a modified MDM structure – five-layer symmetrical metal/low-index/high-index/low-index/metal has been proposed. Such a plasmonic waveguide structure has been presented by several groups. Kim [86] proposed complementary metal-oxide-semiconductor (CMOS) hybrid MDM plasmonic waveguide for subwavelength light confinement with enhanced propagation distance and studied by utilizing the commercial software (FIMMWAVE). Bian et *al*. [87] investigated the optical performance of a five-layer hybrid MDM waveguide which shows a significant improvement in crosstalk between adjacent waveguides by using commercial software (COMSOL).

In this thesis, we theoretically investigate the hybrid guided modes in a five-layer symmetrical hybrid-metal-dielectric-metal (MDM) plasmonic waveguide [88]. The hybrid guided mode is characterized and analyzed based on the results obtained from our derived analytical mode characteristics equations. Such a waveguiding structure can support different types of hybrid-MDM modes at different dielectric thicknesses. Consequently, the optical performance of the hybrid MDM plasmonic waveguide can be controlled by the geometrical parameters and the refractive indices of the dielectric layers. The proposed waveguide structures could be very useful in building on-chip all-optical devices and the analytical models could be potentially help the waveguide designer in designing and optimizing the plasmonic devices for ultra-compact nanophotonics [89].

5.1 Theoretical Study of the Hybrid Modes in a 5-layer MDM Waveguide

A comprehensive theoretical study of the guided hybrid mode in a five-layer (metal/low/high/low/metal) MDM plasmonic waveguide structure based on our derived hybrid mode dispersion equations will be presented. Our numerical results are in perfect agreement with those obtained from commercial software [87]. Our results reveal that the total thickness of the dielectric (low/high/low) layers as well as the thickness of each dielectric layer have significant impact on the formation of the hybrid modes and their optical performances. When the thickness of 3-layer dielectric is small, the guided hybrid mode tends to be the SPP-like mode; consequently the optical performance of the hybrid MDM structure falls in the regime of traditional MDM waveguide. For a large total dielectric thickness, the propagation length can be significantly improved by suitably choosing the thickness of the center high-index layer, which indicates the hybrid guided mode has becomes to dielectric waveguide-like mode as more power has been transferred to the high-index layer from the low-index dielectric layers. We also characterize the mode confinement in terms of the mode confinement factor and the normalized mode size. We found that the evolution of the hybrid mode with the change of the dielectric thickness is correlated with the changes of the mode size, the propagation length as well as the modal index. The effect of the refractive indices of the dielectric layers on optical performance is also discussed.

5.1.1 Basic Equations

Figure 40 illustrates a schematic diagram of the 1D hybrid-MDM multilayer plasmonic waveguide structure. A high-index dielectric layer with thickness *d* and permittivity ε_d is sandwiched between two low-index dielectric gap layers with thickness *t* and permittivity ε_g. The top and bottom cladding layers for the whole structure are infinite conductor layers with complex permittivity ε_m, where the dielectric mediums assumed to be lossless, non-magnetic, homogenous, and isotropic.

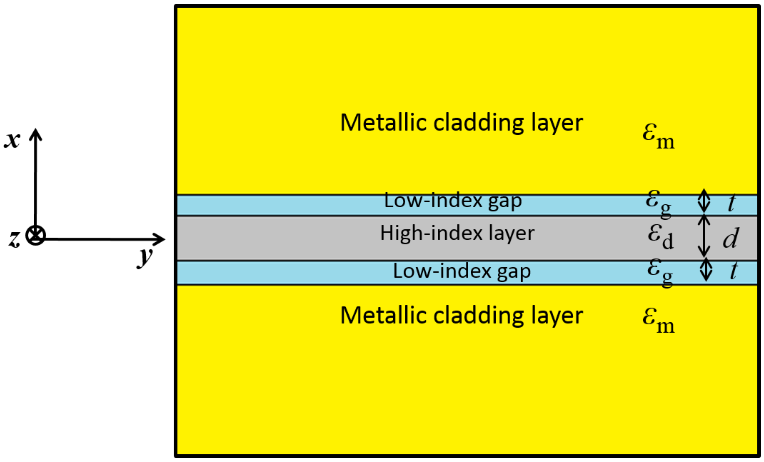

Fig. 40 The schematic geometry of the studied 1D hybrid MDM structure

We assume the geometry infinite in the *y*-direction so that there is no *y*-dependency for the fields of the guided mode which propagate along the *z*-direction and evanescently decay in the *x*-direction. Such a waveguide structure can only support transverse-magnetic (TM) mode. Thus, the wave equation for the magnetic field in each layer can be written as:

$$\nabla^2 \vec{H} - (\beta^2 - k_0^2 \varepsilon_r)\vec{H} = 0, \tag{101}$$

where β is the propagation constant of the guided mode, k_0 is the free-space wave vector, and ε_r is the relative permittivity of each region in the geometry. By utilizing Maxwell's equations for time-harmonic fields, and solving the wave equation Eq. 101, the three non-vanishing fields (E_x, H_y, E_z) of the guided mode can be obtained as:

$$\vec{H} = H_y(x)e^{i\beta z} \tag{102}$$

And

$$\vec{E} = \frac{i}{\omega\varepsilon_r}\left(i\beta H_y \hat{x} - \frac{\partial H_y}{\partial x}\hat{z}\right). \tag{103}$$

By imposing the boundary conditions that the tangential components of electric and magnetic fields as well as the normal components of the electric displacement fields must be continuous at the interfaces between the different regions, the dispersion equation of the hybrid-MDM waveguide mode can be expressed as:

$$e^{k_d d} = \pm \frac{\left[\frac{k_d}{\varepsilon_d} + \frac{(1-r)k_g}{(1+r)\varepsilon_g}\right]}{\left[\frac{k_d}{\varepsilon_d} - \frac{(1-r)k_g}{(1+r)\varepsilon_g}\right]}, \tag{104}$$

where

$$r = e^{-2k_g t} \frac{\left[\frac{k_g}{\varepsilon_g} - \frac{k_m}{\varepsilon_m}\right]}{\left[\frac{k_g}{\varepsilon_g} + \frac{k_m}{\varepsilon_m}\right]}. \tag{105}$$

The wave vectors k_g, k_d, and k_m of the hybrid-MDM guided mode in each region (i.e., high-index layer, low-index gap, and metallic cladding layer), can be expressed as:

$$k_i = \sqrt{\beta^2 - k_0^2 \varepsilon_i}, \text{ where } \quad i = g, d, m. \tag{106}$$

The positive and negative signs in the dispersion relation Eq. (104) correspond to two kinds of hybrid-MDM guided modes supported by the structure. The equation with positive sign refers to the long range symmetrical hybrid-MDM (LRSH-MDM) mode, while the one with negative sign represents the short range anti-symmetrical hybrid-MDM (SRAH-MDM) mode. The characteristic mode equation Eq. (104) can also be written in a transcendental form, for the positive sign:

$$\tanh\left(\frac{k_d d}{2}\right) = \frac{(1-r)k_g \varepsilon_d}{(1+r)k_d \varepsilon_g}, \tag{107}$$

And for the negative sign:

$$\tanh\left(\frac{k_d d}{2}\right) = \frac{(1+r)k_d \varepsilon_g}{(1-r)k_g \varepsilon_d}. \tag{108}$$

We consider only studying the fundamental LRSH-MDM mode because it has lower prpgation loss. To provide an analysis for the optical performance of the hybrid-MDM plasmonic waveguide, we solve the characteristic mode equation Eq. (107) numerically to obtain the propagation constant of the guided mode. The key parameters of the guided mode, the effective modal index n_{eff} and the propagation length L_{p} (the distance where the optical field power decays by 1/e of its initial value), can be written as:

$$n_{eff} = Re\left(\frac{\beta}{k_0}\right), \tag{109}$$

$$L_p = \frac{\lambda}{4\pi Im[n_{eff}]}. \tag{110}$$

At zero low-index gap thickness *t*, the hybrid MDM mode equation Eq. 107 can recast to the conventional MDM plasmonic mode equation:

$$\tanh\left(\frac{k_d d}{2}\right) = -\frac{k_m \varepsilon_d}{k_d \varepsilon_m}. \tag{111}$$

The optical behavior of the hybrid MDM waveguide structure will be studied and compared with the conventional MDM plasmonic waveguide structure at different wavelengths.

5.1.2 Numerical Results and Discussion

5.1.2.1 The Modal Properties

To study the optical properties of the guide mode in the hybrid-MDM waveguide model, we chose the materials for the low and high-index dielectric regions to be silica and silicon due their compatibility with current fabrication techniques, and for the metallic clads to be silver. The influence of the wavelength on the hybrid guide mode will be investigated. The refractive indices of the silicon and silica are n_{Si}=3.477 and n_{SiO2}=1.445 at λ=1550 nm, and n_{Si}=3.461 and n_{SiO2}=1.441 at λ=1800 nm, respectively [25] whereas the permittivities of the silver at these wavelengths 1550 and 1800 nm are $\varepsilon_{\mathrm{Ag}}$=-129+3.3*j* and $\varepsilon_{\mathrm{Ag}}$=-172.78+5.32*j*, respectively [26]. The hybrid MDM guided mode of such a structure results from the coupling between the MDM plasmonic waveguide mode and the conventional dielectric waveguide DW mode which formed at the center 3-layer dielectrics. The evolution of the hybrid guided mode has been governed by the thickness of the center three layers (low-index gap/high-index dielectric/low-index gap), which influences the optical performance of the waveguide.

For this analytical study, the total thickness of the three dielectric layers D=2t+d is fixed while the thickness of the high-index layer is varied d from 0 to D. The five-layer hybrid waveguide structure reduces to the conventional three-layer MDM structure, i.e., metal/low-index-dielectric/metal (MLM) at d=0 and metal/high-index-dielectric/metal (MHM) format, at the case d=D. Firstly, we find the cutoff thickness d_{cutoff} of the dielectric layer in the MDM plasmonic waveguide by using Eq. (57) in order to ensure the MDM plasmonic waveguide supports strong coupled plasmonic mode. The cutoff thickness d_{cutoff} is defined as the separation distance between the metallic layers where the mode effective index n_{eff} of the MDM plasmonic waveguide approaches that of the metal/dielectric single interface plasmonic waveguide ($n_{\text{eff},\infty}$= $\sqrt{\varepsilon_d \varepsilon_m/(\varepsilon_m + \varepsilon_d)}$). Figure 41 illustrates how the cutoff thickness of the 3-layer MDM plasmonic waveguide mode depends on the wavelength, where the metallic layer is chosen to be silver and the dielectric layer is silicon. As the wavelength increases, the cutoff thickness increases. For instance, at the wavelengths 1550 and 1800 nm the cutoff thicknesses are around 900 and 1200 nm respectively. We need to choose the total dielectric thickness D smaller than the cutoff thickness in order to study the 5-layer waveguide at any wavelength.

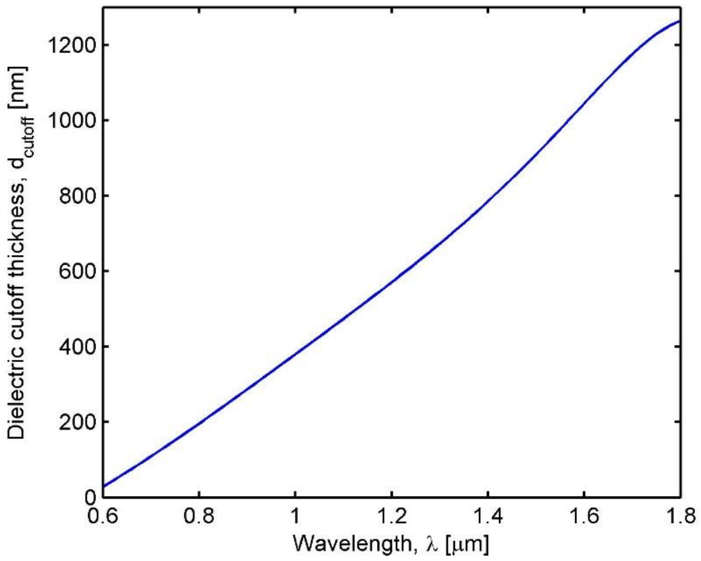

Fig. 41 The dependence of the cutoff dielectric thickness of MDM waveguide on wavelength

The optical properties of the hybrid-MDM guided mode, the modal index and the propagation length, can be investigated by solving the mode characteristics equation Eq. 107 numerically. Figure 42 shows the modal index and the propagation length of the hybrid guided mode at different fixed total dielectric thickness *D* (100, 200, 300, 400, 500nm) for the wavelengths 1550 and 1800 nm. Our results based on the derived-analytical formula agree perfectly with those based on the commercial software COMSOL [87], where they only discussed the optical properties at the total dielectric thickness *D*=300 nm. The two limiting cases *d*=0 and *d*=*D* are illustrated in Fig. 42, which corresponds to the 3-layer Metal/Low-index/Metal (MLM) and the 3-layer Metal/High-index/Metal (MHM) waveguide mode, and the remaining part refers to 5-layer hybrid MDM waveguide mode's optical behavior. We can observe that increasing the high-index layer thickness *d* will increase the modal index monotonously in Fig. 42(a); that means, the modal index of the hybrid MDM mode is always between that of MLM and MHM mode.

It can be noticed that there is a difference between the shape of the curves for the small total thickness *D* (such as: *D* =100, 200 nm) and large *D* (such as: *D* =400, 500 nm). There is a small raised bump presented at the mid-range of *d* for large *D*. Figure 42(b) shows clearly the difference in the shape of the curves of the propagation length. At small total thickness *D*, the propagation length decreases monotonously with increases of the high-index layer thickness *d* as it happens in traditional MDM plasmonic waveguides. On the other hand, at large total dielectric thickness D, there is an interesting optimized dielectric thickness with a maximum propagation length, and the enhancement in the L_{prop} increases as the total dielectric thickness D increases. For D=300 nm, at small d, the propagation length L_{prop} decreases slightly with increases of d and then starts to increase up to a maximum at about d=210 nm, followed by a decreasing trend until it reaches the minimum value for the traditional MHM mode. However, for D=400 and 500 nm, the propagation length increases slightly at small d, then rapidly ramps up until it reaches the maximum L_{prop}. This attributes to that electromagnetic energy penetrated into the metal layers is low as the Ohmic loss of the metal is responsible for the propagation loss. In other words, more energy is distributed in the inner high-index dielectric layer as evidenced by the apparent increase in the modal index. Moreover, with the thickness of high-index layer properly chosen, the inner low/high/low-index dielectric layers may form DW-mode, interacting with SPP-mode. In addition, the enhancement in propagation length for wavelength at 1800 nm is also noticeable but not as much as that at 1550nm; this is intuitively because the Ohmic loss of silver increases as the wavelength increases. The changes in the propagation lengths and the modal index suggest the great influence of the thickness of the dielectric layers on the formation and evolution of the hybrid guided MDM mode. We will continue the discussion about the hybrid-MDM mode at the telecom wavelength 1550 nm.

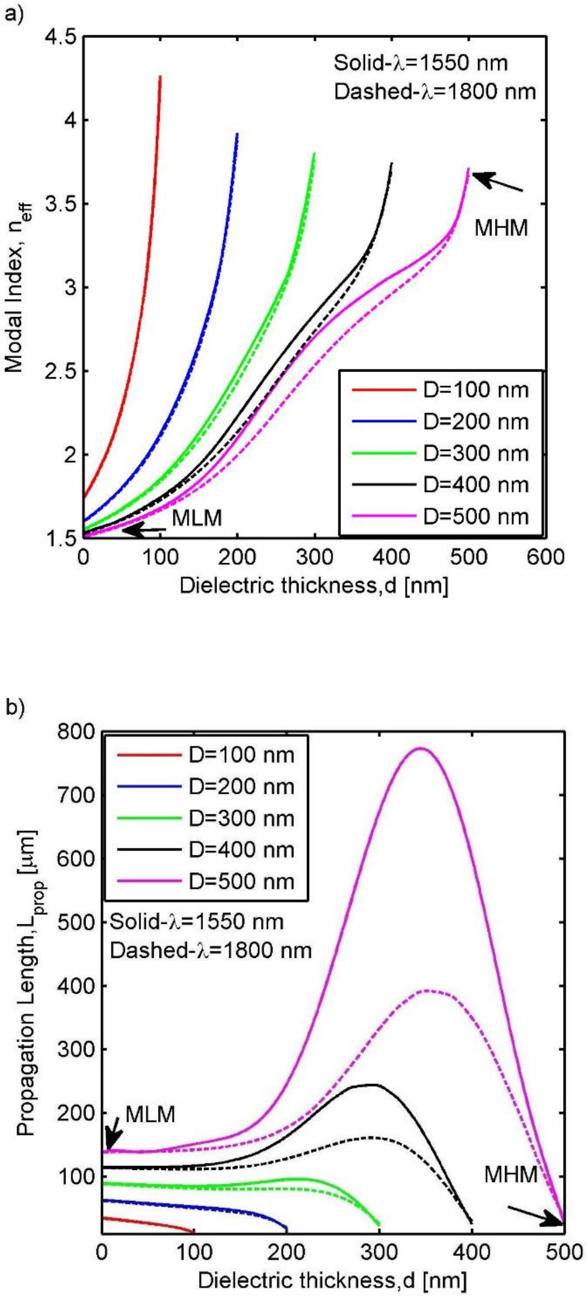

Fig. 42 The modal index (a) and propagation length (b) of the hybrid–MDM guided mode at wavelengths 1550 and 1800 nm, at different dielectric thicknesses D=100,200,300,400, and 500 nm

5.1.2.2 Energy Flux Density

The propagating power of the guided mode within the hybrid-MDM waveguide structure can be visualized by plotting the energy flux density of the hybrid guided MDM mode along the *x*-direction. The energy flux density can be expressed by time averaging the *z*-component of the poynting vector value:

$$S_z = \frac{1}{2} Re\left(\vec{E} \times \vec{H}^*\right) \cdot \hat{z}, \tag{112}$$

where and the propagation constant of the hybrid-MDM mode can be obtained by solving the mode equation Eq. 107, and the transverse fields components E_x and H_y from Eq.102 and Eq. 103. Figure 43 shows the energy flux density of the hybrid-MDM mode for different dielectric thicknesses *d* and at fixed total dielectric thickness *D*=400 nm. The special cases at *d*=0 and *d*=*D* for the traditional 3-layer MLM and MHM mode are shown in Fig. 43(a) and 43(d). In Fig. 43(b) and 43(c), the power is gradually shifted from the low-index to high-index layer with insertion of high-index layer at center, resulting in the evolution of the hybrid MDM mode. Thus, we can notice how the geometrical parameters of the dielectric low- and high-index layers *t* and *d* influences the formation of the hybrid MDM mode.

In addition, Also note that the field of hybrid guided mode is distributed mainly within the dielectric layers and it decays rapidly to zero in the metal layers, as can be seen from Fig. 43. Even though infinite thickness of the conductor layer is assumed in our theoretical modeling, in practical applications, a metal cladding layer of a few μm thickness is sufficient to have no effect on the hybrid modes.

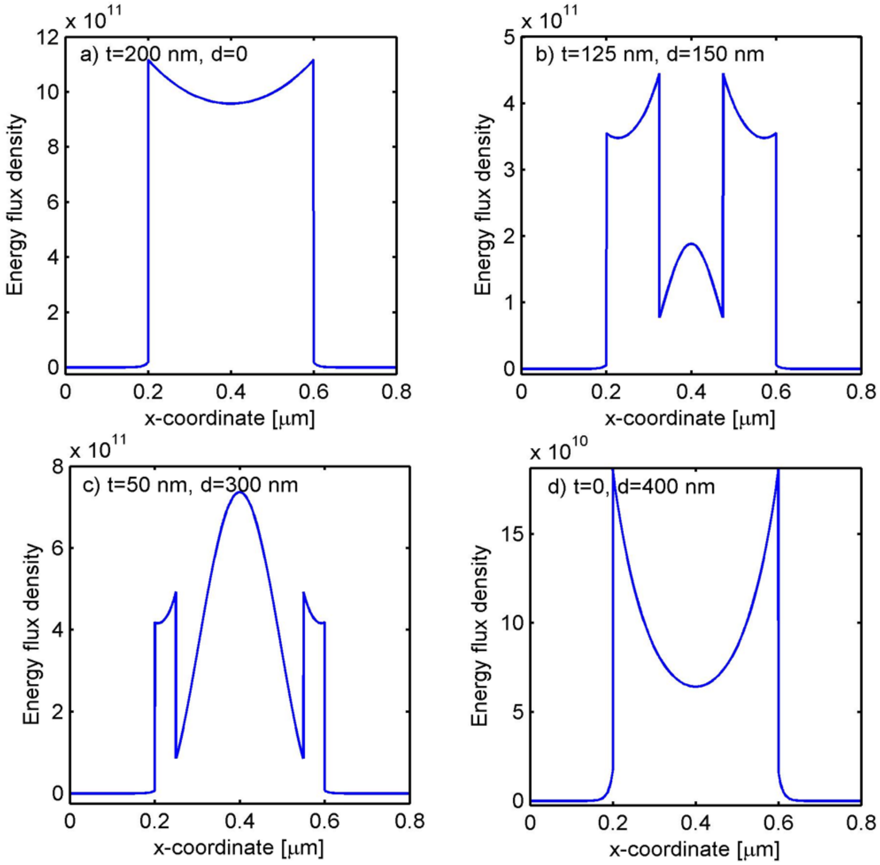

Fig. 43 The energy flux density of the hybrid-MDM guide mode at fixed *D*=400, where the dielectric thicknesses are a) *t*=200 nm & *d*=0, b) *t*=125 nm & *d*=150 nm, c) *t*=50 nm & *d*=300 nm, and d) *t*=0, & *d*=400 nm

Moreover, the propagating power in *z*-direction has been plotted by using COMSOL's mode solver in one and two dimensions. Figure 44 illustrates the surface plot for the guided modes' propagating power supported by the Ag/SiO_2/Si/SiO_2/Ag hybrid waveguide at different gap and dielectric thicknesses and a fixed total thickness *D*=400, while their corespondence1D plot of the propagating power as a function of *x* is shown in Fig. 45. At *D*=2*t*=400 nm, the propagating power field is strongly confined within the low-index gap region leading to form Metal-Low-index-gap-Metal (MLM) waveguide mode in the absence of the high-index layer as shown in Fig. 44(a) & Fig. 45(a). In the presence of the high-index layer, we can see the evolution of the MDM hybrid plasmonic waveguide mode as shown in Fig. 44(b) and Fig. 44(c) and Fig. 45(b) and Fig. 45(c). It is noticeable how the geometrical parameters have an impact on the MDM hybrid mode's formation. As the low index gap decreasing from 125 to 50 nm, we can see how the power fields penetrates from the low-index gap region to high-index region. The physical interpretation about the MDM hybrid mode characteristics will be discussed in detail in the next section. As the low-index gap thickness vanishes, the power field of the guide mode will be the conventional Metal-High-index-Metal (MHM) plasmonic waveguide mode as shown in Fig. 44(d) and Fig. 45(d).

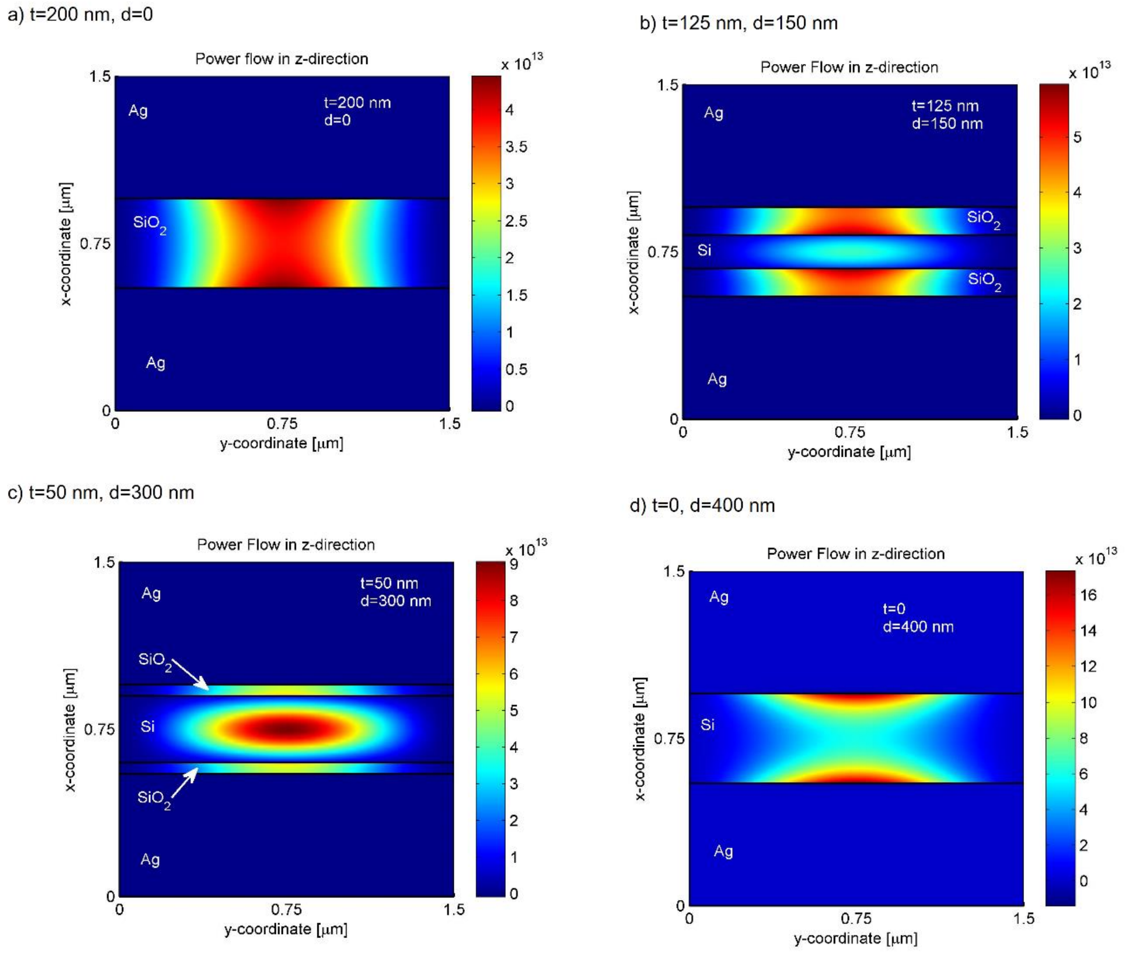
a) t=200 nm, d=0

b) t=125 nm, d=150 nm

c) t=50 nm, d=300 nm

d) t=0, d=400 nm

Fig. 44 The surface plot for the energy flux density of the hybrid MDM mode at fixed D=400 nm and different gap and high-index dielectric thicknesses, a) *t*=200 nm and *d*=0, b) *t*=125 and *d*=150 nm, c) *t*=50 and *d*=300 nm, and d) *t*=0 and d=400 nm.

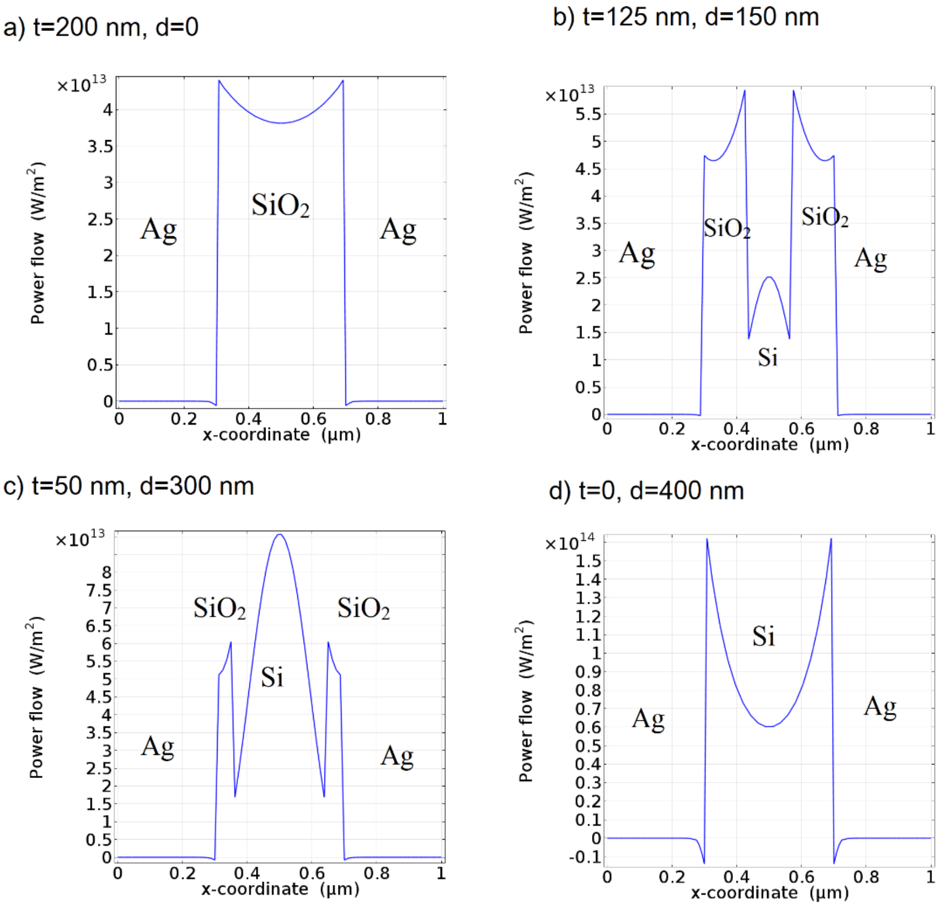

Fig. 45 The power flow of the hybrid MDM guided mode as a function of *x* at fixed total dielectric thickness D=400 nm and different gap and dielectric thicknesses, a) [*t*, *d*]=[200, 0]nm, b) [*t*, *d*]=[125, 150]nm, c) [*t*, *d*]=[50, 300]nm, c)[*t*, *d*]=[0, 400] nm

5.1.3 The Hybrid-MDM Mode Evolution

The evolution of the hybrid-MDM mode can be understood clearly by using the two criteria for mode characterization that we have introduced in the previous chapter, which mainly based on the maximum energy flux density in the low-index gap and the high-index dielectric regions ($P_{\max,g}$ & $P_{\max,d}$). The first criterion is that the peak energy density in the high index dielectric region is at 1/e of that in the low-index gap, ($P_{\mathrm{max,d}}/P_{\mathrm{max,g}}=1/\mathrm{e}$), and the second criterion is that the energy peak densities are equal in both regions, ($P_{\mathrm{max,g}}/P_{\mathrm{max,d}}=1$).

The ratio of the energy flux density $P_{\mathrm{max,g}}/P_{\mathrm{max,d}}$ as a function of the high-index layer thickness d for different total dielectric thicknesses D=100, 200, 300, 400 and 500 nm is illustrated in Fig. 45. At the limit case d=0, the guided mode is the traditional MLM mode. As d increases the ratio of energy flux density decreases, which means the power in the low-index layers starts to transfer into the high-index layer, leading to the formation of the hybrid-MDM mode. The power ratio continues to reduce until it reaches a minimum value, and then starts to increase until $d=D$, yielding the traditional MHM mode. We notice that the larger the total dielectric thickness D, the smaller is the minimum ratio of the energy flux density.

We can discuss in detail the evolution of the hybrid-MDM mode by applying the criteria for mode characteristics. The hybrid-MDM mode can be classified into five hybrid-MDM mode types at large dielectric thicknesses D=400 and 500 nm, as shown in Fig. 46. For instance, at the largest total dielectric thickness D=500 nm, the first criteria is satisfied at d=140 nm. When d is smaller than 140 nm, the hybrid mode behaves as a strong SPP-like MLM mode as the power is mainly distributed in the low-index layer. The energy flux density distribution of this type of mode at d=50 nm is displayed in Fig. 47(a). As d further increases, the second criteria is satisfied (see the two dotted circles at $d_1\approx207$ and $d_2\approx460$ nm). When the peak power ratio $P_{\mathrm{max,d}}/P_{\mathrm{max,g}}$ falls between 1/e ($d\approx140$ nm) and unity ($d_1\approx207$ nm), the hybrid mode is referred to as a medium SPP-DW-like MLM mode because of the strong coupling between the SPP and DW modes, as can be seen from the energy flux density profile in Fig. 47(b). In the region between the two dotted circles (or two squares) where the power peaks are equal, the power is mainly confined in the high-index layer at the center. Therefore, such a waveguide structure supports the 3rd-type of mode: strong DW-like mode; the energy flux density distribution of this type of mode is shown in Fig. 47(c). The hybrid-MDM mode types will be symmetrically depending on weather the mode closes to the MLM or MHM mode nature since the studied plasmonic waveguide structure is symmetrical. Consequently, with further increasing d, the 4th and the 5th type of the hybrid-MDM modes are the medium SPP-DW-like MHM mode and strong SPP-like MHM mode, respectively, as shown in Fig. 47 (d) and Fig. 47(e). It is worth pointing out that in the middle region in Fig. 46, associated with the strong DW-like mode, there are the minimum energy flux densities located respectively at $d_{\mathrm{opt}}\approx290$ and 340 nm for D=400 and 500 nm. Referring back to Fig. 42(b), we can see that at the same dielectric thickness d_{opt}, the propagation lengths are maximized, which are increases of about 160% and 460% compared to those at d=0 for the traditional MLM mode for D=400 and 500 nm, respectively.

However, at D=300 nm, the first criterion can only be applied as shown in Fig. 46. That means although power begins to couple to the high-index layer, the power in the low-index layers still dominates over that in the high-index layer, leading to form only three types of modes (strong SPP-like MLM mode, medium SPP-DW-like MLM mode, and strong SPP-like MHM mode). The minimum ratio of the energy flux density occurs at $d_{\mathrm{opt}}\approx210$ nm, where again slight enhancement in the propagation length takes place, referring back to Fig. 42. At small dielectric thicknesses D=100 and 200 nm, the two criteria are not applicable. Hence, the hybrid-MDM mode types are the strong SPP-like MLM mode and the strong SPP-like MHM mode. The lack of the presence of DW-like mode explains why there is no improvement in the propagation length for small dielectric thicknesses D=100 and 200 nm in Fig. 42. In other words, the excitation of the DW-like mode plays an essential role in improving the propagation length of the hybrid guided mode, as the more the power retains in the center regime, the less the power in the metal. Therefore, the Ohmic loss can be decreased. When the energy flux density in the center reaches its peak value, the optimized propagation length can be achieved.

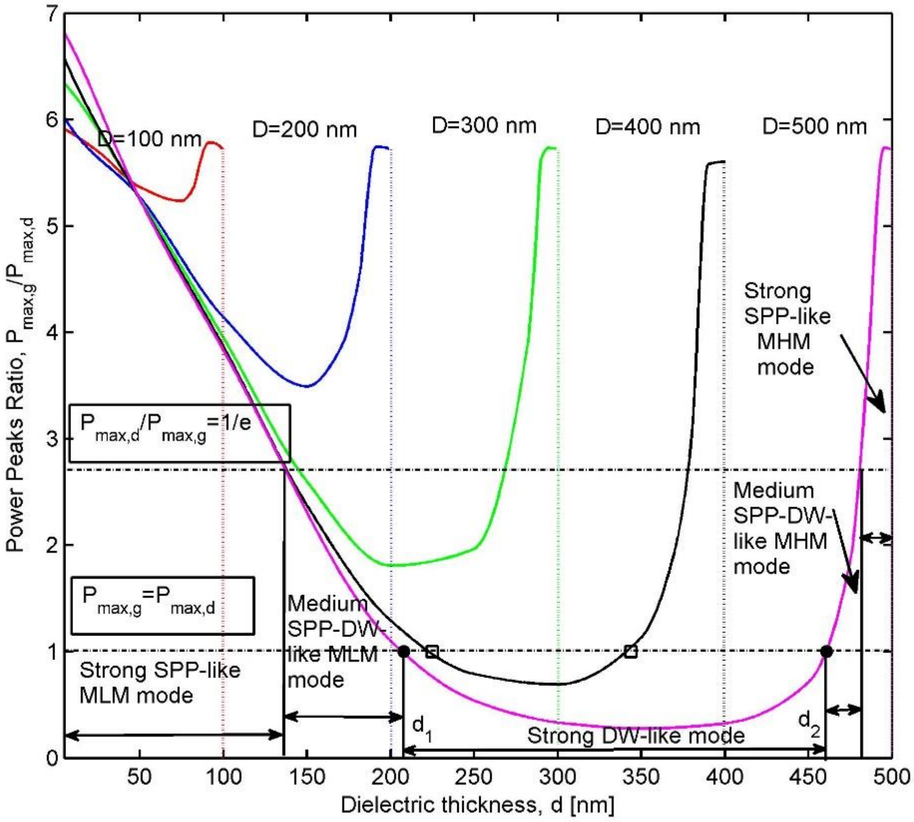

Fig. 46 The power peaks ratio versus the dielectric thickness *d* at different *D*=100, 200, 300, 400, and 500 nm, with two criteria shown.

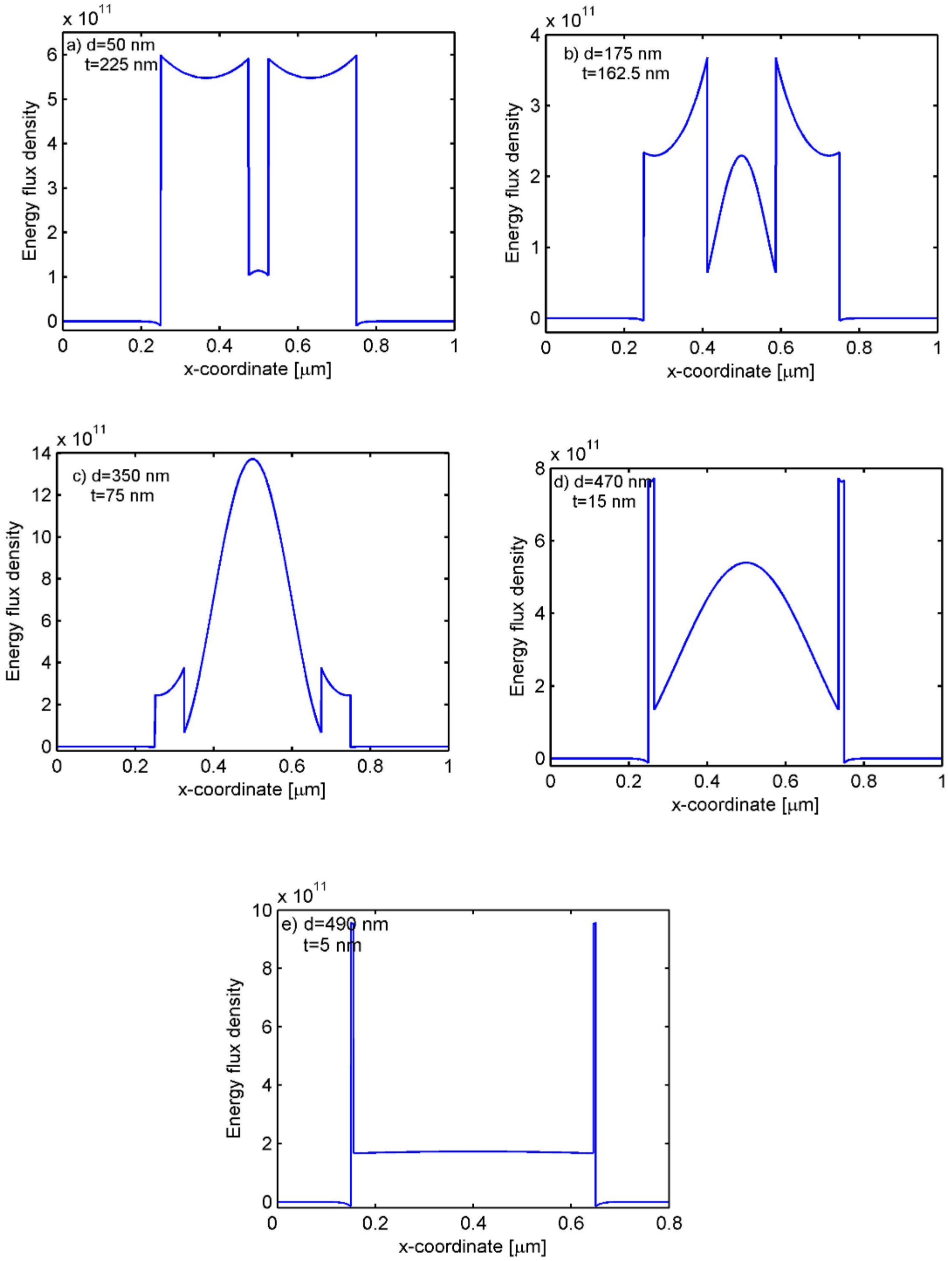

Fig. 47 The energy flux density of the five types of the hybrid MDM mode at D=500 nm

5.1.4 Hybrid-MDM Mode Confinement

The mode confinement of the different types of the hybrid-MDM modes can be investigated in terms of the confinement factor and the effective mode size. The confinement factor Γ, defined as the ratio of the power distribution within the dielectric layers to the overall power distributed in the waveguide, can be expressed as:

$$\Gamma = \frac{\frac{1}{2}\int_{g,d} Re(\vec{E}\times\vec{H}^{*})\cdot\hat{z}dx}{\frac{1}{2}\int_{whole} Re(\vec{E}\times\vec{H}^{*})\cdot\hat{z}dx}. \tag{113}$$

The confinement factor of the hybrid-MDM waveguide structure is shown in Fig. 48. It can be seen that such a structure can support large amount of power residing within the dielectric layers; this arises from the well-known fact that MDM waveguides have very strong mode confinement. For small total dielectric thicknesses (*D*=100, 200 nm), the confinement factor of the hybrid MDM mode falls between that of the MLM and the MHM mode. As the total dielectric thickness *D* increases, the confinement factor of the hybrid-MDM mode is slightly improved with increasing the dielectric thickness *d*, which relates to the excitation of the DW-like mode.

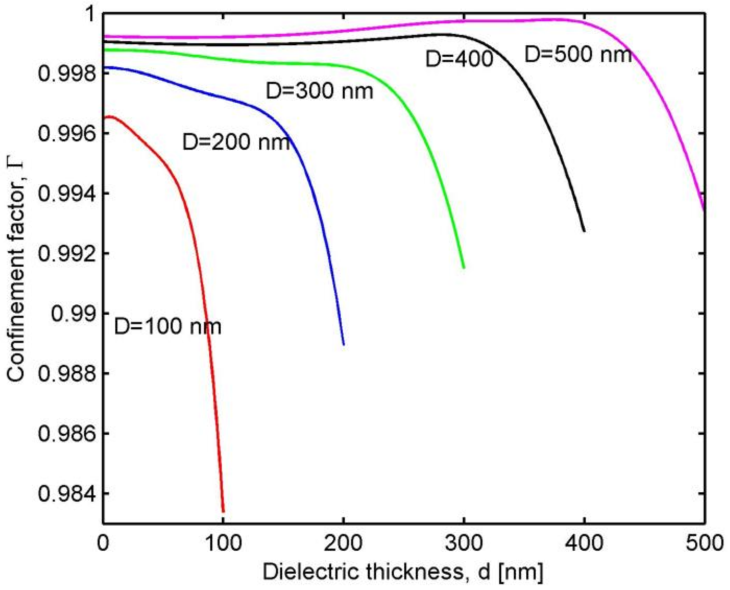

Fig. 48 The confinement factor of the guided mode versus dielectric thickness *d*, at different dielectric thickness *D*=100, 200, 300, 400, and 500 nm

The mode confinement can be also interpreted in terms of the effective mode size L_{ms}, which is defined as the ratio of the total modal energy flux along the *x*-direction to its maximum energy flux density; it can be written as [82, 84]:

$$L_{ms} = \frac{\int_{-\infty}^{\infty} S_z dx}{\max(S_z)}. \tag{114}$$

The normalized mode size L_{norm} of the hybrid-MDM mode, ($L_{\mathrm{norm}}=L_{\mathrm{rm}}/L_0$, where $L_0=\lambda/2$), calculated from our derived analytical formula, at different total dielectric thickness is shown in Fig. 49. As the total dielectric thickness decreases, the mode size reduces. For example, at small dielectric thicknesses D=100, 200 and 300 nm, the mode size decreases monotonously as the dielectric thickness d increases, which means the hybrid MDM mode size is larger than that of the MHM mode and smaller than that of the MLM mode. On the other hand, the mode size behaves differently at large total dielectric thickness. For D=400 nm, there are two localized peaks at d_1=220, d_2=340 nm, and d_1=207, d_2=460 nm for D=500 nm, respectively. Referring back to Fig. 46, d_1 and d_2 are just the thicknesses where the 2nd criteria are satisfied. The thickness d with the minimum mode size for D=400 and 500 nm in Fig. 49, within this region ($d_1<d<d_2$) associated with the DW-like mode, is nearly the thickness d with the minimum power ratio of the energy flux density and the maximum propagation length referring to Fig. 46 and Fig. 42(b). It is worth noting that choosing the optimal high-index dielectric thickness d, the hybrid MDM waveguide with maximum propagation length and relatively small mode size along with large confinement factor can be achieved for large total dielectric thickness D, where the hybrid-MDM mode behaves as DW-like mode. Another minimum mode size is localized at $d \approx 170$ nm in the regime having medium-SPP-DW-like MLM mode, where the mode size is decreased by 29% for both D=400 and 500 nm as shown in Fig. 49, and the propagation length is increased by 18% and 40% for D=400 and 500 nm, respectively, compared with the MLM mode in Fig. 42. Furthermore, for D=300 nm, at the thickness $d_{\mathrm{opt}} \approx 210$ nm with optimum propagation length, as seen in Fig. 42, the mode size is reduced by 38% where the hybrid mode exhibits medium-SPP-DW-like MLM mode behavior.

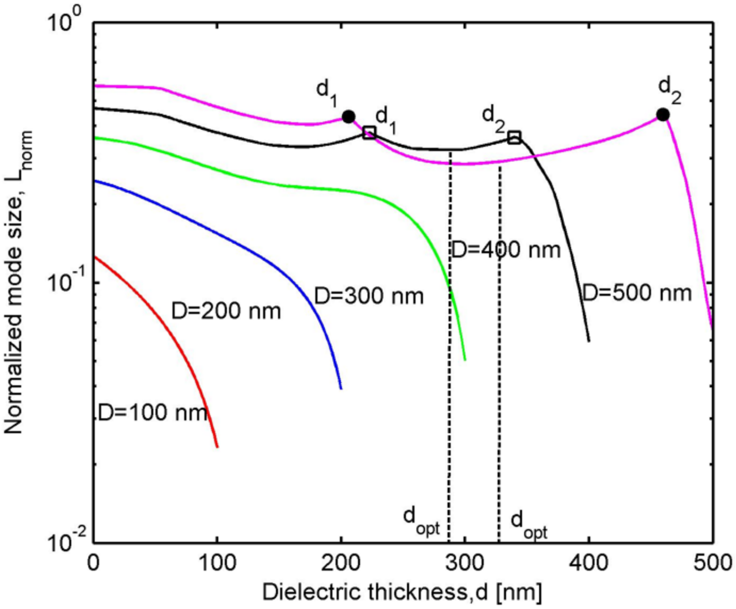

Fig. 49 the dependence of the normalized mode size of the hybrid-MDM mode on the dielectric thickness *d* at different total dielectric thicknesses *D*=100, 200, 300, 400, and 500 nm.

In our analytical study of the hybrid-MDM waveguide structure, we can notice that the hybrid guided mode behaves basically as the traditional MDM-like mode with little improvement on its optical performance at small total dielectric thickness *D*. On the other hand, although the mode size naturally increases at large total dielectric thickness *D*, the enhancement in the propagation length in the region supporting medium SPP-DW-like MLM mode can be achieved. The largest propagation length and mode confinement along with relatively small mode size can be specifically obtained by choosing the optimized high-index thickness *d* in the region which supports the DW-like mode.

The interesting behavior of the modal index of the hybrid-MDM mode, at large total dielectric thickness *D*=400 and 500 nm, in Fig. 42(a) can be correlated with the evolution of the hybrid mode as confirmed by the results obtained above. The modal index, for large *D*, increases smoothly until reaching the middle region (with small bump) where the modal index slope changes, first increases and then decreases. After that, the modal index returns to the behavior at small *d*, and increases rapidly until the modal index reaches to the one of the MHM mode. The change of the modal index in the middle region, associated with medium SPP-DW-like MLM mode and DW-like mode, shown in Fig. 42(a) truly reflects the evolution of the hybrid guided MDM mode as shown in Fig. 46. This can be attributed to the strength of the mode coupling from SPP mode to DW mode, and can also be observed from the variation in the mode size, shown in Fig. 49.

5.1.5 The Effect of the Dielectric Layers on the Modal Properties of the Hybrid-MDM Waveguide Loss

The importance of the low/high/low-index inner dielectric layers on the enhancement of the propagation length in hybrid MDM waveguides will be discussed. The arrangement of low/high/low-index layers permits to the excitation of the DW-like mode as in traditional DWs. Thus, the field is significantly improved in the high-index region and decreased in the low-index regions, leading to the field reduction in the metal layers. Therefore, the propagation length of the hybrid-MDM mode can be significantly increased. However, if we instead utilize another arrangement (high/low/high-index) structure, such a structure can not form DW-like mode, resulting in no enhancement in the propagation length. Figure 50(a) and (b) shows the modal index and the propagation length for the high/low/high-index structure with fixed $D = 400$ nm. By switching the low and high-index layers, the core is now the low-index layer. Hence, $d = 0$ and $d = 400$ becomes the traditional MHM and MLM structure, respectively. Accordingly, the modal index decreases with increasing the low-index layer. It can be noticed that at the middle range of *d*, there is a small index bump rises. That means, strong field is distributed in high-index layers, which are adjacent to the outer metal layers, yielding to more power penetration into the metal layers. As result, the propagation length is even reduced at middle range of *d*, as shown in Fig. 50(b). Consequently, the only arrangement of the dielectric layers that makes the 5-layer hybrid MDM an excellent plasmonic waveguide is the (low/high/low-index) structure.

In addition, we can study how the refractive index contrast between the high and low index layer in the low/high/low structure influences the waveguide optical performance. Figure 51(a) and (b) illustrate our calculated results on the modal index and the propagation length at $D = 400$ nm for fixed low-index material SiO_2 with different high-index materials Ge, Si and CdS whose refractive indices are 4.275, 3.477 and 2.3, respectively. The index difference between the high-index layer (Ge, Si, CdS) and low-index layer (SiO_2) are 2.83, 2.03, and 0.855, respectively. Figure 51(b) shows that the large index difference is beneficial to further improve optical performance. For example, the propagation length for Ge surges about 373% comparing with that for Si. On the other hand, the improvement of the propagation length is very minimal if CdS is used as a high-index layer, due to the relatively small index contrast. As the index difference varied, the line shapes of the modal index in Fig. 51(a) change accordingly. The larger the index contrast, the higher the rising bump in the middle region becomes and the stronger the field distributes in the core, leading to the enhancement of the propagation lengths. Finally, both the dielectric index contrast and the geometrical dimensions of the hybrid-MDM waveguide have a great impact on its optical performance.

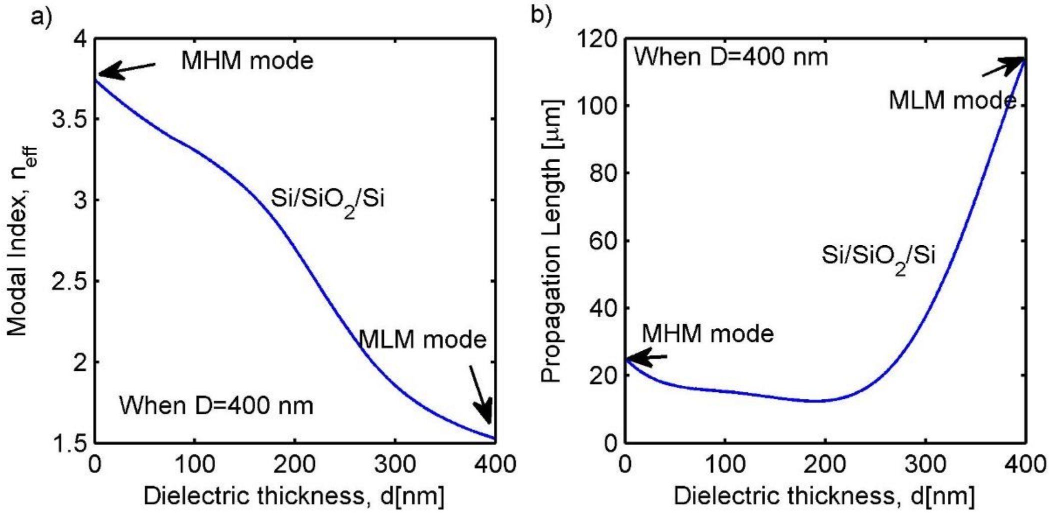

Fig. 50 The optical properties of the hybrid mode generated by metal/high/low/high/metal (MHLHM) structure a) modal index and b) propagation length, versus the dielectric thickness d, when D = 400 nm.

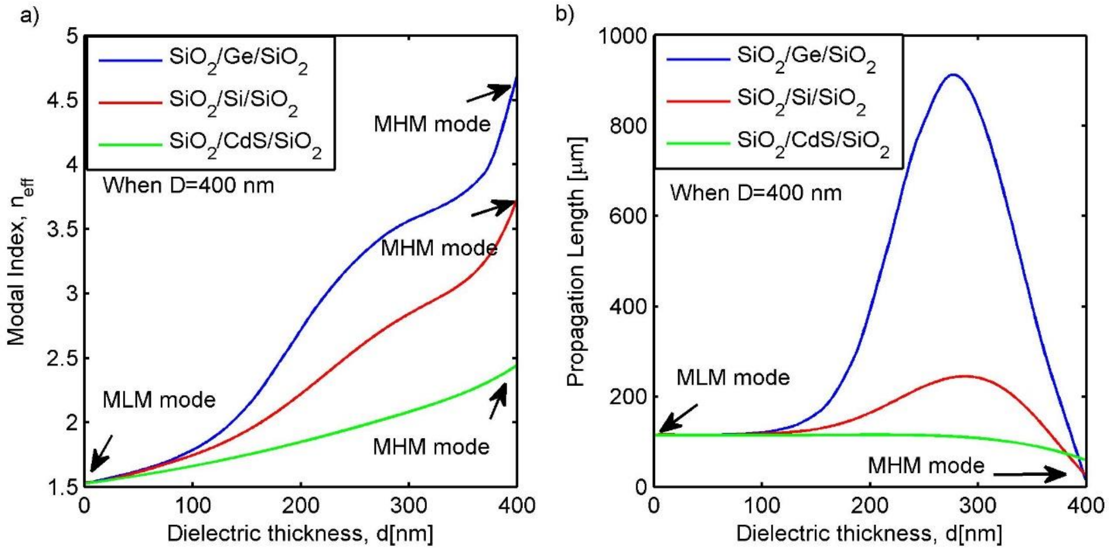

Fig. 51 The modal index (a) and the propagation length (b) of the hybrid-MDM mode versus the dielectric thickness *d* at different dielectric refractive indices, when D=400 nm.

5.1.6 The propagation Characteristics of the Hybrid-MDM Modes

As seen, the optical properties of the dielectric layers have played a crucial role on the optical performance of the hybrid-MDM guided modes. The effect of the refractive index of the high index dielectric core layer on the propagation length enhancement will be investigated [90]. We kept the total dielectric layers thickness *D* fixed at 400 nm, and the refractive index of the low-index gap chosen to be silica (SiO_2) with a refractive index 1.445 at the telecom wavelength 1550 mm. We studied the effect of variation the refractive index of the core layer (high-index layer) n_d on the waveguide performance. Figure 52 shows the maximum propagation length L_{max} and the optimized thickness *d* at L_{max} versus the dielectric refractive index n_d. Our results show that large index contrast leads to great enhancement in L_{max}. When there is no high-index layer (i.e. n_d=0, *d*=0), the guided mode will be the traditional MLM waveguide mode. As the refractive index n_d increases from 0 to 1.445 (same as the low-index gap), there is no evolution of the hybrid MDM mode, just exhibit MLM mode and MHLHM mode. Therefore, there is no enhancement in the propagation length in this region. With increasing the refractive index n_d from 1.445 to 2.2, there is also no improvement in the maximum value of propagation length. This attributes to the low index contrast between the low and high-index dielectric materials, as discussed above in Fig. 51; referring back to Fig. 51(b) we can see the low index contrast of (CdS/SiO_2) exhibits minimal improvement in the propagation length. However, as the index increasing from ~2.3 to 3, the propagation length starts to enhance a little and the thickness of the optimized high-index layer increases sharply as shown in Fig. 52(b). This indicates the evolution of strong SPP-like in this region, which exhibits low propagation length compared to the next regions, where the index contrast increases. With the further increasing the index contrast, the propagation length noticeably improves, and the thickness of the optimized high-index layer becomes flat (when n_d increases from 3 to 4), and further starts to decreases (from $n_d > 4$), which associated with the evolution of the hybrid guided modes from strong dielectric waveguide (DW)-like, to extremely strong DW-like modes.

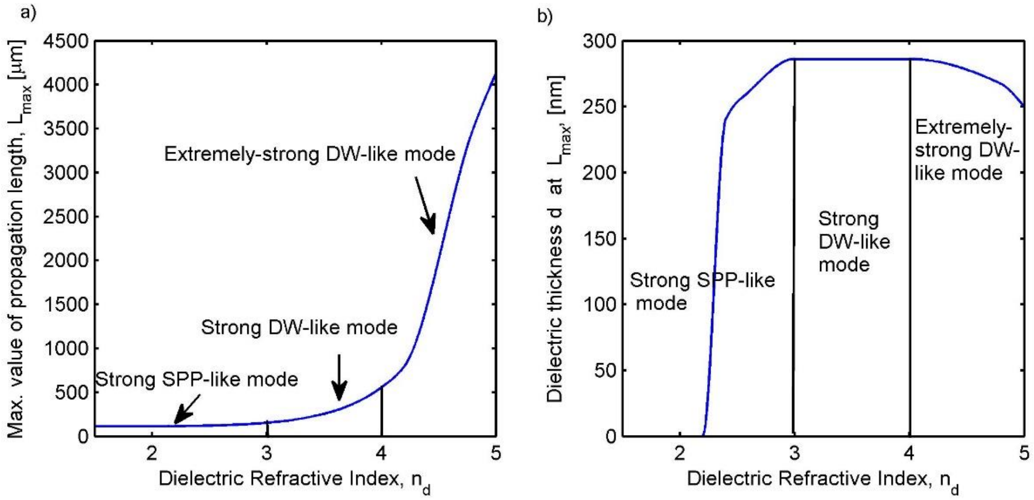

Fig. 52 The effect of the dielectric refractive index on (a) the maximum propagation length, and (b) the optimized thickness *d* at L_{max}

5.2 Conclusion

The guided mode in a multilayer symmetrical hybrid-MDM plasmonic waveguide have been studied theoretically based on using our analytically derived expressions. We found that there are different types of hybrid-MDM modes supported by the hybrid waveguide structure based on our proposed mode characteristic criteria. At small total dielectric thickness, the hybrid guided mode always exhibits strong SPP-like behavior no matter how the thickness of the high-index layer varies. On the contrary, for large total dielectric thickness, the thickness of the high-index layer plays an essential role in determining if the hybrid guided mode is SPP-like, SPP-DW-like, or DW-like, which can significantly affect the modal index, the propagation length, the mode size as well as the mode confinement factor. As result, the waveguide optical performance could be tailored by suitably choosing the proper geometrical parameters. Moreover, we revealed the necessity of the structure of inner low/high/low-index layer and the effect of the index difference between high- and low-index layers on the optical performance of the hybrid MDM waveguides. Such a waveguide structure has potential applications in sub-wavelength all-optical data processing plasmonics devices.

Chapter 6

Conclusion and Future Work

6.1 Summary of the Contributions

Plasmonic waveguides (PWs) have been a subject of considerable interest over the past decade due to their ability to manipulate light on deep subwavelength scales beyond the diffraction limit at a metal-dielectric interface, leading to the development of ultra-compact active/passive nanophotonic devices. One major drawback of PWs which can not be ignored is the high propagation loss due to Ohmic loss of metals at optical frequencies. The hybrid plasmonic waveguide (HPW) is a recent novel type of PWs, which consists of a subwavelength low-index dielectric region embedded between metal and high-index dielectric cladding layers. It has been proposed to tackle the issue of the high propagation of PWs. The capability of the HPW to support a strong confined guided mode within subwavelength nanoscale structure with a lower propagation loss has motivated nanophotonics community to exploit its outstanding merits. Various waveguide structures have been proposed based on the HPW in order to improve its performance, such as symmetrical cylindrical and planar geometries. Most of the theoretical studies are conducted by using commercial available mode solver's software in order to analyze the hybrid guided mode and examine its modal properties. Comprehending the hybrid mode deeply requires theoretical studies in order to investigate all the key factors that may intensify the waveguide optical performance with a higher degree of accuracy, which can effectively help the waveguide designers to obtain a deep analysis before fabricating plasmonic waveguide devices. Thus, the main objective of this dissertation was to provide thorough theoretical studies for the hybrid guided modes for different types of multilayer hybrid plasmonic waveguides structures based on derived equations due to the lack of such theoretical studies.

In Chapter 2, the recent excitement about nanoplasmonic technology was discussed. The essential principle and concepts, such as such Drude model, Maxwell's equation, and the mode equation are included in order to understand the electromagnetics of the surface plasmon polaritons (SPPs) guided modes of PWs. The dispersion equation of the SPPs mode at single metal-dielectric interface has been derived and its optical properties were investigated. In the third Chapter, plasmonic waveguides were introduced; in particular, Dielectric-Metal-Dielectric (DMD), Metal-Dielectric-Metal (MDM), and

Hybrid Plasmonic waveguides were investigated theoretically based on deriving their guided mode equations, studying their optical performance, plotting their field's profile, and discussing their advantages and disadvantages, as well as their potential applications. The mode solver of COMSOL software was utilized throughout the whole theoretical studies in this thesis for the purpose of comparison between our analytical-based results and software-based results. The guided modes of PWs are also investigated in different dimensions.

In Chapter 4, the optical behavior of the guided mode in a five-layer Symmetrical Conductor-Gap-Dielectric (SCGD) plasmonic waveguide structure was theoretically analyzed. We found the condition for the existence of the hybrid guided mode in the proposed waveguide structure, which is the low-index gap thickness should be smaller than the cutoff gap thickness. The dispersion equation of the SCGD guided mode as well as the cutoff gap thickness condition were analytically derived. The SCGD guided mode was numerically characterized based on the analytical equations for different index contrast ratios of the cladding to the gap layers. At large index contrast ratio, the SCGD mode can be guided within a few nanometers gap thickness. Such a waveguide structure can support ultra-long range SPPs mode with relatively lower propagation loss compared to that of the typical DMD waveguide mode. Even though the propagation length can be substantially increased near the cutoff gap thickness, it may not be practical to fabricate such a waveguide.

Fortunately, this issue associated with the 5-layer structure was solved by a 7-layer hybrid-DMD plasmonic structure by replacing the infinite high-index dielectric cladding layers with a finite thickness and introducing infinite low-index cover layers: the bottom substrate and the top cover. As a result, we presented a comprehensive analytical theoretical investigation for the hybrid guided mode supported by the 7-layer hybrid-DMD plasmonic waveguide. The presence of the cover cladding layers eliminated the cutoff condition of the gap thickness of the 5-layer hybrid-DMD plamonic waveguide. We classified the guided mode into three types according to our two criteria which proposed for studying the mode characteristics of the 7-layer HPW. In addition, we examined the optical performance of the waveguide structure with analyzing the normalized mode size, confinement factor, and the FOM. Our results agreed perfectly with the results based on the commercial software. By properly choosing the geometrical parameters as well as the dielectric materials, this waveguide structure can support subwavelength strong mode confinement with higher propagation length compared to the three-layer HPW.

A thorough theoretical analysis for the 5-layer hybrid-MDM plasmonic waveguide was presented in Chapter 5. Such a waveguide geometry has been proposed to reduce the high propagation loss accompanied with the typical MDM plasmonic waveguide. The guided mode's equation for the hybrid-MDM plasmonic waveguide was derived. Based on our analytical equations, the overall optical performance of the guided mode such as modal index, propagation length, normalized mode size, and the confinement factor was studied comprehensively. We found that different types of modes, SPP-like, SPP-DW-like, and DW-like mode, can be supported by the hybrid-MDM waveguide structure. For example, at small total dielectric thickness, the hybrid-MDM guided mode exhibits always SPP-like mode; however, at large total dielectric thickness, the guided mode can take different forms of the hybrid mode relying on the high-index dielectric thickness which plays a crucial role on the guided mode's formation. In addition, the waveguide optical performance was dominated by the index difference between the high- and low-index regions and the total dielectric layers. Therefore, the waveguide structure can be highly optimized for building on-chip all optical processing devices, by controlling the waveguide geometrical parameters as well as the optical properties of the materials.

6.2 Future Work

The optical performance of the multilayer hybrid-DMD and hybrid-MDM plasmonic waveguides was successfully investigated based on analytical derived equations. The proposed multilayer hybrid plasmonic waveguide structures have shown a better compromise between mode confinement and propagation loss compared to the typical three-layer HPW, DMD, and MDM plasmonic waveguide, by utilizing optimized geometrical parameters and choosing suitable materials optical properties. The great field enhancement and the essential merits of the proposed studied multilayer hybrid plasmonic waveguides make them excellent candidates for applications in active and passive nanoplasmonic devices. Constructing ultra-compact high-density plasmonic integrated circuits demands all-optical data processing devices in order to switch, route, and modulate data within the circuit. In electronic devices, processing data is performed nonlinearly. Thus, in order to implement high speed all-optical switching devices, nonlinear domains are required to be incorporated into devices. Since nonlinear interactions can be typically observed at very high field intensity, the strong field enhancement within the low index gap of the multilayer hybrid plasmonic waveguides makes them ideal elements to build nonlinear all-optical switching devices, which demands extremely high field intensity, low power consumption, and miniscule switching time. To extend our research, a nonlinear medium can be incorporated into the low-index dielectric layer, and the nonlinear mode equation of the guided modes can be derived for our studied different types of hybrid plasmonic waveguides. The nonlinear optical behavior of the hybrid modes can be fully investigated based on the analytical derived equations.

The analytical model of the nonlinear multilayer hybrid plasmonic waveguides can help optimizing the waveguide geometries to achieve higher nonlinear performance, and designing all-optical switching devices. Different schemes of nonlinear switching devices can be utilized in order to see which one can provide a better nonlinear switching performance. Various nonlinear materials can be also used for further enhancement. Designing such a nonlinear all-optical switching device can really open the possibility to process, modulate, and route data in all-optical domain, and can help to design nanoplasmonic integrated circuits for the future of “all-optical computers”.

Bibliography

[1] R. P. Feynman, "There's Plenty of Room at the Bottom," Eng. Sci, vol. 23, pp. 22-36 (1959).

[2] J.A. Conway, S. Sahni, and T. Szkopek, "Plasmonic interconnects versus conventional interconnects a comparison of latency, cross-talk and energy costs," Opt. Express, vol. 15, no. 8, pp. 4474-4484 (2007).

[3] E. Ozbay, "Plasmonics: Merging Photonics and Electronics at Nanoscale Dimensions," Science, vol.311, pp. 189-193 (2006).

[4] R. Zia, J. A. Schuller, A. Chandran, and M. L. Brongersma, "Plasmonics: the next chip-scale technology," Mater. Today, vol. 9, pp. 20–27 (2006).

[5] W. L. Barnes, A. Dereux, and T. W. Ebbesen, "Surface Plasmon subwavelength optics," Nature, vol.424, pp.824-830 (2003).

[6] S. A. Maier and H. A. Atwater, "Plasmonic: localization and guiding of electromagnetic energy in metal/dielectric structures," J. Appl. Phys., vol. 98, 011101 (2005).

[7] G. Veronis and S. Fan, "Bends and splitters in metal-dielectric-metal subwavelength plasmonic waveguides," Appl. Phys. Lett., vol.87, no.13, p. 131102 (2005).

[8] N. N. Feng, M. L. Brongersma, and L. D. Negro, "Metal-dielectric slot-waveguide structures for the propagation of surface Plasmon polaritons at 1.55 μm," IEEE J. Quantum Electron., vol. 43, no. 6, pp.479–485 (2007).

[9] P. Berini, "Long-range surface plasmon polaritons," Adv. Opt. Photon., vol. 1, no. 3, pp. 484-588 (2009).

[10] E. P. Fitakis, T. Kamalakis, and T. Sphicopoulos, "Slow light in insulator-metal-insulator plasmonic waveguides," J. Opt. Am. B, vol. 28, o. 9, pp. 2159-2164 (2011).

[11] M. Z. Alam, J. Meier, J. S. Aitchison, and M. Mojahedi, "Super mode propagation in low index medium," in Proc. CLEO/QELS , JThD112 (2007).

[12] R. F. Oulton, V. J. Sorger, D. A. Genov, D. F. P. Pile, and X. Zhang, "A hybrid plasmonic waveguide for subwavelength confinement and long-range propagation," Nat. Photonics, vol. 2, no.8, pp. 496–500 (2008).

[13] D. J. Griffiths, "Introduction to Electrodynamics," 4th edition, Pearson Education Inc. (2013), Chapter-7, pp. (340-342).

[14] S. A. Maier, "Plasmonics Fundametnlas and Apllications," ISBN 978-0387-33150-8, Springer (2007), Chapter-2, pp. (21-22).

[15] S. A. Maier, “Plasmonics: Fundamentals and Applications,” ISBN 978-0387-33150-8, Springer (2007), Chapter-2, pp. (25-27).

[16] S. Aldawsari, “Nonlinear Hybrid Plasmonic Waveguides,” Master Thesis, Waterloo University, 2013.

[17] S. A. Maier, “Plasmonics: Fundamentals and Applications,” ISBN 978-0387-33150-8, Springer (2007), Chapter-1, pp. (11-15).

[18] Otto, “Excitation of nonradiative plasma surface waves in silver by method of frustrated total reflection,” Z. Phys., vol. 216, pp. 398-410 (1968).

[19] R. H. Ritchie, E. T. Arakawa, J. J. Cowan, and R. N. Hamm, “Surface Plasmon resonance effect in grating diffraction,” Phys. Rev. Lett., vol. 21, no. 22, pp. 1530-1533 (1968).

[20] COMSOL Multiphysics 4.3b, http://www.comsol.com

[21] D. F. P. Pile and D. K. Gramotnev, “Channel plasmon–polariton in a triangular groove on a metal surface Opt. Lett., vol. 29, no. 10, pp. 1069-1071 (2004).

[22] E. Moreno, F. J. Garcia-Vidal, S. G. Rodrigo, L. Martin-Moreno, and S.I. Bozhevolnyi, “Channel plasmon-polaritons: modal shape, dispersion, and losses,” Opt. Lett., vol. 31, no. 23, pp. 3447-3449 (2006).

[23] Y. Fang, H. Wei, F. Hao, P. Nordlander, H. Xu, “Remote-excitation surface-enhanced Raman scattering using propagating Ag nanowire plasmons,” Nano Lett., vol. 9, no. 5, pp. 2049–2053 (2009).

[24] S. A. Maier, “Plasmonics: Fundamentals and Applications,” ISBN 978-0387-3315-8, Springer (2007), Chapter-2, pp. (30-32).

[25] W. J. Tropf, M. E. Thomas, and E. W. Rogala, Handbook of Optics, McGraw Hill, 3rd Ed, p2.64.

[26] P. B. Johnson and R. W. Christy, “Optical consatnts of the noble metals,” Phys. Rev. B, vol. 6, no. 12, pp. 4370-4379, 1972.

[27] J. Grandidier, S. Massenot, G. Colas des Frances, A. Bouhelier, J.-C. Weeber, L. Markey, and A. Dereux, “Dielectric-loaded surface plasmon polariton waveguides: Figures of merit and mode characterization by image and Fourier plane leakage microscopy,” Phys. Rev. B, vol. 78, no. 24, p. 24519 (2008).

[28] D. Sarid, ‘‘Long-range surface-plasma waves on very thin metal films,’’ Phys. Rev. Lett., vol.47, pp. 1927–1930 (1981).

[29] J. J. Burke, G. I. Stegeman, and T. Tamir, ‘‘Surface polariton-like waves guided by thin, lossy metal films,’’ Phys. Rev. B, vol. 33, pp. 5186–5201 (1986).

[30] F. Yang, J. R. Sambles, and G. W. Bradberry, ‘‘Long-range surface modes supported by thin films,’’ Phys. Rev. B, vol. 44, pp. 5855–5872 (1991).

[31] R. Zia, M. D. Selker, P. B. Catrysse, and M. L. Brongersma, “Geometries and materials for subwavelength surface plasmon modes,” J. Opt. Soc. Am. A, vol. 21, no. 12, pp. 2442-2446 (2004).

[32] E. Moreno, F. J. Carcia-Vida, S. G. Rodrigo, L. Martin-Moreno, and S. I. Bozhevolnyi, “Channel plasmon-polaritons: moda, and losses,” Opt. Lett., vol. 31, no. 23, pp 3447-3449 (2006).

[33] S. I. Bozhevolnyi, V. S. Volkov, E. Devaux, J. Y. Lalute, and T. W. Ebbesen, “Channel Plasmon subwavelength waveguide comonents including interferometre and ring resonators,” Nature, vol. 440, no. 7083, pp. 508-511 (2006)

[34] T. Wu, Y. Liu, Z. Yu, Y. Peng, C. Shu, and H. Ye, “The sensing characterstics of plasmonic waveguide with a ring resonator,” Opt. Express, vol. 22, no. 7, pp. 7669-7677 (2014).

[35] Y. Xie, Y. Huang, W. Zhao, W. Xu, and C. He, “A Novel Plasmonic Sensor Based on Metal–Insulator–Metal Waveguide With Side-Coupled Hexagonal Cavity,” IEEE Photonics Journal, vol. 7. No. 2, pp. 1-12 (2015).

[36] J. Tao, Q. Wang, X. Haung, “All-optical plasmonics switches bsed on coupled nano-disk cavity structures containing nonlinear material,” Plasmonics, vol. 6, pp. 753-759 (2011).

[37] S. Paul and M. Ray, “Plasmonic switching and bistability at telecom wavelength using the subwavelength nonlinear cavity coupled to a dielectric waveguide: A theoretical approach,” J. Appl. Phys., vol. 120, no. 303102, pp. 1-9 (2016).

[38] Q. Zhang, X. Haung, X. Lin, J. Tao, and X. Jin, “A subwavelength coupler-type MIM optical filter,” Opt. Express, vol. 17, no. 9, pp. 7549-7554 (2009).

[39] G. Zhan, R. Liang, H. Liang, J. Liu, and R. Zhao, “Asymmetric band-pass plasmonic nanodisk filter with mode inhibition and spectrally splitting capabilities,” Opt. Express, vol. 22, no. 8, pp. 9912-9919 (2014).

[40] J. Mao, X. Zhai, L. Wang, and H. Li, “Numerical analysis of near-infrared plasmonic filter with high figure of merit based on Fano resonance,” Appl. Phys. Express, vol. 10, no. 082201, pp. 1-4 (2017).

[41] M. Z. Alam, J. S. Aitchison, and M. Mojahedi, “A mariage of convenience: Hybridization of surface plasmon and dielectric waveguide modes,” Laser Photonics Rev., vol. 8, no. 3, pp. 394-408 (2014).

[42] D. Dai and S. He, “ A silicon-based hybrid plasmnic waveguide with a metal cap for a nano-scale light confinement,” Opt. Express, vol. 17, no. 19, pp. 16646-16653 (2009).

[43] J. T. Kim, “CMOS-compatible hybrid plasmonic wavguide for subwavelength light confinment and on-chip integration,” IEEE Photon. Technol. Lett., vol. 23, no. 4, pp. 206-208 (2011).

[44] D. Dai and S. He, “ Low loss hybrid plasmonic waveguide with double low-index nano-slots,” Opt. Express, vol. 18, no. 17, pp. 17958-17966 (2010).

[45] M. Z. Alam, J. Meier, J.S. Aitchison, and M. Mojahedi, “Propagation characterstics of hybrid modes supported by metal-low-high index waveguides and bends,” Opt. Express, vol. 18 no. 12, pp. 12971-12979 (2010).

[46] Y. Kue, F. Ye, and X. Chen, “Low-loss hybrid plasmonic waveguide for compact and high efficient photonic integration,” Opt. Express, vol. 19, no. 12, pp. 11746-11752 (2011).

[47] H. S. Chu, E. P. Li, P. Bai, and R. Hegde, “Optical performance of single-mode hybrid dielectric-loaded plasmonic waveguide-based components,” Appl. Phys. Lett., vol. 96, bo. 22, 221103 (2010).

[48] Y. Bian, Z. Zheng, X. Zhao, L. Liu, Y. Su, J. Liu, J. Zhu, and T. Zhou, “Hybrid plasmon polariton guiding with tight mode confinement in a V-shaped metal/dielectric groove,” J. Opt, vol. 15, no. 5, 055011 (2013).

[49] V. J. Sorger, Z. Ye, R. F. Oulton, Y. Wang, G. Bartal, X. Yin, and X. Zhang, “Experimental demonstration of low-loss optical waveguiding at deep sub-wavelength scales,” Nature Comm, vol. 2, no. 331, (2011).

[50] V. A. Zenin, S. Choudhury, S. Saha, V. Shalaev, A. Boltasseva, and S. I. Bozhevolnyi, “Hybrid plasmonic waveguides formed by metal coating of dielectric ridges,” Opt. Express, vol. 25, no. 11, pp. 12295-12302 (2017).

[51] I. Avrutsky, R. Soref, and W. Buchwald, “Sub-wavelength plasmonic modes in a conductor-gap-dielectric syetem with a nanoscale gap,” Opt. Express, vol. 18, no. 1, pp. 348-363 (2010).

[52] Y. Fang and M. Sun, “Nanoplasmonic waveguides: towards applications in integrated nanophotonic circuits,” Light: Science & Applications, vol. 4, e294 (2015).

[53] J. Wang, X. Guan, Y. He, Y. Shi, Z. Wang, S. He, P. Holmstrom, L. Wosinski, L. Thylen, and D. Dai, “Sub-μm^2 power splitters by using silicon hybrid plasmonic waveguides,” Opt. Express, vol. 19, no. 2, pp. 838-847 (2011).

[54] S. Zhu, G. Q. Lo, and D. L. Kwong, “Metal-Insulator-Si hybrid plasmonic waveguide components for on-chip photonics,” *IEEE Asia Pacific Conference on Anntenas and Propagation*, August 27-29, 2012, Singapore.

[55] M. Z. Alam, J. N. Caspers, J. S. Aitchison, and M. Mojahedi, “Compact low loss and broadband hybrid plasmonic directional coupler,” Opt. Express, vol. 21, no. 13, pp. 16029-16034 (2013).

[56] M. M. Hossain, M. D. Turner, and M. Gu, “Ultrahigh nonlinear nanoshellplasmonic waveguide with total energy confinement,” Opt. Express, vol. 19, no. 24, pp. 23800-23808 (2011).

[57] A. Pitilakis, O. Tsilipakos, and E. E. Kriezis, “Nonlinear effects in hybrid nonlinear plasmonic waveguides,” *4th International Conference on Transperent Optical Networks (ICTON)*, 2012 England, pp. 1-4.

[58] S. Aldawsari and B. R. West, “Hybrid plasmonic waveguides for nonlinear applications,” *IEEE Photonics Global Conference (PGC)*, 2012 Singapore, pp. 1-4.

[59] F. J Diaz, G. Li, C. M. Sterke, B. T. Kuhlmey, and S. Palomba, “Kerr effect in hybrid plasmonic waveguides,” J. Opt. Am. B, vol. 33, no. 5, pp. 957-962 (2016).

[60] A. Pitilakis and E. E. Kriezis, “Highly nonlinear hybrid silicon-plasmonic waveguides: analysis and optimization,” J. Opt. Soc. Am. B, vol. 30, no. 7, pp. 1954–1965 (2013).

[61] K.Y. Wang, and A.C. Foster. “Optimization of CMOS-Compatible Hybrid Plasmonic Waveguides for Nonlinear Applications,” in Advanced Photonics OSA Technical Digest (Optical Society of America, 2011), paper JTuB15.

[62] F. J. Diaz, T. Hatakeyama, J. Rho, Y. Wang, K. O’Brien, X. Zhang, C. M. Sterke, B. T. Kuhlmey, and S. Palomba, “Sensitive method for measuring third order nonlinearities in compact dielectric and hybrid plasmonic waveguides," Opt. Express, vol. 24, no. 1, pp. 545-554 (2016).

[63] J. Zhang, P. Zhao, E. Cassan, and X. Zhange, “Phase regeneration of phase shft keying signals in highly nonlinear hybrid plasmonic waveguides,” Opt. Lett., vol. 38, no. 6, pp. 845-850 (2013).

[64] R. F. Oulton, V.G. Sorger, T. Zentgraf, R. M. Ma, C. Gladden, L. Dai, G. Bartal, and X. Zhang, “Plasmon lasers at deep subwavelength scale,” Nature, vol. 461, pp. 629-632 (2009).

[65] Z. Li, Y. Wang, J. He, D. Feng, E. Gu, W. Li, “An ultraviolet hybrid plamonic waveguide for nanolaser applications,” Photonics and Optica Journal, vol. 6, no. 8B, pp. 19-23 (2016).

[66] L. Zhu, “Modal properties of hybrid plasmonic waveguides for nanolaser applications,” IEEE Photon Tech. Lett., vol. 22, no. 8, pp. 535-537 (2010).

[67] L. Zhi-Quan, P. Rui-Qi, Z. Jing-Jing, M. Xiao-Yun, and T. Kai, “A low-threshold nanolaser on hybrid plasmonic waveguides at the deep subwavelength scale,” Chin. Phys. B, vol. 24, no. 7, pp. (1-7) 077303 (2015).

[68] W. Wei, X. Yan, X. Zhange, “Ultrahigh Purcell factor in low-threshold nanolaser based on asymmetric hybrid plasmonic cavity,” Scientific Reports, vol. 6, pp. 1-7, 33063 (2016).

[69] B. You, J. Lu, T. Liu, and J. Ping, “Hybrid terahertz plasmonic waveguide for sensing applications,” Opt. Express, vol. 21, no. 18, pp. 21087-21096 (2013).

[70] M. Z. Alam, F. Bahrami, J. S. Aitchison, M. Mojahedi, “Analysis and optimization of hybrid plasmonic wavehuides as a platform for biosensing,” IEEE Photon. J, vol. 6, no. 4, 3700110 (2014).

[71] D. Travo, “Theorey of a plasmonic waveguide biosensor for the detection of turbid analytes,” M.Sc. thesis, University of Windsor, 2013.

[72] H.Reather, “Surface Plasmons on Smooth and Rough Surface and on Gratings,” Springer, Berlin (1988).

[73] P. Berini, “Plasmon-Polariton waves guided by thin lossy metal films of finite width: Bound modes of symmetirc structure,” Phys. Rev. B, vol. 61, no. 15, pp. 1044-10503 (2000).

[74] A. Degiron and D. Smith, “Numerical simulations of long-range plasmons,” Opt. Express, vol. 14, no. 4, pp. 1611-1625 (2006).

[75] Y. Bian, Z. Zheng, X. Zhao, J. Zhu, and T. Zhou, “Symmetric hybrid surface Plasmon polariton waveguides for 3D photonic integration,” Opt. Express, vol. 17, no. 23, pp.21320-21325 (2009).

[76] L. Chen, T. Zhang, X. Li and W.P. Huang, “Novel hybrid plasmonic waveguide consisting of two identical dielectric nanowires symmetrically placed on each side of a thin metal film,” Opt. Express, vol. 20, no. 18, pp. 20535-20544 (2012).

[77] L. Wei, S. Aldawsari, W. Liu, and B. R. West, “Theoretical analysis of plasmonic modes in a symmetric conductor–gap–dielectric structure for nanoscale confinement,” IEEE Photonics Journal, vol.6, no.3, pp.1-10 (2014).

[78] S. Aldawsari, L. Wei, and W.K. Liu, “Theoretical Study of Hybrid Guided Modes in a Multilayer Symmetrical Planar Plasmonic Waveguide,” J. Lightwave Technol., vol. 33, no. 15, pp.3198-3206 (2015).

[79] R. Adato and J. Guo, “Characteristics of ultra-long range surface Plasmon waves at optical frequency,” Opt. Express, vol. 15, no. 8, pp.5008-5017 (2007).

[80] M. A. Noginov, G. Zhu, A. M. Belgrave, R. Bakker, V. M. Shalaev, E. E. Narimanov, S. Stout, E. Herz, T. Suteewong, and U. Wiesner, “Demonstration of a spaser-based nanolaser,” Nature, vol. 460, no. 7259, pp.1110–1112 (2009).

[81] M. Amin, M. Farhat, and H. Bagci, “A nonlinear plasmonic esonator for three-state all-optical switching,” Opt. Express, vol. 22, no. 6, pp. 6966-6976 (2014).

[82] L. Chen, X. Li, and G. Wang, “ A hybrid long-range plsmonic waveguide with sub-wavelength confinement,” Opt. Commun. , vol. 291, pp. 400-404 (2013) .

[83] P. Berini, “Figures of merit for surface plasmon waveguides,” Opt. Express, vol. 14, no. 26, pp. 13030-13042 (2006).

[84] L. Gao, L. Tang, F. Hu, R. Guo, X. Wang, and Z. Zhou, “ Active metal strip hybrid plasmonic waveguide with low critical material gain,” Opt. Express, vol. 20, no. 10, pp. 11487-11495 (2012).

[85] J. Grandidier, S. Massenot, G. Colas des Francs, A. Bouhelier, J.-C. Weeber, L. Markey, and A. Dereux, “Dielectric-loaded surface plasmon polariton waveguides: Figures of merit and mode characterization by image and Fourier plane leakage microscopy,” Phys. Rev. B, vol. 78, no. 245419, pp. 1-9 (2008).

[86] J. T. Kim, “CMOS-compatible hybrid plasmonic waveguide for subwavelength light confinement and on-chip integration,” IEEE Photonics letters, vol. 23, no. 4, pp. 206-208 (2011).

[87] Y. Bian and Q. Gong, “optical performance of one-dimensional hybrid metal-insulator-metal structures at telcom wavwelength,” Opt. Commun., vol. 308, pp. 30-35 (2013).

[88] S. Aldawsari, L. Wei, and W. K. Liu, "A Comprehensive Theoretical Study of the Guided Modes in a Five-Layer Hybrid-Metal/Dielectric/Metal Waveguide," J. Lightwave Technol., vol. 35, no. 11, pp. 2243-2251 (2017).

[89] J. W. M. Chon and K. Iniewski, “ Nanoplasmonics Advanced Device Applications,” CRC Press, NW (2014).

[90] S. Aldawsari, L. Wei, and W. K. Liu, “Propagation Characteristics of Hybrid Guided Modes in a 5-layer Metal/Dielectric/Metal Waveguide,” *Photonics North Conference*, June 6-8, 2017, Ottawa, ON, Canada.

[91] M. N. Sadiku, “Numerical Techniques in Electromegnetics,” (CRC Press Inc., Folrida, 1992), p. 407-440

Appendix A

COMSOL's MODE SOLVER

In this appendix, a full report has been generated by using COMSOL software mode solver based on the finite element method (FEM) numerical method in order to solve the guided mode within the plasmonic waveguide structure and provide a computational analysis [91]. The concept of the FEM depends on four basic steps. Firstly, the solution domain is divided into thousands of small shapes, which called mesh elements. Then, Maxwell's equations and the governed partial differential equations are found in each element of the mesh; thirdly, all the mesh elements are assembled. Finally, the general solution for the electromagnetic problem can be evaluated by solving all the equation with the suitable boundary conditions. Hence, the guided modes can be solved by obtaining the effective mod index, propagation length, and plotting their fields' profile.

Single Interface SPPs

Contents

1 Global Definitions

1.1 Parameters 1

Parameters

Name	Expression	Description
d	.5	Dielectric thickness
WD	.8	Domain Width
HD	.3	Domain height
nAgR	.1453	Real refractive index of metal
nAgI	-11.3587	Imaginary part index of metal
ng	3.455	Dielectric refractive index
wl	1.55e-6[m]	wavelength
f0	c_const/wl	frequency
nSeed	3.501589 + 0.004673i	Initial guess

2 Model 1 (mod1)

2.1 Definitions

2.1.1 Coordinate Systems

6.2.1.1 Boundary System 1

Coordinate system type	Boundary system
Identifier	sys1

Settings

Name	**Value**
Coordinate names	{t1, n, to}
Create first tangent direction from	Global Cartesian

2.2 Geometry 1

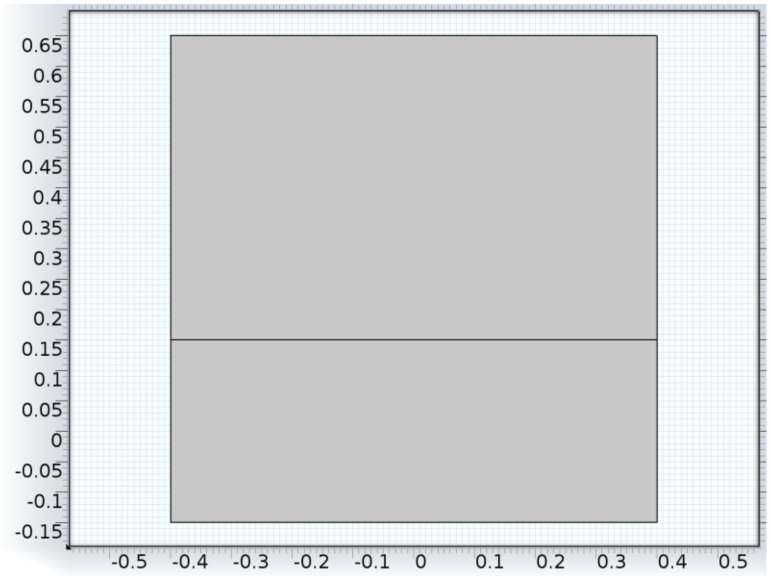

Geometry 1

Units

Length unit	µm
Angular unit	deg

Geometry statistics

Property	Value
Space dimension	2
Number of domains	2
Number of boundaries	7

2.2.1 Metal (r1)

Position

Name	Value
Position	{0, 0}
Base	Center
Width	WD
Height	HD
Size	{WD, HD}

2.2.2 Dielectric (r3)

Position

Name	Value
Position	{0, (HD/2) + (d/2)}
Base	Center
Width	WD
Height	d
Size	{WD, d}

2.3 Materials

2.3.1 Silver

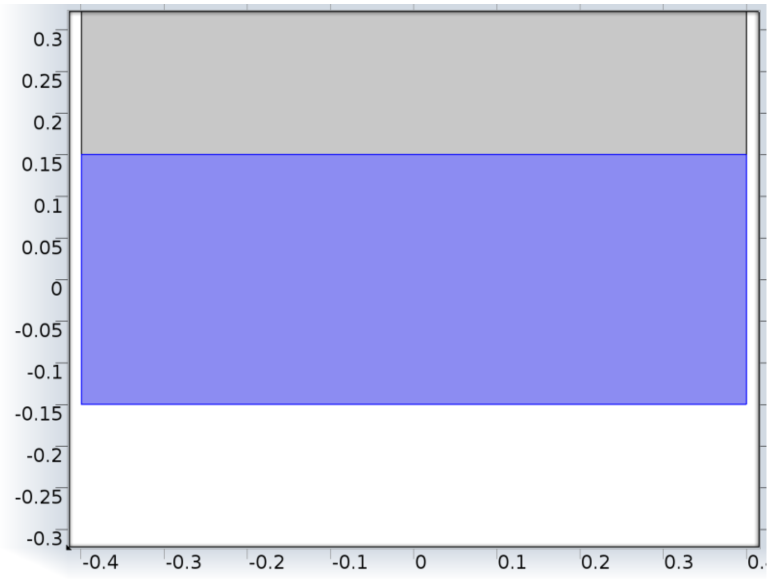

Silver

Selection

Geometric entity level	Domain
Selection	Domain 1

Material parameters

Name	Value	Unit
Refractive index	nAgR	1
Refractive index, imaginary part	nAgI	1

Refractive index Settings

Description	Value
Refractive index	{{nAgR, 0, 0}, {0, nAgR, 0}, {0, 0, nAgR}}
Refractive index, imaginary part	{{nAgI, 0, 0}, {0, nAgI, 0}, {0, 0, nAgI}}

2.3.2 Si

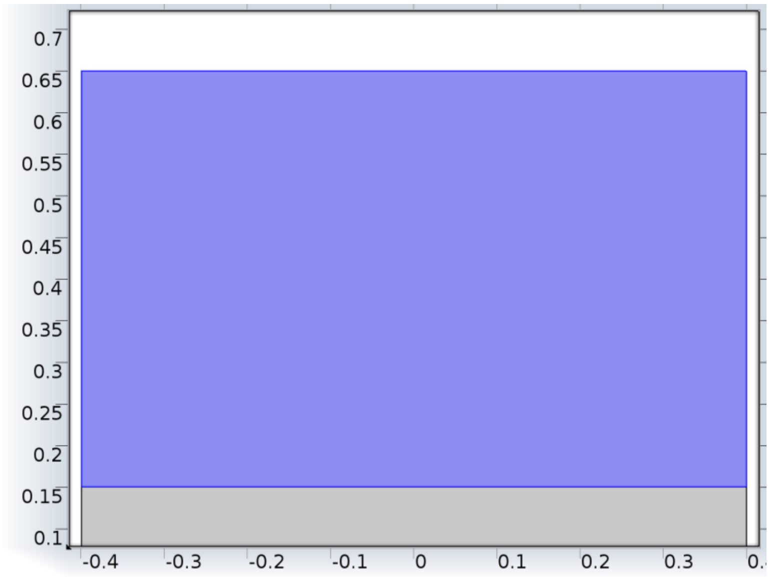

Si

Selection

Geometric entity level	Domain
Selection	Domain 2

Material parameters

Name	Value	Unit
Refractive index	ng	1
Refractive index, imaginary part	0	1

Refractive index Settings

Description	Value
Refractive index	{{ng, 0, 0}, {0, ng, 0}, {0, 0, ng}}
Refractive index, imaginary part	{{0, 0, 0}, {0, 0, 0}, {0, 0, 0}}

2.4 Electromagnetic Waves (emw)

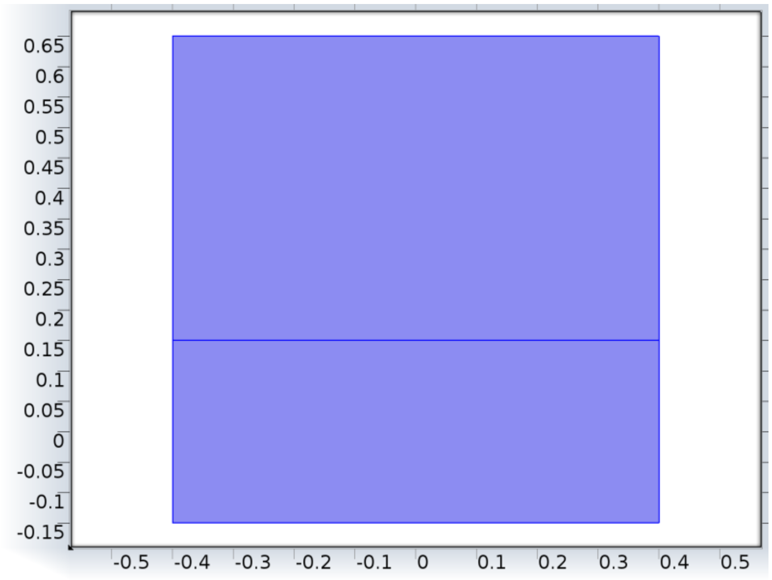

Electromagnetic Waves

Selection

Geometric entity level	Domain
Selection	Domains 1–2

Equations

$$\nabla \times \mu_r^{-1}(\nabla \times \mathbf{E}) - k_0^2\left(\epsilon_r - \frac{j\sigma}{\omega\epsilon_0}\right)\mathbf{E} = \mathbf{0}$$

$$\lambda = -j\beta - \delta_z$$

Settings

Description	**Value**
Electric field	Quadratic
Value type when using splitting of complex variables	Complex
Equation form	Study controlled
Frequency	1e9[Hz]
Mode analysis frequency	1e9[Hz]

Description	**Value**
Electric field components solved for	Three-component vector
Solve for	Full field
Activate port sweep	0
Sweep on	Ports
Show equation assuming	std1/mode
Out-of-plane wave number	0

2.4.1 Wave Equation, Electric 1

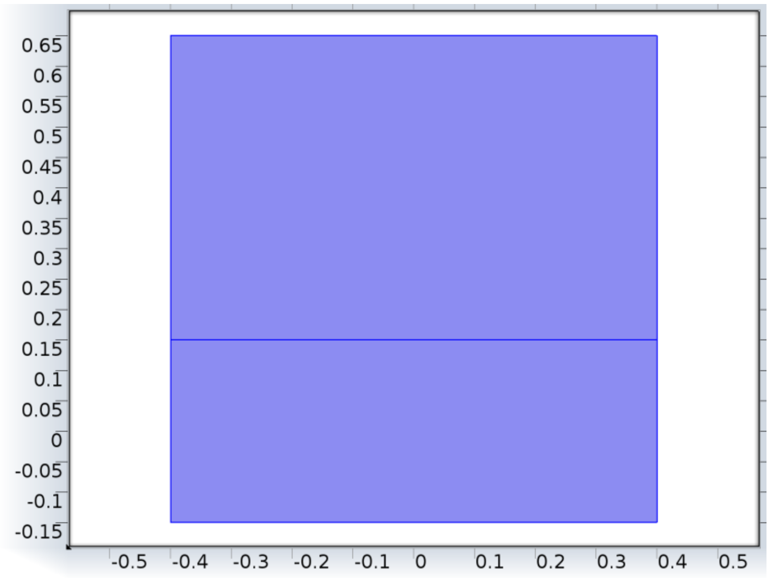

Wave Equation, Electric 1

Selection

Geometric entity level	Domain
Selection	Domains 1–2

Equations

$$\underline{\nabla \times (\nabla \times \mathbf{E})} - \underline{k_0^2 \epsilon_r} \mathbf{E} = \mathbf{0}$$

$$\lambda = -j\beta - \delta_z$$

6.2.1.2 Settings

Settings

Description	Value
Electrical conductivity	{{0, 0, 0}, {0, 0, 0}, {0, 0, 0}}
Reference temperature	293.15[K]
Relative permittivity	{{1, 0, 0}, {0, 1, 0}, {0, 0, 1}}
Relative permittivity (imaginary part)	{{0, 0, 0}, {0, 0, 0}, {0, 0, 0}}
Relative permittivity (real part)	{{1, 0, 0}, {0, 1, 0}, {0, 0, 1}}
Refractive index	From material
Refractive index	{{1, 0, 0}, {0, 1, 0}, {0, 0, 1}}
Refractive index, imaginary part	From material
Refractive index, imaginary part	{{0, 0, 0}, {0, 0, 0}, {0, 0, 0}}
Electric displacement field model	Refractive index
Relative permeability	{{1, 0, 0}, {0, 1, 0}, {0, 0, 1}}
Relative permittivity, high-frequency	{{1, 0, 0}, {0, 1, 0}, {0, 0, 1}}

Properties from material

Property	Material	Property group
Refractive index	Silver	Refractive index
Refractive index, imaginary part	Silver	Refractive index
Refractive index	Si	Refractive index
Refractive index, imaginary part	Si	Refractive index

6.2.1.3 Variables

Name	**Expression**	**Unit**	**Description**	**Selection**
emw.Qsh	0	W/m^2	Surface losses	Boundaries 1–7
emw.Qe	emw.Qml+emw.Qrh	W/m^3	Electromagnetic power loss density	Domains 1–2
emw.Qh	emw.Qml+emw.Qrh	W/m^3	Total power dissipation density	Domains 1–2
emw.Jx	emw.sigmaxx*emw.Ex+emw.sigmaxy*emw.Ey+emw.sigmaxz*emw.Ez+emw.Jdx	A/m^2	Current density, x component	Domains 1–2
emw.Jy	emw.sigmayx*emw.Ex+emw.sigmayy*emw.Ey+emw.sigmayz*emw.Ez+emw.Jdy	A/m^2	Current density, y component	Domains 1–2
emw.Jz	emw.sigmazx*emw.Ex+emw.sigmazy*emw.Ey+emw.sigmazz*emw.Ez+emw.Jdz	A/m^2	Current density, z component	Domains 1–2
emw.tJx	0	A/m^2	Tangential current density, x component	Boundaries 1–7
emw.tJy	0	A/m^2	Tangential current density, y component	Boundaries 1–7

Name	Expression	Unit	Description	Selection
emw.tJz	0	A/m^2	Tangential current density, z component	Boundaries 1–7
emw.Wav	emw.Weav+emw.Wmav	J/m^3	Energy density time average	Domains 1–2
emw.W	0	J/m^3	Energy density	Domains 1–2
emw.nxx	model.input.n11	1	Refractive index, xx component	Domain 1
emw.nyx	model.input.n21	1	Refractive index, yx component	Domain 1
emw.nzx	model.input.n31	1	Refractive index, zx component	Domain 1
emw.nxy	model.input.n12	1	Refractive index, xy component	Domain 1
emw.nyy	model.input.n22	1	Refractive index, yy component	Domain 1
emw.nzy	model.input.n32	1	Refractive index, zy component	Domain 1
emw.nxz	model.input.n13	1	Refractive index, xz component	Domain 1
emw.nyz	model.input.n23	1	Refractive index, yz component	Domain 1
emw.nzz	model.input.n33	1	Refractive index, zz component	Domain 1

Name	Expression	Unit	Description	Selection
emw.nxx	model.input.n11	1	Refractive index, xx component	Domain 2
emw.nyx	model.input.n21	1	Refractive index, yx component	Domain 2
emw.nzx	model.input.n31	1	Refractive index, zx component	Domain 2
emw.nxy	model.input.n12	1	Refractive index, xy component	Domain 2
emw.nyy	model.input.n22	1	Refractive index, yy component	Domain 2
emw.nzy	model.input.n32	1	Refractive index, zy component	Domain 2
emw.nxz	model.input.n13	1	Refractive index, xz component	Domain 2
emw.nyz	model.input.n23	1	Refractive index, yz component	Domain 2
emw.nzz	model.input.n33	1	Refractive index, zz component	Domain 2
emw.kixx	model.input.ki11	1	Refractive index, imaginary part, xx component	Domain 1
emw.kiyx	model.input.ki21	1	Refractive index, imaginary part, yx component	Domain 1

Name	**Expression**	**Unit**	**Description**	**Selection**
emw.kizx	model.input.ki31	1	Refractive index, imaginary part, zx component	Domain 1
emw.kixy	model.input.ki12	1	Refractive index, imaginary part, xy component	Domain 1
emw.kiyy	model.input.ki22	1	Refractive index, imaginary part, yy component	Domain 1
emw.kizy	model.input.ki32	1	Refractive index, imaginary part, zy component	Domain 1
emw.kixz	model.input.ki13	1	Refractive index, imaginary part, xz component	Domain 1
emw.kiyz	model.input.ki23	1	Refractive index, imaginary part, yz component	Domain 1
emw.kizz	model.input.ki33	1	Refractive index, imaginary part, zz component	Domain 1
emw.kixx	model.input.ki11	1	Refractive index, imaginary part, xx component	Domain 2

Name	**Expression**	**Unit**	**Description**	**Selection**
emw.kiyx	model.input.ki21	1	Refractive index, imaginary part, yx component	Domain 2
emw.kizx	model.input.ki31	1	Refractive index, imaginary part, zx component	Domain 2
emw.kixy	model.input.ki12	1	Refractive index, imaginary part, xy component	Domain 2
emw.kiyy	model.input.ki22	1	Refractive index, imaginary part, yy component	Domain 2
emw.kizy	model.input.ki32	1	Refractive index, imaginary part, zy component	Domain 2
emw.kixz	model.input.ki13	1	Refractive index, imaginary part, xz component	Domain 2
emw.kiyz	model.input.ki23	1	Refractive index, imaginary part, yz component	Domain 2
emw.kizz	model.input.ki33	1	Refractive index, imaginary part, zz component	Domain 2

Name	**Expression**	**Unit**	**Description**	**Selection**
emw.epsilonrxx	(model.input.n11-i*model.input.ki11)^2	1	Relative permittivity, xx component	Domain 1
emw.epsilonryx	(model.input.n21-i*model.input.ki21)^2	1	Relative permittivity, yx component	Domain 1
emw.epsilonrzx	(model.input.n31-i*model.input.ki31)^2	1	Relative permittivity, zx component	Domain 1
emw.epsilonrxy	(model.input.n12-i*model.input.ki12)^2	1	Relative permittivity, xy component	Domain 1
emw.epsilonryy	(model.input.n22-i*model.input.ki22)^2	1	Relative permittivity, yy component	Domain 1
emw.epsilonrzy	(model.input.n32-i*model.input.ki32)^2	1	Relative permittivity, zy component	Domain 1
emw.epsilonrxz	(model.input.n13-i*model.input.ki13)^2	1	Relative permittivity, xz component	Domain 1
emw.epsilonryz	(model.input.n23-i*model.input.ki23)^2	1	Relative permittivity, yz component	Domain 1

Name	**Expression**	**Unit**	**Description**	**Selection**
emw.epsilonrzz	(model.input.n33-i*model.input.ki33)^2	1	Relative permittivity, zz component	Domain 1
emw.epsilonrxx	(model.input.n11-i*model.input.ki11)^2	1	Relative permittivity, xx component	Domain 2
emw.epsilonryx	(model.input.n21-i*model.input.ki21)^2	1	Relative permittivity, yx component	Domain 2
emw.epsilonrzx	(model.input.n31-i*model.input.ki31)^2	1	Relative permittivity, zx component	Domain 2
emw.epsilonrxy	(model.input.n12-i*model.input.ki12)^2	1	Relative permittivity, xy component	Domain 2
emw.epsilonryy	(model.input.n22-i*model.input.ki22)^2	1	Relative permittivity, yy component	Domain 2
emw.epsilonrzy	(model.input.n32-i*model.input.ki32)^2	1	Relative permittivity, zy component	Domain 2
emw.epsilonrxz	(model.input.n13-i*model.input.ki13)^2	1	Relative permittivity, xz component	Domain 2

Name	Expression	Unit	Description	Selection
emw.epsilonryz	(model.input.n23-i*model.input.ki23)^2	1	Relative permittivity, yz component	Domain 2
emw.epsilonrzz	(model.input.n33-i*model.input.ki33)^2	1	Relative permittivity, zz component	Domain 2
emw.Px	epsilon0_const*(emw.epsilonrxx*emw.Ex+emw.epsilonrxy*emw.Ey+emw.epsilonrxz*emw.Ez-emw.Ex)	C/m^2	Polarization, x component	Domains 1–2
emw.Py	epsilon0_const*(emw.epsilonryx*emw.Ex+emw.epsilonryy*emw.Ey+emw.epsilonryz*emw.Ez-emw.Ey)	C/m^2	Polarization, y component	Domains 1–2
emw.Pz	epsilon0_const*(emw.epsilonrzx*emw.Ex+emw.epsilonrzy*emw.Ey+emw.epsilonrzz*emw.Ez-emw.Ez)	C/m^2	Polarization, z component	Domains 1–2
emw.normP	sqrt(realdot(emw.Px,emw.Px)+realdot(emw.Py,emw.Py)+realdot(emw.Pz,emw.Pz))	C/m^2	Polarization norm	Domains 1–2

Name	Expression	Unit	Description	Selection
emw.Dx	epsilon0_const*emw.Ex +emw.Px	C/m^2	Electric displacement field, x component	Domains 1–2
emw.Dy	epsilon0_const*emw.Ey +emw.Py	C/m^2	Electric displacement field, y component	Domains 1–2
emw.Dz	epsilon0_const*emw.Ez +emw.Pz	C/m^2	Electric displacement field, z component	Domains 1–2
emw.normD	sqrt(realdot(emw.Dx,emw.Dx)+realdot(emw.Dy,emw.Dy)+realdot(emw.Dz,emw.Dz))	C/m^2	Electric displacement field norm	Domains 1–2
emw.epsrAv	(emw.epsilonrxx+emw.epsilonryy+emw.epsilonrzz)/3	1	Relative permittivity, average	Domains 1–2
emw.murxx	1	1	Relative permeability, xx component	Domains 1–2
emw.muryx	0	1	Relative permeability, yx component	Domains 1–2
emw.murzx	0	1	Relative permeability, zx component	Domains 1–2

Name	Expression	Unit	Description	Selection
emw.murxy	0	1	Relative permeability, xy component	Domains 1–2
emw.muryy	1	1	Relative permeability, yy component	Domains 1–2
emw.murzy	0	1	Relative permeability, zy component	Domains 1–2
emw.murxz	0	1	Relative permeability, xz component	Domains 1–2
emw.muryz	0	1	Relative permeability, yz component	Domains 1–2
emw.murzz	1	1	Relative permeability, zz component	Domains 1–2
emw.murAv	(emw.murxx+emw.muryy+emw.murzz)/3	1	Relative permeability, average	Domains 1–2
emw.sigmaxx	0	S/m	Electrical conductivity, xx component	Domains 1–2

Name	Expression	Unit	Description	Selection
emw.sigmayx	0	S/m	Electrical conductivity, yx component	Domains 1–2
emw.sigmazx	0	S/m	Electrical conductivity, zx component	Domains 1–2
emw.sigmaxy	0	S/m	Electrical conductivity, xy component	Domains 1–2
emw.sigmayy	0	S/m	Electrical conductivity, yy component	Domains 1–2
emw.sigmazy	0	S/m	Electrical conductivity, zy component	Domains 1–2
emw.sigmaxz	0	S/m	Electrical conductivity, xz component	Domains 1–2
emw.sigmayz	0	S/m	Electrical conductivity, yz component	Domains 1–2
emw.sigmazz	0	S/m	Electrical conductivity, zz component	Domains 1–2
emw.Ex	Ex	V/m	Electric field, x component	Domains 1–2

Name	**Expression**	**Unit**	**Description**	**Selection**
emw.Ey	Ey	V/m	Electric field, y component	Domains 1–2
emw.Ez	Ez	V/m	Electric field, z component	Domains 1–2
emw.curlEx	emw.alphaOOP*Ey+Ezy	V/m^2	Curl of electric field, x component	Domains 1–2
emw.curlEy	-emw.alphaOOP*Ex-Ezx	V/m^2	Curl of electric field, y component	Domains 1–2
emw.curlEz	curlEz	V/m^2	Curl of electric field, z component	Domains 1–2
emw.testdepEx	test(Ex)	V/m	Electric field, x component	Domains 1–2
emw.testdepEy	test(Ey)	V/m	Electric field, y component	Domains 1–2
emw.testdepEz	test(Ez)	V/m	Electric field, z component	Domains 1–2
emw.curltestdepEx	-emw.alphaOOP*test(Ey)+test(Ezy)	V/m^2	Curl of electric field, x component	Domains 1–2
emw.curltestdepEy	emw.alphaOOP*test(Ex)-test(Ezx)	V/m^2	Curl of electric field, y component	Domains 1–2
emw.curltestdepEz	test(curlEz)	V/m^2	Curl of electric field, z component	Domains 1–2
emw.dBdtx	-emw.curlEx	V/m^2	Magnetic flux density, time	Domains 1–2

Name	Expression	Unit	Description	Selection
			derivative, x component	
emw.dBdty	-emw.curlEy	V/m^2	Magnetic flux density, time derivative, y component	Domains 1–2
emw.dBdtz	-emw.curlEz	V/m^2	Magnetic flux density, time derivative, z component	Domains 1–2
emw.Bx	-emw.curlEx/emw.iomega	T	Magnetic flux density, x component	Domains 1–2
emw.By	-emw.curlEy/emw.iomega	T	Magnetic flux density, y component	Domains 1–2
emw.Bz	-emw.curlEz/emw.iomega	T	Magnetic flux density, z component	Domains 1–2
emw.murinvxx	(emw.muryy*emw.murzz-emw.muryz*emw.murzy)/(emw.murxx*emw.muryy*emw.murzz+emw.murxy*emw.muryz*emw.murzx+emw.murxz*em	1	Inverse of relative permeability, xx component	Domains 1–2

Name	Expression	Unit	Description	Selection
	w.muryx*emw.murzy-emw.murxx*emw.muryz*emw.murzy-emw.murxy*emw.muryx*emw.murzz-emw.murxz*emw.muryy*emw.murzx)			
emw.murinvyx	(emw.muryz*emw.murzx-emw.muryx*emw.murzz)/(emw.murxx*emw.muryy*emw.murzz+emw.murxy*emw.muryz*emw.murzx+emw.murxz*emw.muryx*emw.murzy-emw.murxx*emw.muryz*emw.murzy-emw.murxy*emw.muryx*emw.murzz-emw.murxz*emw.muryy*emw.murzx)	1	Inverse of relative permeability, yx component	Domains 1–2
emw.murinvzx	(emw.muryx*emw.murzy-emw.muryy*emw.murzx)/(emw.murxx*emw.muryy*emw.murzz+emw.murxy*emw.muryz*emw.murzx+emw.murxz*em	1	Inverse of relative permeability, zx component	Domains 1–2

Name	Expression	Unit	Description	Selection
	w.muryx*emw.murzy-emw.murxx*emw.muryz*emw.murzy-emw.murxy*emw.muryx*emw.murzz-emw.murxz*emw.muryy*emw.murzx)			
emw.murinvxy	(emw.murxz*emw.murzy-emw.murxy*emw.murzz)/(emw.murxx*emw.muryy*emw.murzz+emw.murxy*emw.muryz*emw.murzx+emw.murxz*emw.muryx*emw.murzy-emw.murxx*emw.muryz*emw.murzy-emw.murxy*emw.muryx*emw.murzz-emw.murxz*emw.muryy*emw.murzx)	1	Inverse of relative permeability, xy component	Domains 1–2
emw.murinvyy	(emw.murxx*emw.murzz-emw.murxz*emw.murzx)/(emw.murxx*emw.muryy*emw.murzz+emw.murxy*emw.muryz*emw.murzx+emw.murxz*em	1	Inverse of relative permeability, yy component	Domains 1–2

Name	**Expression**	**Unit**	**Description**	**Selection**
	w.muryx*emw.murzy-emw.murxx*emw.muryz*emw.murzy-emw.murxy*emw.muryx*emw.murzz-emw.murxz*emw.muryy*emw.murzx)			
emw.murinvzy	(emw.murxy*emw.murzx-emw.murxx*emw.murzy)/(emw.murxx*emw.muryy*emw.murzz+emw.murxy*emw.muryz*emw.murzx+emw.murxz*emw.muryx*emw.murzy-emw.murxx*emw.muryz*emw.murzy-emw.murxy*emw.muryx*emw.murzz-emw.murxz*emw.muryy*emw.murzx)	1	Inverse of relative permeability, zy component	Domains 1–2
emw.murinvxz	(emw.murxy*emw.muryz-emw.murxz*emw.muryy)/(emw.murxx*emw.muryy*emw.murzz+emw.murxy*emw.muryz*emw.murzx+emw.murxz*em	1	Inverse of relative permeability, xz component	Domains 1–2

Name	Expression	Unit	Description	Selection
	w.muryx*emw.murzy-emw.murxx*emw.muryz*emw.murzy-emw.murxy*emw.muryx*emw.murzz-emw.murxz*emw.muryy*emw.murzx)			
emw.murinvyz	(emw.murxz*emw.muryx-emw.murxx*emw.muryz)/(emw.murxx*emw.muryy*emw.murzz+emw.murxy*emw.muryz*emw.murzx+emw.murxz*emw.muryx*emw.murzy-emw.murxx*emw.muryz*emw.murzy-emw.murxy*emw.muryx*emw.murzz-emw.murxz*emw.muryy*emw.murzx)	1	Inverse of relative permeability, yz component	Domains 1–2
emw.murinvzz	(emw.murxx*emw.muryy-emw.murxy*emw.muryx)/(emw.murxx*emw.muryy*emw.murzz+emw.murxy*emw.muryz*emw.murzx+emw.murxz*em	1	Inverse of relative permeability, zz component	Domains 1–2

Name	Expression	Unit	Description	Selection
	w.muryx*emw.murzy-emw.murxx*emw.muryz*emw.murzy-emw.murxy*emw.muryx*emw.murzz-emw.murxz*emw.muryy*emw.murzx)			
emw.Hx	(emw.murinvxx*emw.Bx+emw.murinvxy*emw.By+emw.murinvxz*emw.Bz)/mu0_const	A/m	Magnetic field, x component	Domains 1–2
emw.Hy	(emw.murinvyx*emw.Bx+emw.murinvyy*emw.By+emw.murinvyz*emw.Bz)/mu0_const	A/m	Magnetic field, y component	Domains 1–2
emw.Hz	(emw.murinvzx*emw.Bx+emw.murinvzy*emw.By+emw.murinvzz*emw.Bz)/mu0_const	A/m	Magnetic field, z component	Domains 1–2
emw.dHdtx	(emw.murinvxx*emw.dBdtx+emw.murinvxy*emw.dBdty+emw.murinvxz*emw.dBdtz)/mu0_const	A/(m*s)	Magnetic field, time derivative, x component	Domains 1–2
emw.dHdty	(emw.murinvyx*emw.dBdtx+emw.murinvyy*emw.dBdty+emw.murinvyz	A/(m*s)	Magnetic field, time derivative, y component	Domains 1–2

Name	Expression	Unit	Description	Selection
	*emw.dBdtz)/mu0_const			
emw.dHdtz	(emw.murinvzx*emw.dBdtx+emw.murinvzy*emw.dBdty+emw.murinvzz*emw.dBdtz)/mu0_const	A/(m*s)	Magnetic field, time derivative, z component	Domains 1–2
emw.normE	sqrt(realdot(emw.Ex,emw.Ex)+realdot(emw.Ey,emw.Ey)+realdot(emw.Ez,emw.Ez))	V/m	Electric field norm	Domains 1–2
emw.tEsdimx	tEx	V/m	Tangential electric field, x component	Boundaries 1–7
emw.tEsdimy	tEy	V/m	Tangential electric field, y component	Boundaries 1–7
emw.tEsdimz	Ez	V/m	Tangential electric field, z component	Boundaries 1–7
emw.tEx	emw.tEsdimx	V/m	Tangential electric field, x component	Boundaries 1–7
emw.tEy	emw.tEsdimy	V/m	Tangential electric field, y component	Boundaries 1–7
emw.tEz	emw.tEsdimz	V/m	Tangential electric field, z component	Boundaries 1–7
emw.testPhystEx	test(emw.tEx)	V/m	Tangential electric field, x component	Boundaries 1–7

Name	Expression	Unit	Description	Selection
emw.testPhystEy	test(emw.tEy)	V/m	Tangential electric field, y component	Boundaries 1–7
emw.testPhystEz	test(emw.tEz)	V/m	Tangential electric field, z component	Boundaries 1–7
emw.Mx	emw.Bx/mu0_const-emw.Hx	A/m	Magnetization, x component	Domains 1–2
emw.My	emw.By/mu0_const-emw.Hy	A/m	Magnetization, y component	Domains 1–2
emw.Mz	emw.Bz/mu0_const-emw.Hz	A/m	Magnetization, z component	Domains 1–2
emw.normM	sqrt(realdot(emw.Mx,emw.Mx)+realdot(emw.My,emw.My)+realdot(emw.Mz,emw.Mz))	A/m	Magnetization norm	Domains 1–2
emw.Brx	0	T	Remanent flux density, x component	Domains 1–2
emw.Bry	0	T	Remanent flux density, y component	Domains 1–2
emw.Brz	0	T	Remanent flux density, z component	Domains 1–2
emw.normBr	sqrt(realdot(emw.Brx,emw.Brx)+realdot(emw.B	T	Remanent flux density norm	Domains 1–2

Name	Expression	Unit	Description	Selection
	ry,emw.Bry)+realdot(emw.Brz,emw.Brz))			
emw.Qml	real(0.5*emw.iomega*(emw.Bx*conj(emw.Hx)+emw.By*conj(emw.Hy)+emw.Bz*conj(emw.Hz)))	W/m^3	Magnetic losses	Domains 1–2
emw.tBx	emw.Bx-(emw.nx*emw.Bx+emw.ny*emw.By+emw.nz*emw.Bz)*emw.nx	T	Tangential magnetic flux density, x component	Boundaries 1–7
emw.tBy	emw.By-(emw.nx*emw.Bx+emw.ny*emw.By+emw.nz*emw.Bz)*emw.ny	T	Tangential magnetic flux density, y component	Boundaries 1–7
emw.tBz	emw.Bz-(emw.nx*emw.Bx+emw.ny*emw.By+emw.nz*emw.Bz)*emw.nz	T	Tangential magnetic flux density, z component	Boundaries 1–7
emw.normB	sqrt(realdot(emw.Bx,emw.Bx)+realdot(emw.By,emw.By)+realdot(emw.Bz,emw.Bz))	T	Magnetic flux density norm	Domains 1–2
emw.normH	sqrt(realdot(emw.Hx,emw.Hx)+realdot(emw.Hy,emw.Hy)+realdot(emw.Hz,emw.Hz))	A/m	Magnetic field norm	Domains 1–2

Name	Expression	Unit	Description	Selection
emw.Jix	emw.sigmaxx*emw.Ex+emw.sigmaxy*emw.Ey+emw.sigmaxz*emw.Ez	A/m^2	Induced current density, x component	Domains 1–2
emw.Jiy	emw.sigmayx*emw.Ex+emw.sigmayy*emw.Ey+emw.sigmayz*emw.Ez	A/m^2	Induced current density, y component	Domains 1–2
emw.Jiz	emw.sigmazx*emw.Ex+emw.sigmazy*emw.Ey+emw.sigmazz*emw.Ez	A/m^2	Induced current density, z component	Domains 1–2
emw.Jdx	emw.iomega*emw.Dx	A/m^2	Displacement current density, x component	Domains 1–2
emw.Jdy	emw.iomega*emw.Dy	A/m^2	Displacement current density, y component	Domains 1–2
emw.Jdz	emw.iomega*emw.Dz	A/m^2	Displacement current density, z component	Domains 1–2
emw.normJ	sqrt(realdot(emw.Jx,emw.Jx)+realdot(emw.Jy,emw.Jy)+realdot(emw.Jz,emw.Jz))	A/m^2	Current density norm	Domains 1–2
emw.dWe	emw.Weav	J/m^3	Integrand for total electric energy	Domains 1–2

Name	Expression	Unit	Description	Selection
emw.Weav	0.25*(realdot(d(emw.freq*emw.Dx,emw.freq),emw.Ex)+realdot(d(emw.freq*emw.Dy,emw.freq),emw.Ey)+realdot(d(emw.freq*emw.Dz,emw.freq),emw.Ez))	J/m^3	Electric energy density time average	Domains 1–2
emw.Qrh	0.5*(realdot(emw.Jx,emw.Ex)+realdot(emw.Jy,emw.Ey)+realdot(emw.Jz,emw.Ez))	W/m^3	Resistive losses	Domains 1–2
emw.dWm	emw.Wmav	J/m^3	Integrand for total magnetic energy	Domains 1–2
emw.Wmav	0.25*(realdot(mu0_const*(d(emw.freq*emw.murxx,emw.freq)*emw.Hx+d(emw.freq*emw.murxy,emw.freq)*emw.Hy+d(emw.freq*emw.murxz,emw.freq)*emw.Hz),emw.Hx)+realdot(mu0_const*(d(emw.freq*emw.muryx,emw.freq)*emw.Hx+d(emw.freq*emw.muryy,emw.freq)*emw.Hy+d(emw.freq*emw.muryz,emw.freq)*emw.Hz),emw	J/m^3	Magnetic energy density time average	Domains 1–2

Name	Expression	Unit	Description	Selection
	.Hy)+realdot(mu0_const*(d(emw.freq*emw.murzx,emw.freq)*emw.Hx+d(emw.freq*emw.murzy,emw.freq)*emw.Hy+d(emw.freq*emw.murzz,emw.freq)*emw.Hz),emw.Hz))			
emw.Poavx	0.5*real(conj(emw.Hz)*emw.Ey-conj(emw.Hy)*emw.Ez)	W/m^2	Power flow, time average, x component	Domains 1–2
emw.Poavy	0.5*real(-conj(emw.Hz)*emw.Ex+conj(emw.Hx)*emw.Ez)	W/m^2	Power flow, time average, y component	Domains 1–2
emw.Poavz	0.5*real(conj(emw.Hy)*emw.Ex-conj(emw.Hx)*emw.Ey)	W/m^2	Power flow, time average, z component	Domains 1–2
emw.nPoav	real(0.5*((conj(emw.Hz)*emw.Ey-conj(emw.Hy)*emw.Ez)*emw.nx+(-conj(emw.Hz)*emw.Ex+conj(emw.Hx)*emw.Ez)*emw.ny+(conj(emw.Hy)*emw.Ex-conj(emw.Hx)*emw.Ey)*emw.nz))	W/m^2	Power outflow, time average	Boundaries 1–7

Name	Expression	Unit	Description	Selection
emw.deltaS	1/real(sqrt(emw.iomega*mu0_const*(emw.murxx+emw.muryy+emw.murzz)*(emw.sigmaxx+emw.sigmayy+emw.sigmazz+emw.iomega*epsilon0_const*(emw.epsilonrxx+emw.epsilonryy+emw.epsilonrzz))/9))	m	Skin depth	Domains 1–2
emw.unTx	emw.unTmx+emw.unTex	Pa	Maxwell upward surface stress tensor, x component	Boundaries 1–7
emw.unTy	emw.unTmy+emw.unTey	Pa	Maxwell upward surface stress tensor, y component	Boundaries 1–7
emw.unTz	emw.unTmz+emw.unTez	Pa	Maxwell upward surface stress tensor, z component	Boundaries 1–7
emw.dnTx	emw.dnTmx+emw.dnTex	Pa	Maxwell downward surface stress tensor, x component	Boundaries 1–7
emw.dnTy	emw.dnTmy+emw.dnTey	Pa	Maxwell downward surface stress	Boundaries 1–7

Name	**Expression**	**Unit**	**Description**	**Selection**
			tensor, y component	
emw.dnTz	emw.dnTmz+emw.dnTez	Pa	Maxwell downward surface stress tensor, z component	Boundaries 1–7
emw.unx	unx		Normal vector up direction, x component	Boundaries 1–7
emw.uny	uny		Normal vector up direction, y component	Boundaries 1–7
emw.unz	0		Normal vector up direction, z component	Boundaries 1–7
emw.dnx	dnx		Normal vector down direction, x component	Boundaries 1–7
emw.dny	dny		Normal vector down direction, y component	Boundaries 1–7
emw.dnz	0		Normal vector down direction, z component	Boundaries 1–7
emw.unTmx	0.5*real(-0.5*emw.dnx*(up(emw.	Pa	Maxwell upward magnetic surface	Boundary 4

Name	**Expression**	**Unit**	**Description**	**Selection**
	Bx)*up(conj(emw.Hx))+up(emw.By)*up(conj(emw.Hy))+up(emw.Bz)*up(conj(emw.Hz)))+up(emw.Bx)*(up(conj(emw.Hx))*emw.dnx+up(conj(emw.Hy))*emw.dny+up(conj(emw.Hz))*emw.dnz))		stress tensor, x component	
emw.unTmy	0.5*real(-0.5*emw.dny*(up(emw.Bx)*up(conj(emw.Hx))+up(emw.By)*up(conj(emw.Hy))+up(emw.Bz)*up(conj(emw.Hz)))+up(emw.By)*(up(conj(emw.Hx))*emw.dnx+up(conj(emw.Hy))*emw.dny+up(conj(emw.Hz))*emw.dnz))	Pa	Maxwell upward magnetic surface stress tensor, y component	Boundary 4
emw.unTmz	0.5*real(-0.5*emw.dnz*(up(emw.Bx)*up(conj(emw.Hx))+up(emw.By)*up(conj(emw.Hy))+up(emw.Bz)*up(conj(emw.Hz)))+up(emw.Bz)*(up(conj(emw.Hx))*emw.dnx+up(conj(emw.	Pa	Maxwell upward magnetic surface stress tensor, z component	Boundary 4

Name	Expression	Unit	Description	Selection
	Hy))*emw.dny+up(conj(emw.Hz))*emw.dnz))			
emw.unTmx	0	Pa	Maxwell upward magnetic surface stress tensor, x component	Boundaries 1–3, 5–7
emw.unTmy	0	Pa	Maxwell upward magnetic surface stress tensor, y component	Boundaries 1–3, 5–7
emw.unTmz	0	Pa	Maxwell upward magnetic surface stress tensor, z component	Boundaries 1–3, 5–7
emw.dnTmx	0.5*real(-0.5*emw.unx*(down(emw.Bx)*down(conj(emw.Hx))+down(emw.By)*down(conj(emw.Hy))+down(emw.Bz)*down(conj(emw.Hz)))+down(emw.Bx)*(down(conj(emw.Hx))*emw.unx+down(conj(emw.Hy))*emw.uny+down(conj(emw.Hz))*emw.unz))	Pa	Maxwell downward magnetic surface stress tensor, x component	Boundary 4

Name	Expression	Unit	Description	Selection
emw.dnTmy	0.5*real(-0.5*emw.uny*(down(emw.Bx)*down(conj(emw.Hx))+down(emw.By)*down(conj(emw.Hy))+down(emw.Bz)*down(conj(emw.Hz)))+down(emw.By)*(down(conj(emw.Hx))*emw.unx+down(conj(emw.Hy))*emw.uny+down(conj(emw.Hz))*emw.unz))	Pa	Maxwell downward magnetic surface stress tensor, y component	Boundary 4
emw.dnTmz	0.5*real(-0.5*emw.unz*(down(emw.Bx)*down(conj(emw.Hx))+down(emw.By)*down(conj(emw.Hy))+down(emw.Bz)*down(conj(emw.Hz)))+down(emw.Bz)*(down(conj(emw.Hx))*emw.unx+down(conj(emw.Hy))*emw.uny+down(conj(emw.Hz))*emw.unz))	Pa	Maxwell downward magnetic surface stress tensor, z component	Boundary 4
emw.dnTmx	0.5*real(-0.5*emw.unx*(down(emw.Bx)*down(conj(emw.Hx))+down(emw.By)*do	Pa	Maxwell downward magnetic surface	Boundaries 1–3, 5–7

Name	Expression	Unit	Description	Selection
	wn(conj(emw.Hy))+down(emw.Bz)*down(conj(emw.Hz)))+down(emw.Bx)*(down(conj(emw.Hx))*emw.unx+down(conj(emw.Hy))*emw.uny+down(conj(emw.Hz))*emw.unz))		stress tensor, x component	
emw.dnTmy	0.5*real(-0.5*emw.uny*(down(emw.Bx)*down(conj(emw.Hx))+down(emw.By)*down(conj(emw.Hy))+down(emw.Bz)*down(conj(emw.Hz)))+down(emw.By)*(down(conj(emw.Hx))*emw.unx+down(conj(emw.Hy))*emw.uny+down(conj(emw.Hz))*emw.unz))	Pa	Maxwell downward magnetic surface stress tensor, y component	Boundaries 1–3, 5–7
emw.dnTmz	0.5*real(-0.5*emw.unz*(down(emw.Bx)*down(conj(emw.Hx))+down(emw.By)*down(conj(emw.Hy))+down(emw.Bz)*down(conj(emw.Hz)))+down(emw.Bz)*(down(conj(emw.Hx))*	Pa	Maxwell downward magnetic surface stress tensor, z component	Boundaries 1–3, 5–7

Name	Expression	Unit	Description	Selection
	emw.unx+down(conj(emw.Hy))*emw.uny+down(conj(emw.Hz))*emw.unz))			
emw.unTex	0.5*real(-0.5*emw.dnx*(up(emw.Dx)*up(conj(emw.Ex))+up(emw.Dy)*up(conj(emw.Ey))+up(emw.Dz)*up(conj(emw.Ez)))+up(emw.Dx)*(up(conj(emw.Ex))*emw.dnx+up(conj(emw.Ey))*emw.dny+up(conj(emw.Ez))*emw.dnz))	Pa	Maxwell upward electric surface stress tensor, x component	Boundary 4
emw.unTey	0.5*real(-0.5*emw.dny*(up(emw.Dx)*up(conj(emw.Ex))+up(emw.Dy)*up(conj(emw.Ey))+up(emw.Dz)*up(conj(emw.Ez)))+up(emw.Dy)*(up(conj(emw.Ex))*emw.dnx+up(conj(emw.Ey))*emw.dny+up(conj(emw.Ez))*emw.dnz))	Pa	Maxwell upward electric surface stress tensor, y component	Boundary 4
emw.unTez	0.5*real(-0.5*emw.dnz*(up(emw.Dx)*up(conj(emw.Ex))+u	Pa	Maxwell upward electric surface	Boundary 4

Name	Expression	Unit	Description	Selection
	p(emw.Dy)*up(conj(emw.Ey))+up(emw.Dz)*up(conj(emw.Ez)))+up(emw.Dz)*(up(conj(emw.Ex))*emw.dnx+up(conj(emw.Ey))*emw.dny+up(conj(emw.Ez))*emw.dnz))		stress tensor, z component	
emw.unTex	0	Pa	Maxwell upward electric surface stress tensor, x component	Boundaries 1–3, 5–7
emw.unTey	0	Pa	Maxwell upward electric surface stress tensor, y component	Boundaries 1–3, 5–7
emw.unTez	0	Pa	Maxwell upward electric surface stress tensor, z component	Boundaries 1–3, 5–7
emw.dnTex	0.5*real(-0.5*emw.unx*(down(emw.Dx)*down(conj(emw.Ex))+down(emw.Dy)*down(conj(emw.Ey))+down(emw.Dz)*down(conj(emw.Ez)))+down(emw.Dx)*(down(conj(emw.Ex	Pa	Maxwell downward electric surface stress tensor, x component	Boundary 4

Name	Expression	Unit	Description	Selection
	))*emw.unx+down(conj(emw.Ey))*emw.uny+down(conj(emw.Ez))*emw.unz))			
emw.dnTey	0.5*real(-0.5*emw.uny*(down(emw.Dx)*down(conj(emw.Ex))+down(emw.Dy)*down(conj(emw.Ey))+down(emw.Dz)*down(conj(emw.Ez)))+down(emw.Dy)*(down(conj(emw.Ex))*emw.unx+down(conj(emw.Ey))*emw.uny+down(conj(emw.Ez))*emw.unz))	Pa	Maxwell downward electric surface stress tensor, y component	Boundary 4
emw.dnTez	0.5*real(-0.5*emw.unz*(down(emw.Dx)*down(conj(emw.Ex))+down(emw.Dy)*down(conj(emw.Ey))+down(emw.Dz)*down(conj(emw.Ez)))+down(emw.Dz)*(down(conj(emw.Ex))*emw.unx+down(conj(emw.Ey))*emw.uny+down(	Pa	Maxwell downward electric surface stress tensor, z component	Boundary 4

Name	Expression	Unit	Description	Selection
	conj(emw.Ez))*emw.unz))			
emw.dnTex	0.5*real(-0.5*emw.unx*(down(emw.Dx)*down(conj(emw.Ex))+down(emw.Dy)*down(conj(emw.Ey))+down(emw.Dz)*down(conj(emw.Ez)))+down(emw.Dx)*(down(conj(emw.Ex))*emw.unx+down(conj(emw.Ey))*emw.uny+down(conj(emw.Ez))*emw.unz))	Pa	Maxwell downward electric surface stress tensor, x component	Boundaries 1–3, 5–7
emw.dnTey	0.5*real(-0.5*emw.uny*(down(emw.Dx)*down(conj(emw.Ex))+down(emw.Dy)*down(conj(emw.Ey))+down(emw.Dz)*down(conj(emw.Ez)))+down(emw.Dy)*(down(conj(emw.Ex))*emw.unx+down(conj(emw.Ey))*emw.uny+down(conj(emw.Ez))*emw.unz))	Pa	Maxwell downward electric surface stress tensor, y component	Boundaries 1–3, 5–7

Name	Expression	Unit	Description	Selection
emw.dnTez	0.5*real(-0.5*emw.unz*(down(emw.Dx)*down(conj(emw.Ex))+down(emw.Dy)*down(conj(emw.Ey))+down(emw.Dz)*down(conj(emw.Ez)))+down(emw.Dz)*(down(conj(emw.Ex))*emw.unx+down(conj(emw.Ey))*emw.uny+down(conj(emw.Ez))*emw.unz))	Pa	Maxwell downward electric surface stress tensor, z component	Boundaries 1–3, 5–7

2.4.2 Perfect Electric Conductor 1

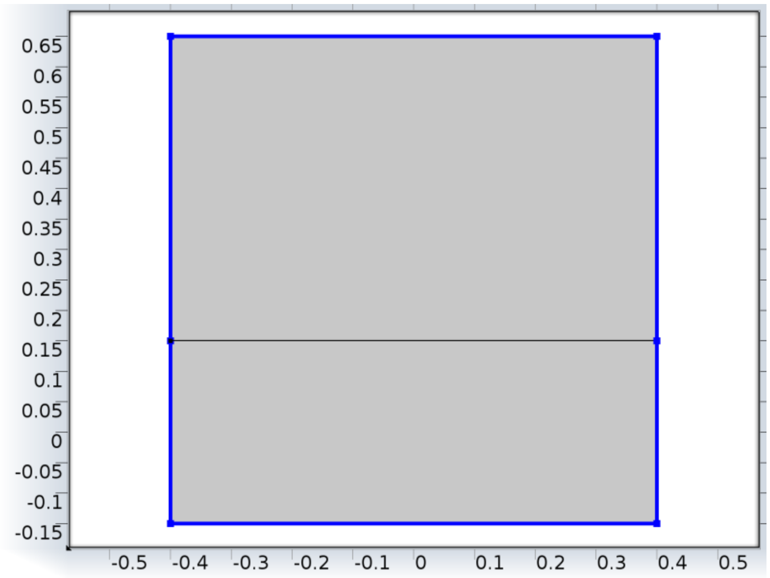

Perfect Electric Conductor 1

Selection

Geometric entity level	Boundary

Selection	Boundaries 1–3, 5–7

Equations

$$\mathbf{n} \times \mathbf{E} = \mathbf{0}$$

6.2.1.4 Settings

Settings

Description	Value
Apply reaction terms on	All physics (symmetric)
Use weak constraints	0

6.2.1.5 Variables

Name	Expression	Unit	Description	Selection
emw.Jsx	(up(emw.Hz)-down(emw.Hz))*emw.ny+(-up(emw.Hy)+down(emw.Hy))*emw.nz	A/m	Surface current density, x component	Boundaries 1–3, 5–7
emw.Jsy	(-up(emw.Hz)+down(emw.Hz))*emw.nx+(up(emw.Hx)-down(emw.Hx))*emw.nz	A/m	Surface current density, y component	Boundaries 1–3, 5–7
emw.Jsz	(up(emw.Hy)-down(emw.Hy))*emw.nx+(-up(emw.Hx)+down(emw.Hx))*emw.ny	A/m	Surface current density, z component	Boundaries 1–3, 5–7
emw.E0x	0	V/m	Electric field, x component	Boundaries 1–3, 5–7

Name	Expression	Unit	Description	Selection
emw.E0y	0	V/m	Electric field, y component	Boundaries 1–3, 5–7
emw.E0z	0	V/m	Electric field, z component	Boundaries 1–3, 5–7

2.4.3 Initial Values 1

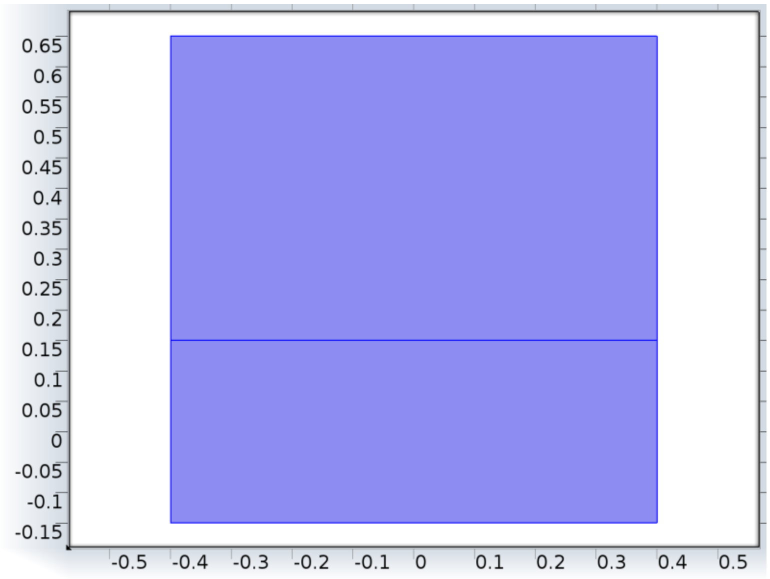

Initial Values 1

Selection

Geometric entity level	Domain
Selection	Domains 1–2

6.2.1.6 Settings

Settings

Description	Value
Electric field	{0, 0, 0}

2.5 Mesh 1

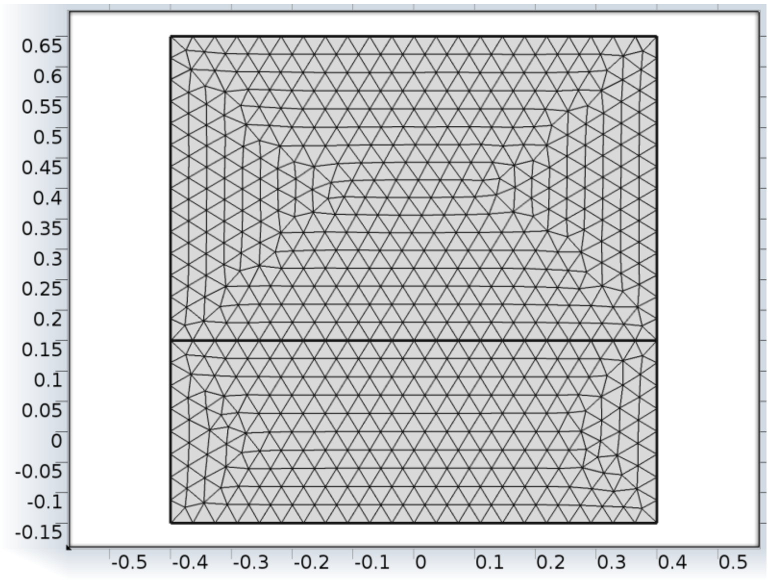

Mesh 1

2.5.1 Size (size)

Settings

Name	Value
Maximum element size	0.0376
Minimum element size	2.13E-4
Resolution of curvature	0.3
Resolution of narrow regions	7
Maximum element growth rate	1.5
Predefined size	Fine
Custom element size	Custom

2.5.2 Free Triangular 1 (ftri1)

Selection

Geometric entity level	Remaining

3 Study 1

3.1 Mode Analysis

Study settings

Property	Value
Include geometric nonlinearity	Off

Mesh selection

Geometry	Mesh
Geometry 1 (geom1)	mesh1

Physics selection

Physics	Discretization
Electromagnetic Waves (emw)	physics

3.2 Solver Configurations

3.2.1 Solver 1

6.2.1.7 Compile Equations: Mode Analysis (st1)

Study and step

Name	Value
Use study	Study 1
Use study step	Mode Analysis

6.2.1.8 Dependent Variables 1 (v1)

General

Name	Value
Defined by study step	Mode Analysis

Initial values of variables solved for

Name	Value
Solution	Zero

Values of variables not solved for

Name	Value
Solution	Zero

6.2.1.8.1 mod1.E (mod1_E)

General

Name	Value
Field components	{mod1.Ex, mod1.Ey, mod1.Ez}

6.2.1.9 Eigenvalue Solver 1 (e1)

General

Name	Value
Defined by study step	Mode Analysis
Desired number of eigenvalues	1
Eigenvalue transformation	Effective mode index
Value	nSeed

Values of linearization point

Name	Value
Solution	Zero

6.2.1.9.1 Advanced (aDef)

General

Name	Value
Allow complex-valued output from functions with real input	On

4 Results

4.1 Data Sets

4.1.1 Solution 1

Selection

Geometric entity level	Domain
Selection	Geometry geom1

Solution

Name	Value
Solution	Solver 1
Model	Save Point Geometry 1

4.1.2 horizontal line slice

Data

Name	Value
Data set	Solution 1

Advanced

Name	Value
Space variable	cln2x

4.1.3 Cut Line 2D 3

Data

Name	Value
Data set	Solution 1

Advanced

Name	Value
Space variable	cln3x

4.2 Tables

4.2.1 Eigenvalue solver

Eigenvalue solver

Iteration number	Error
0	1
1	1

4.3 Plot Groups

4.3.1 Electric Field (emw)

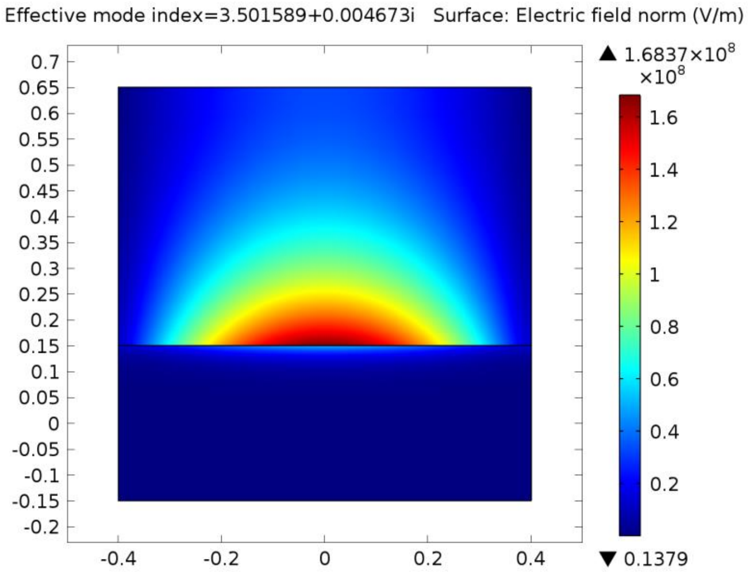

Effective mode index=3.501589+0.004673i Surface: Electric field norm (V/m)

4.3.2 1D Plot Group 2

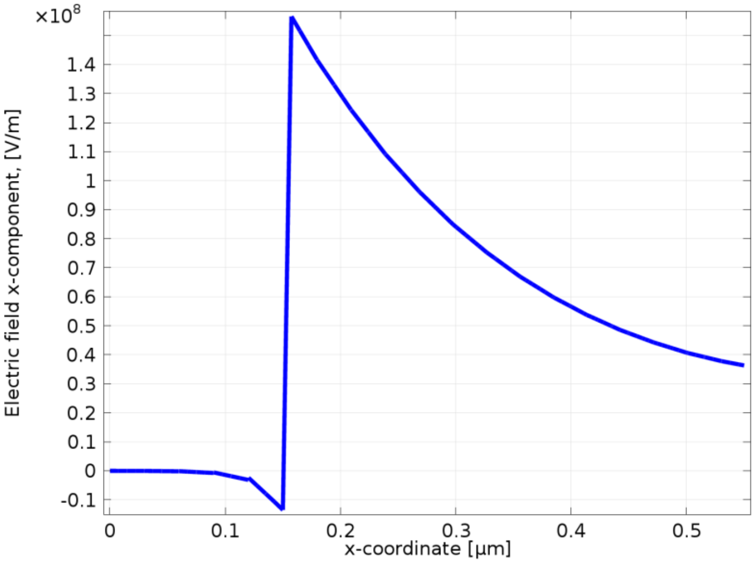

Appendix B List of Publications

[1] S. Aldawsari, L. Wei, and W.K. Liu, "Theoretical Study of Hybrid Guided Modes in a Multilayer Symmetrical Planar Plasmonic Waveguide," J. Lightwave Technol., vol. 33, no. 15, pp.3198-3206 (2015).

[2] S. Aldawsari, L. Wei, and W. K. Liu, "A Comprehensive Theoretical Study of the Guided Modes in a Five-Layer Hybrid-Metal/Dielectric/Metal Waveguide," J. Lightwave Technol., vol. 35, no. 11, pp. 2243-2251 (2017).

[3] S. Aldawsari, L. Wei, and W. K. Liu, "Analytical Study for Hybrid Guided Modes in a 7-layer Plasmonic Waveguide," *Photonics North Conference*, June 9-11, 2015, Ottawa, ON, Canada.

[4] S. Aldawsari, L. Wei, and W. K. Liu, "Propagation Characteristics of Hybrid Guided Modes in a 5-layer Metal/Dielectric/Metal Waveguide," *Photonics North Conference*, June 6-8, 2017, Ottawa, ON, Canada.

[5] L. Wei, S. Aldawsari, W. Liu, and B. R. West, "Theoretical analysis of plasmonic modes in a symmetric conductor–gap–dielectric structure for nanoscale confinement," IEEE Photonics Journal, vol.6, no.3, pp.1-10 (2014)